Resonant Raman spectroscopy of low-dimensional semiconductor structures

DISSERTATION ZUR ERLANGUNG DES DOKTORGRADES DER NATURWISSENSCHAFTEN
(DR. RER. NAT)
DER FAKULTÄT FÜR PHYSIK
DER UNIVERSITÄT REGENSBURG

vorgelegt von
Sebastian Meier
aus Regensburg

im Jahr 2022

Das Promotionsgesuch wurde eingereicht am 26.01.2022

Die Arbeit wurde angeleitet von: Prof. Dr. Christian Schüller

Prüfungsausschuss:

Vorsitzender:	Prof. Dr. John Schliemann
1. Gutachter:	Prof. Dr. Christian Schüller
2. Gutachter:	Prof. Dr. Dominique Bougeard
weiterer Prüfer:	Prof. Dr. Franz J. Gießibl

Contents

1. Introduction **1**

I. Experimental methods 4

2. Excitons and photoluminescence **5**

2.1. Formation of excitonic states 5
2.2. Mott transition 7
2.3. Photoluminescence emission and excitation 8

3. Raman spectroscopy **9**

3.1. Basic principle of Raman spectroscopy 9
3.2. Mediation by the electronic system 12
3.3. Electron-phonon coupling 14
3.3.1. Deformation-potential interaction 14
3.3.2. Fröhlich interaction 15

4. Experimental setup **16**

4.1. Micro-Raman setup 16
4.2. Microscope setup for magnetic fields 18

II. Intersubband excitations in wurtzite GaAs wires 22

5. Theoretical background and state of the art **24**

5.1. Synthesis of ultra thin core-shell wires 24
5.2. Formation of wurtzite crystal structure 26
5.3. Raman spectroscopy of wurtzite wires 28
5.4. Electronic band structure of wurtzite GaAs 30
5.5. Formation of one-dimensional subbands 32

5.6. Inelastic light scattering in low-dimensional GaAs structures 35

6. Experimental results on GaAs nanowires **39**
6.1. PL characteristics of nanowires 39
6.1.1. Polarization and excitation energy dependence 39
6.1.2. PLE 41
6.2. Observation of electronic Raman peaks 43
6.2.1. Diameter dependence 43
6.2.2. Resonance behaviour 45
6.2.3. Polarization dependence 47
6.3. Interpretation as intersubband excitations 49
6.3.1. Scattering mechanism 49
6.3.2. Comparison to band structure calculations 51
6.3.3. Discussion of linewidth 54
6.4. Effects of excitation power 55
6.4.1. Determination of charge-carrier density 56
6.4.2. Power dependence of Raman peaks 58
6.4.3. Comparison of all data to calculated absorption 59
6.4.4. High-power excitation 61

7. Conclusion and outlook on part two **65**

III. Resonance effects in $MoSe_2$-WSe_2 heterostructures **69**

8. Basic principles of TMDCs **71**
8.1. Crystal structure of TMDCs 71
8.2. Electronic properties 72
8.2.1. Band structure of TMDCs 72
8.2.2. Excitons in TMDCs 75
8.2.3. Behaviour under external magnetic fields 78
8.3. Raman spectroscopy of TMDCs 79
8.3.1. Intralayer modes 79
8.3.2. Interlayer modes 81
8.4. TMDC heterostructures 82
8.4.1. Moiré lattice and atomic reconstruction 82

8.4.2. Interlayer excitons . . . 86
8.5. Sample preparation . . . 88

9. Experimental results on $MoSe_2$-WSe_2 heterostructures 91
9.1. Non-resonant temperature dependence . . . 91
9.2. Quenching of intralayer PL . . . 93
9.3. Excitation energy dependent spectra . . . 95
9.4. Temperature dependence of resonance effects . . . 98
9.5. Power and polarization behaviour . . . 100
9.6. Possible connection to trion states . . . 101
9.6.1. Proposed scattering mechanism . . . 101
9.6.2. External magnetic fields . . . 103
9.7. Twist angle dependence . . . 104
9.7.1. Misaligned heterostructures . . . 104
9.7.2. Correlation with atomic reconstruction . . . 106
9.7.3. H- and R-type comparison . . . 107
9.8. Possible interpretations . . . 108

10. Conclusion and outlook on part three 112

Bibliography 116

1. Introduction

The concept of inelastic light scattering by a medium was discovered in 1928 by C. V. Raman [1, 2], leading to the development of Raman spectroscopy. This technique uses scattering processes that change the frequency of the incident light, in order to gain information about elementary excitations which are present in the medium. In solids, Raman spectroscopy focusses mainly on the investigation of optical phonons [3], and has become a popular non-invasive tool for sample characterization. However, in the late 1970s, it was also established as a powerful technique to explore electronic effects in semiconductor quantum-well and quantum-wire structures, for an overview see [4]. In such experiments, the elementary excitations responsible for inelastic scattering are either single particle intersubband excitations of free electrons, or plasmonic effects such as charge-density or spin-density excitations.

In our working group, Raman experiments on quantum-well structures were used to explore the band dispersion of two-dimensional hole systems [5], or to reveal collective effects in the regime of the persistent spin helix [6, 7]. In order observe such electronic scattering events, the laser energy is required to hit resonances in the band structure of the sample. Therefore, one of our laboratories is specially dedicated to this so called resonant Raman spectroscopy. It contains a continuous-wave Ti:Sapphire laser, whose emission energy can be tuned continuously in the range between $\approx 1.3\,\mathrm{eV}$-$1.74\,\mathrm{eV}$, which enables it to reach the band gap of GaAs based systems. The backscattered light by the sample is detected using a triple Raman spectrometer, that allows to suppress elastically scattered laser light, which is important to measure Raman effects at low frequencies. In this thesis, the technique of resonant Raman spectroscopy is applied to two new material systems, that have not been examined by this approach so far.

The first material system investigated are single GaAs wires. This project was made possible by a cooperation with the group of Prof. Dominique Bougeard, where single nanowires are grown in MBE using the VLS-growth mechanism. These wires have a pure wurtzite phase crystal structure [8], and can reach minimal core diameters of 20 nm [9]. This opens the possibility to observe electronic Raman excitations within the quasi-

one-dimensional subband structure of single wires, which has not been demonstrated before, as one-dimensional systems used in Raman experiments so far were arrays of laterally structured quantum wells. In this thesis, the subband structure of single wires is characterized by photoluminescence, photoluminescence-excitation and resonant Raman spectroscopy. The obtained subband energies are compared to realistic k·p band structure calculations, which were done by Paulo de Faria Junior. We will also show that for low excitation powers, the wires are found in the one-dimensional quantum limit. For higher powers, the occupation of the first excited electron subband is revealed by the appearance of additional Raman peaks.

The second project of this thesis focusses on two-dimensional transition metal dichalcogenides (TMDCs). These belong to the class of van der Waals materials, which means their bulk form consists of atomic layers, that are only held together by weak van der Waals interactions. It was first realized for graphite, that this opens the possibility to thin these materials down to single layers (called graphene) by mechanical exfoliation [10]. The same technique is applicable for other types of layered materials, such as TMDCs [11], which in addition undergo a transition from indirect to direct semiconductor in this process [12, 13]. In this work, the focus will lie on $MoSe_2$, due to the great compatibility of its band gap size [14] to the Ti:Sapphire laser, enabling resonant excitation. However, resonant excitation of a direct semiconductor also leads to a strong luminescence that obscures Raman lines due to its much higher intensity. Therefore, we use a $MoSe_2$-WSe_2 heterostructure which quenches the intralayer luminescence. In our experiments we find a so far unknown Raman excitation, that is only visible in extreme resonance with the $MoSe_2$ trion. We analyse this effect by means of excitation-energy and power dependence, light polarization, sample temperature, external magnetic fields and the twist angle of the heterostructure. As this project is still ongoing, the exact interpretation of the new Raman effect is not entirely clear to us so far, which means only different scenarios are discussed in the end.

Consequently, this thesis is structured in to three parts. The first part introduces the experimental methods which are used in the experiments, starting with the principle of photoluminescence. Here, also excitonic states are shortly discussed, which lead to the formation of the optical band gap. In the following, the basics of Raman spectroscopy are recapped, highlighting the effect of resonant excitation, and also giving a quick introduction to electron-phonon coupling. In the end of the first part, the experimental setups in the laboratory are explained.

The second part deals with the project on wurtzite GaAs wires, while the third one

focusses on $MoSe_2$-WSe_2 heterostructures. Both of these parts are started by a theoretical introduction, explaining the most important background information necessary for the respective project. This is followed by the presentation of our experimental results. Both part two and three are ended by a separate conclusion on the results, and an outlook on the possible future path for the topics.

Part I.

Experimental methods

2. Excitons and photoluminescence

In this thesis, Raman measurements will be performed in resonant excitation, which means tuning the incident laser energy to hit excitonic states or band to band transitions of the material. Consequently, in order to understand the results, a brief look has to be taken on the electronic states that are created during resonant excitation and mediate the Raman or inelastic light scattering process. Therefore, a short introduction on the formation of excitons will be given, followed by the principle of photoluminescence, which is often used for the pre-characterization of our samples.

2.1. Formation of excitonic states

When creating electron-hole pairs by exciting electrons from valence to conduction band as in Fig. 2.1 (a), the Coulomb interaction between the two charge carries gives rise to a hydrogen like quasi particle, called exciton. Depending on the strength of this attractive interaction, two extreme cases can be distinguished: The Frenkel excitons, for which electron and hole are strongly bound and therefore found within the same or neighbouring unit cells, and the Wannier-Mott excitons, where electron and hole are weakly bound and find themselves several unit cells apart [15]. Since Frenkel excitons occur mostly in ionic crystals, and Wannier-Mott excitons are typical for semiconductors due to screening of Coulomb interaction by valence electrons, only the latter case will be discussed in the following.

The attractive coulomb potential is simply assumed to be

$$U(r) = -\frac{e^2}{4\pi\epsilon_0\epsilon r}, \tag{2.1}$$

where $r = R_e - R_h$ is the distance between electron and hole [16]. It is possible to separate the resulting Schrödinger equation into one for the center of mass R, and one for the relative motion using the reduced mass $\mu^{-1} = m_e^{-1} + m_h^{-1}$. Using the modified Rydberg energy R^*, one then obtains a series of excitonic states depending on the quantum number n:

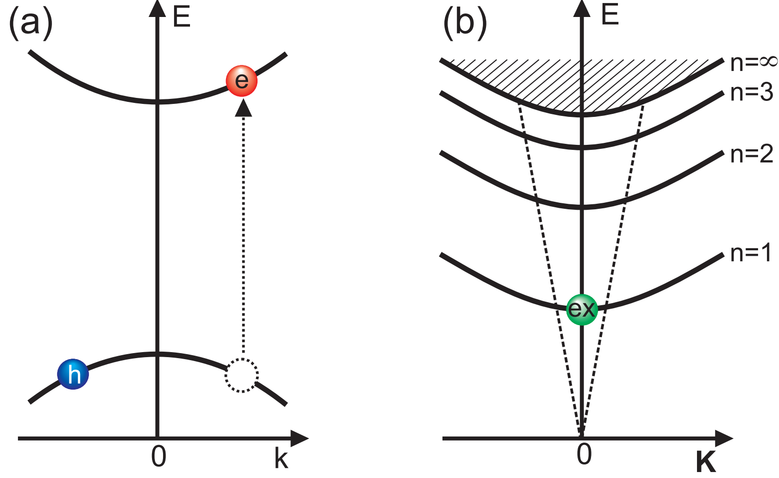

Figure 2.1.: *(a) Electron-hole pair in the single particle picture. The dashed circle marks the position of the missing electron, the hole sits at opposite k. In all following pictures, the position of the missing electron will be shown for simplicity. (b) Dispersion of excitonic states in the two-particle picture, where $K = k_e + k_h$. The dashed lines mark the light cone, which is the maximal momentum a photon can transfer to the crystal, corresponding to non-vertical transitions in (a).*

$$E_{(n)}(K) = E_\infty - \frac{R^*}{n^2} + \frac{\hbar^2 K^2}{2M} \qquad \text{with} \qquad R^* = \frac{\mu}{m_e \epsilon_r^2} R\,. \tag{2.2}$$

Here, E_∞ is the band gap energy for uncorrelated electrons and holes, whereas K and M are the total momentum and mass of the exciton. The second term in equation 2.2 gives rise to discrete excitonic states, which lie energetically below E_∞, while the third one describes the center of mass motion of the exciton. This formula is further illustrated in Figure 2.1 (b). Here, the dispersion of excitons is shown in the two-particle picture. The total momentum of the exciton is $K = k_e + k_h$, which is equal to the momentum a photon transfers to the crystal by exciting the electron-hole pair. In Fig. 2.1, this momentum is neglected, leaving a vertical transition in the single particle picture and an exciton with zero total momentum, as the momenta of electron and hole cancel each other. Photons do however transfer small amounts of momentum to the crystal (which will be discussed later in section 5.6), which produces slightly non-vertical transitions in the single-particle picture and gives a finite momentum to the exciton. The dashed lines in Fig. 2.1 (b) mark the maximal momentum a photon can transfer to the exciton or vice versa. Thus, excitons that lie outside of this region, which is called the light cone, can not recombine radiatively. In the end, it should be noted that while holes always

lie at opposite k compared to the corresponding electron, in all further pictures in this thesis the position of the missing electron (dashed circle in Fig. 2.1 (a)) will be used for simplicity.

2.2. Mott transition

The binding energy of excitons is strongly dependent on how strong the Coulomb interaction of electrons and holes is screened by their surrounding. It will be explained later in section 8.2.2, that for two-dimensional crystals binding energies are much higher than expected, since the electric field lines between the charge carriers extend into the surrounding vacuum [17]. The other way round, having high amounts of other charge carriers in the material decreases the binding potential by adding a screening factor to equation 2.1 [16],

$$U(r) = -\frac{e^2}{4\pi\epsilon_0\epsilon r}\exp\left(-k_s r\right) , \tag{2.3}$$

where the screening factor k_s is connected to the screening length by $\lambda_s = k_s^{-1}$, corresponding to the distance after which charger carriers do not interact any more. Increasing the charge carrier density therefore decreases λ_s, until it eventually reaches the size of the exciton Bohr radius. At this point, excitons will become unstable and transformed into an uncorrelated electron-hole plasma. This is known as the Mott transition, and the corresponding charge carrier density as the Mott density n_M.

However, a Mott transition does not necessarily lead to an rapid increase of the band gap energy, as one could expect when bound states "below" the band gap vanish. The reason is, that for sufficiently high electron densities, there is also a significant effect of band gap renormalisation present. Hereby, a correction to the electronic states is understood, that arises from the deviation of the single-particle picture at high carrier densities and leads to decreased values of the band gap. In many materials it is found that this reduction of band gap energy just compensates the increase due to the screening of excitonic states, which means the two effects cancel each other, and the band gap energy remains constant during the Mott transition. This also leads to the conclusion, that the Mott transition is in fact a gradual process of more and more excitons becoming uncorrelated, rather than a sharp transition for a certain excitation density.

2.3. Photoluminescence emission and excitation

The experimental technique used to measure the band gap energies in this thesis is photoluminescence spectroscopy (PL), which is the spontaneous emission of a photon after optically exciting electron-hole pairs or excitons [18]. This excitation is done by a laser of higher energy than the optical band gap, as shown in the first step of Fig. 2.2. In the next step, the charge carriers relax to the lowest available energy state. Thereby, they transfer energy and momentum to phonons in several small steps, since the mean scattering time of such relaxation processes is shorter that the radiative lifetime. In the third step, the electron-hole pair or exciton recombines by emitting a photon, that reflects the band gap energy.

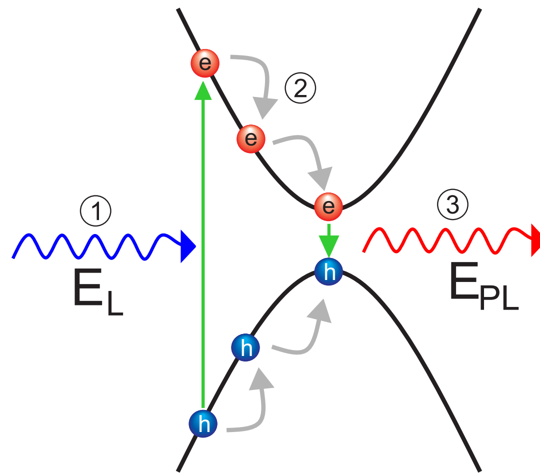

Figure 2.2.: *Illustration of the photoluminescence (PL) process. The electron-hole pairs or excitons created in step one relax to the lowest available state before radiative recombination takes place.*

In addition, PL can also be used to measure the absorption curve of a crystal, which is called photoluminescence-excitation (PLE). In such a measurement, the laser excitation energy is varied in small steps and the luminescence intensity is measured. Whenever the excitation hits an absorption maximum, more charge carriers will be created and also the PL will increase. Plotting the luminescence intensity as a function of the excitation, one will obtain an absorption curve of the crystal. The great advantage of this method over standard absorption spectroscopy is, that it can be applied for all sizes and surface shapes, which is why it will be used for single GaAs nanowires in this thesis.

3. Raman spectroscopy

In the following chapter, we will have a look on the basic mechanisms of the main experimental technique used in this work, which is Raman spectroscopy or inelastic light scattering. These two terms both refer to inelastic scattering of light by a medium, but per definition in Raman spectroscopy the light is scattered by optical phonons, while the more general expression inelastic light scattering is used when photons are scattered by the electronic system of the medium [4]. The process for phonons will be discussed here, and the corresponding electronic scattering in section 5.6.

3.1. Basic principle of Raman spectroscopy

In Raman scattering, an optical phonon in the crystal is either created or annihilated by interaction with a photon. The creation of phonons in the medium is hereby called Stokes process, the annihilation Antistokes process. Both processes have to fulfil momentum and energy conservation, which leads to

$$\vec{k_S} = \vec{k_I} \pm \vec{q} \tag{3.1}$$

$$\hbar\omega_S = \hbar\omega_I \pm \hbar\Omega \,, \tag{3.2}$$

where $\vec{k_S}$, $\vec{k_I}$ and ω_S, ω_I are the wave vectors and frequencies of the scattered and incident photons, while q and Ω belong to the phonon that is created $(-)$ or annihilated $(+)$. For the Antistokes process, the phonon must already exist in the medium before the scattering process. Therefore, the intensity of the Antistokes process follows the Bose-Einstein distribution n and vanishes for low temperatures, while Stokes scattering depends with $n+1$ on temperature [3].

Since the momentum of photons can be neglected compared to that of crystal atoms, it follows from momentum conservation that only optical phonons with $q \approx 0$, at the Γ-point of the Brillouin zone, can take part in the scattering process. From equation

(3.2) one can see the typical form of a measured Raman spectrum, which is plotted in Fig. 3.1. The energy of the Stokes and Antistokes scattered light is shifted to either sides of the elastically scattered laser beam, which defines the zero on the energy scale. The energetic difference between elastically and Raman scattered light is called the Raman shift, and is independent of the laser wavelength. This leads to an important criterion to distinguish Raman and PL effects in the spectrum: When varying the laser energy, Raman modes maintain a constant shift relative to the laser, while PL peaks, which have a constant absolute energy, change their position in the Raman spectrum.

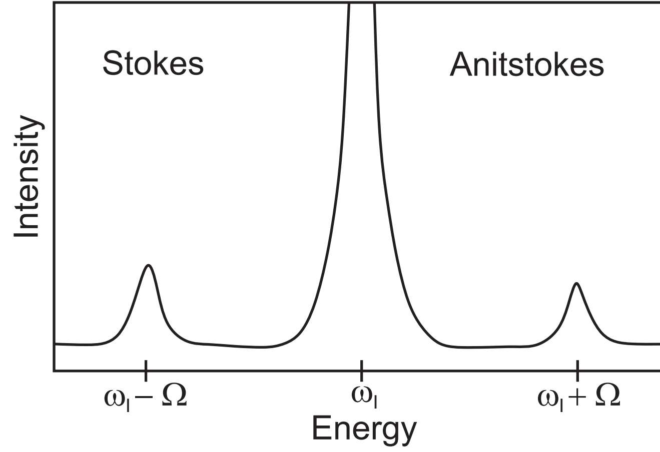

Figure 3.1.: *Schematic picture of a Raman spectrum. The elastically scattered laser appears in the middle, while Stokes and Antistokes lines are shifted to either sides on the energy scale. Inspired by [4].*

For a macroscopic picture of Raman scattering [15], we take a look on the polarization an oscillating electric field of the form

$$E(r,t) = E_I(k_I,\omega_I)\cos(k_I \cdot r - \omega_I t) \ , \tag{3.3}$$

that presents the incident light, induces in a crystal. The resulting polarization will be determined by the susceptibility $\chi(k_I,\omega_I)$, and is oscillating with the frequency of the incident electric field:

$$P(k_I,\omega_I) = \chi(k_I,\omega_I)\,E_I(k_I,\omega_I) \ . \tag{3.4}$$

At finite temperature, there are however fluctuations in the crystal that influence the susceptibility. In this case, these fluctuations are phonons that can be written as plane waves in the following form:

$$Q(r,t) = Q(q,\Omega)\cos(q \cdot r - \Omega t) \ . \tag{3.5}$$

Since the light frequencies in the visible range will be much higher than those of the phonons, their modification of the susceptibility can be expressed as a Taylor series of the lattice displacements $Q(r,t)$ as

$$\chi(k_I, \omega_I, q) = \chi_0(k_I, \omega_I) + \frac{\partial \chi}{\partial Q} Q(r,t) + \cdots \ , \tag{3.6}$$

where the second term is the oscillating part of the susceptibility, induced by the lattice displacements. When inserting equation (3.6) into (3.4), we get two parts: the first one stays unchanged by the lattice displacements and oscillates with the frequency of the electric field. It thus represents elastic Rayleigh scattering. The second term contains the modified term in the susceptibility and a mixing of light and phonon frequencies:

$$\begin{aligned} P_{ind}(r,t,Q) &= \frac{1}{2}\frac{\partial \chi}{\partial Q} Q(q,\Omega) E_I(k_I, \omega_I t) \\ \cdot\{\cos[(k_I + q) r - (\omega_I + \Omega) t] &+ \cos[(k_I - q) r - (\omega_I - \Omega) t]\} \ , \end{aligned} \tag{3.7}$$

which gives the Stokes (-) and Antistokes (+) frequencies and energies already introduced in equation (3.1) and (3.2). The more important conclusion from (3.7) is, that only phonons that modify the susceptibility contribute to the Raman spectrum. These are then called Raman active modes. Other phonons, that modify the polarization directly are called infrared active, modes that do neither of the two are called silent. In non-centrosymmetric crystals, it is possible that phonons are both Raman and infrared active at the same time, which is the case for all material systems examined in this thesis.

The quantity $\frac{\partial \chi}{\partial Q} Q$ in (3.7) is called the Raman tensor R. It not only shows whether a vibration mode is Raman active at all, together with the light polarization of incident and scattered light it also defines selection rules, that determine in which scattering geometries a phonon can be found in the Raman spectrum. These selection rules can be found via the formula

$$I_S \propto |e_i \cdot R \cdot e_S|^2 \ , \tag{3.8}$$

where I_S is the Raman intensity and e_I and e_S the polarization of incident and scattered light.

When expanding the Taylor series in (3.6) to one more order the two-phonon spectrum is included, where Raman peaks differ by $\pm\Omega_a \pm \Omega_b$ from the laser frequency, with Ω_a and Ω_b being the frequencies of the phonons that are either created or annihilated. Creating two phonons is called a sum process, creating one and annihilating another of smaller energy a difference process. The special case that two identical phonons are created is called the overtone of a certain phonon. In these processes, the condition that only phonons from the Γ-point can participate is not needed any more, since it is sufficient that the momenta of the two phonons add up to zero. In contrast to one-phonon scattering, this often makes it possible to draw conclusions about the phonon density of states in the Brillouin zone. For difference processes, one of the phonons must already exist in the crystal before scattering, which makes them only observable at sufficiently high temperatures, similar to the Antistokes process.

3.2. Mediation by the electronic system

In this section, we will take a look on the effect the excitation energy has on the intensity of the Raman scattered light. Varying the laser wavelength, one often finds resonances of the scattered light in the vicinity of electronic band gaps or excitonic transitions of the crystal. These resonances show up due to the mediation of Raman scattering by the electronic system, which happens in three steps. In the following, resonance effects will be discussed for the Stokes process only. These can be described by the following formula:

$$M = \sum_{\nu,\nu\prime} \frac{\langle i| H_{eR}(\omega_I) |\nu\rangle \langle\nu| H_{e-ion} |\nu\prime\rangle \langle\nu\prime| H_{eR}(\omega_S) |f\rangle}{(E_\nu - \hbar\omega_I - i\Gamma_\nu)(E_{\nu\prime} - \hbar\omega_S - i\Gamma_{\nu\prime})}, \tag{3.9}$$

where M gives the Raman scattering amplitude. In the numerator of equation 3.9, there are three transitions, which describe how phonons are created when photons are absorbed and re-emitted by the medium. In the first step, an incident photon of energy $\hbar\omega_I$ creates an electron-hole pair, transferring the system from its initial state $|i\rangle$ to the first intermediate state $|\nu\rangle$, that is in general a virtual electronic state. Next, this virtual state is scattered into a second virtual state $|\nu\prime\rangle$ by the electron-phonon interaction Hamiltonian H_{e-ion}, and a phonon is created in the medium. Lastly, the electron-hole pair recombines into the final state $|f\rangle$. Since the electronic system stays unchanged in the Raman process, the final state is identical to the initial one from the electronic point of view. The only difference between $|i\rangle$ and $|f\rangle$ is the phonon that was created.

When talking about resonant Raman spectroscopy, one means that at least one of the intermediate virtual states becomes a real electronic state of the system. We can see the effect on the Raman amplitude in the denominator of equation 3.9. When the first intermediate state $|\nu\rangle$ is a real electronic state, and the laser energy is chosen to be $E_\nu = \hbar\omega_I$, the first term in the denominator becomes minimal and increases the scattering amplitude. This case is called an ingoing resonance (see also Fig. 3.2 (b)). If the second intermediate state is real and its energy is equal to $\hbar\omega_S$, we have an outgoing resonance. The special case that both intermediate states are real is then a double resonance. Γ_ν and $\Gamma_{\nu\prime}$ are damping constants that give rise to the finite lifetime of the sates $|\nu\rangle$ and $|\nu\prime\rangle$. Since there can also be a series of real states in the system, the sum over all possible intermediate states has to be taken in equation 3.9.

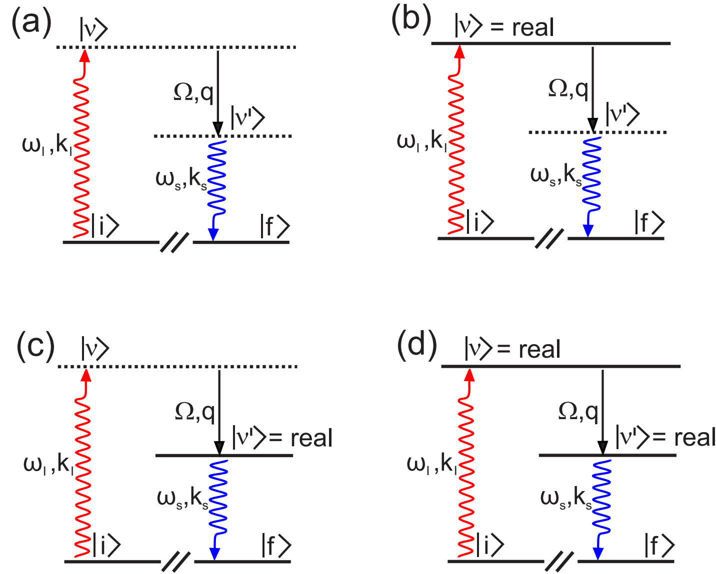

Figure 3.2.: *Energy levels of the electronic mediation in Raman scattering. Dotted lines are virtual, solid ones real electronic states. The axis break between $|i\rangle$ and $|f\rangle$ implies that while the electronic system stays unchanged, a phonon is created in the material during the process, and the initial and final states are not identical. (a) non-resonant case (b) ingoing resonance, (c) outgoing resonance (d) double resonance.*

For mediating the Raman process, uncorrelated electron hole-pairs as well as excitons can serve as intermediate states [19]. Typically, the measured resonance curves turn out sharper and stronger for excitonic states than for band to band transitions [20, 21]. Another effect that is commonly known for GaAs, is that the outgoing resonance is stronger than the ingoing one for a mediation by excitonic sates. This can be explained by the fact that for a excitonic series of real states, one excites into the excitonic con-

tinuum with the incident photon and hits the ground state of the Rydberg series with the re-emitted photon, which makes the outgoing process quasi double resonant [22].

3.3. Electron-phonon coupling

In the last section, it was discussed how tuning the laser energy to hit real electronic states leads to resonances in Raman scattering. There is however another important requirement for the observation of Raman resonances than the laser wavelength, and that is the electron-phonon interaction. In equation 3.9, we can see that the scattering between the two intermediate states which creates a phonon is determined by the electron-phonon interaction Hamiltonian H_{e-ion}. Therefore, resonances will be found only if there is an significant electron-phonon coupling mechanism for the chosen phonon mode and scattering geometry. The two most important interactions are introduced in the following.

3.3.1. Deformation-potential interaction

The most common form of electron-phonon interaction is the so called deformation-potential interaction, which is a direct consequence of the Born-Oppenheimer approximation [15]. According to this rule, due to the much larger masses of the ions in a crystal, the electrons can react almost instantaneously to ionic motion, while the ions themselves see electrons only as a time averaged potential. Therefore, the Hamiltonian H_{e-ion} can be written as a Taylor expansion of the electron Hamiltonian H_e with respect to the atomic displacements ∂R_j from the lattice equilibrium position:

$$H_{e-ion}\left(r_j, \partial R_j\right) = \sum_j \left(\frac{\partial H_e}{\partial R_j}\right)\Bigg|_{R_{jo}} \cdot \partial R_j \cdots \tag{3.10}$$

Or in other words, the electron-phonon interaction is the change in electronic energy due to deformations in the observed potential induced by the movement of lattice atoms. Since the electronic Hamiltonian H_e is not necessarily known most of the time, it is common to approximate this expansion by the induced change in the band energies E_{nk}:

$$\left(\frac{\partial H_e}{\partial R_j}\right)\Bigg|_{R_{j0}} \cdot \partial R_j \approx \left(\frac{\partial E_{nk}}{\partial R_j}\right)\Bigg|_{R_{j0}} \cdot \partial R_j \,. \tag{3.11}$$

For optical phonons, the displacement of lattice atoms does not lead to a macroscopic strain, due to the out-of-phase oscillation within one unit cell. The amount of shift

for the band edge energy is therefore given by the optical phonon deformation potential $D_{n,k}$, using the microscopic displacements u of crystal atoms within one unit cell relative to their equilibrium distance a_0:

$$\partial E_{n,k} = D_{n,k} \frac{u}{a_0} \, . \tag{3.12}$$

3.3.2. Fröhlich interaction

In polar crystals, there is another electron-phonon interaction that only works for optical phonons. The out-of-phase vibration of different kinds of atoms in a unit cell can induce an oscillating electric field, that can directly interact with the electronic band states. This coupling mechanism is called Fröhlich interaction [15]. This process plays an important role for the resonances of the LO phonon in GaAs [22, 23]. This phonon mode and also its overtones show strong resonant enhancement due to Fröhlich interaction, even when being Raman forbidden in the chosen measurement geometry. Therefore, this mechanism is mostly discussed for the GaAs LO phonon.

The Hamiltonian that describes the interaction of LO phonons with the band structure due to the oscillating electric field is

$$H_{Fr} = \sum_q \frac{iC_F}{q} \{c_q^+ \exp\left[i\left(q \cdot r - \Omega_{LO} t\right)\right] - cc\} \, , \tag{3.13}$$

where the coefficient C_F is

$$C_F = \frac{e}{\sqrt{4\pi\epsilon_0}} \sqrt{\frac{2\pi\hbar\Omega_{LO}}{NV} \left(\epsilon_\infty^{-1} - \epsilon_0^{-1}\right)} \, . \tag{3.14}$$

Here, Ω_{LO} and q are the LO phonon frequency and wave vector, e is the elementary charge, N the number of unit cells per unit volume and V the volume of one primitive cell. We can see that the strength of Fröhlich interaction mainly depends on the low and high frequency dielectric constants ϵ_0 and ϵ_∞, which facilitates its calculation. Interestingly, the coupling also depends on q^{-1}, which means it diverges at the Γ point and predominantly enhances zone center phonons.

4. Experimental setup

In the following, the experimental setup that enables PL and Raman experiments in our laboratory will be introduced. The first part explains how the available laser and spectrometer are used to build a micro Raman setup, while the second part summarizes the integration of an Attocube positioning system into an Oxford instruments magnet cryostat, that was done within this thesis.

4.1. Micro-Raman setup

Fig 4.1 shows the main principle of the experimental setup used for Raman measurements. The setup is specially built for resonant excitation in the near infrared range, which is why a continuous wave Ti:Sapphire laser by Spectra-physics is used as the light source. This optically pumped laser is tunable in the range of 715 - 1000 nm, delivering an output power of up to 1 W, for optimal wavelength and resonator adjustment. It does however contain side modes next to the amplified laser wavelength, which would hinder the observation of Raman modes. Thus, a tunable laser line filter with a small bandwidth is used, which only lets pass the central laser wavelength. Since the Ti:Sapphire laser emits light that is horizontally polarized, and the line filter only works for vertically polarization, a half wave plate is always placed between the two elements. Unfortunately, the line filter strongly affects the laser line profile, which is enlarged to about a square centimetre when exiting the filter. To make up for this inconvenience, a beam expander is placed vice versa after the line filter, which reduces the beam profile close to its original size.

The again collimated laser beam is then directed to a 100X Nikon microscope objective with a numerical aperture of 0.8, which focuses the light down to a 1-2 µm spot on the sample. The sample itself sits in a CryoVac cryostat, that is cooled to 4 K by continuous helium flow. Placing the cryostat on a Steinmeyer xy-table allows to adjust the sample position under the focused laser beam. The microscope objective also collects the backscattered light of the sample, which is later coupled out by a cube beamsplitter, that

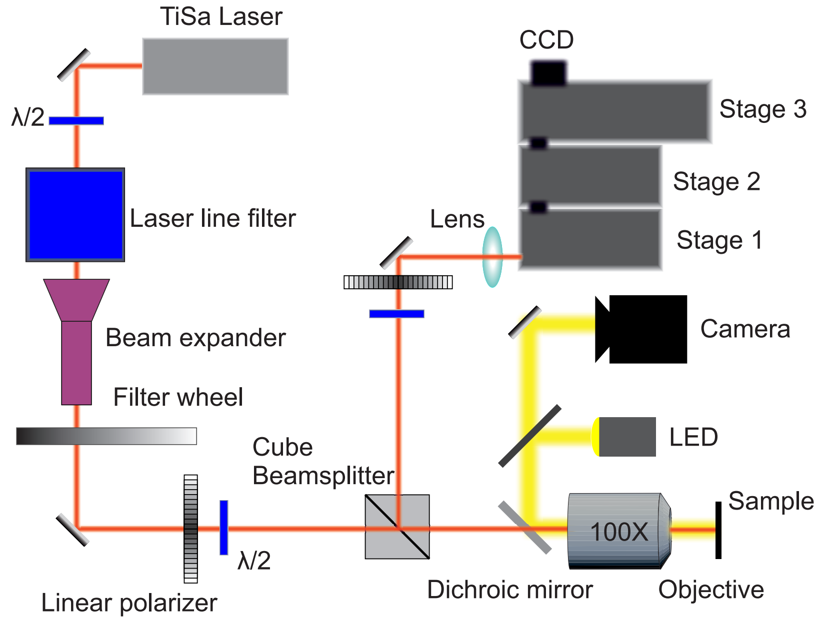

Figure 4.1.: *Illustration of the experimental setup used for all Raman measurements. In case of some PLE experiments on nanowires, the laser line filter was not used.*

was chosen for its very high light polarization conservation. The reflection/transmission ratio of the beamsplitter is 90:10. That way, most of the light that is backscattered by the sample can be coupled out to the spectrometer, allowing to keep the laser power as low as possible in order to achieve a certain count rate of signal. The power that is illuminated on the sample is always measured directly before the objective. This power is adjusted by using a filter wheel, that is continuously tunable between optical density 0 and 2, and is placed behind the beam expander. The polarization of the laser light is selected by a linear polariser and half wave plate, that are placed before the beamsplitter for the incident light, and after it for the out-coupled light that comes from the sample.

To monitor the position of the focused laser on the sample, the white light of a LED is directed onto a 50:50 plate beamsplitter, that lets half of the backscattered white light from the sample through to a camera. Since the cube beamsplitter mentioned earlier is specified for the near infrared range, it does not work for the white light, which requires a separate beamsplitter to couple the white light into the microscope objective. Using a dichroic mirror, that reflects only light with wavelengths shorter than 650 nm, nearly all of the white light can be coupled in and out, without significantly influencing the power of the transmitted laser. The beam path of the laser light is however slightly altered by

the dichroic mirror, which is why it is placed on a flip mount, and is taken out of the beam path for any fine adjustments and all the measurements.

In the end of the beam path, the scattered light is focused on the entrance slit of a triple Raman spectrometer (Princeton instruments) by a lens with focal length of 3 cm. The spectrometer consists of three stages, each equipped with a diffraction grating. In the first stage the light is spectrally expanded, and directed onto the slit towards the second stage in such a way, that the wavelength of the elastically scattered laser light is filtered out. The second stage then reverses the spectral expansion of the first stage, before the third stage produces the spectral resolution for the measured spectra. In each stage, there are three different diffraction gratings selectable. In this thesis, the first two were always used with the 900 lines/mm grating, and the third one with 600 lines/mm. For light in the near infrared, these gratings are only sensitive to horizontally polarized light. Therefore, it is not possible to detect unpolarized light, and all measurements in this thesis are either for the co or cross polarized case. The signal in the end of the third stage is detected by a CCD chip, which is cooled to −120 °C by liquid nitrogen, reducing the dark current.

Some of the sample characterization measurements in part III about $MoSe_2$-WSe_2 heterostructures were done using a green laser (2.33 eV), a single stage Raman spectrometer and a set of Bragg filters for blocking the laser line. The advantage of using Bragg filters lies in the fact, that only the laser frequency is blocked, and therefore the Stokes and Antistokes sides can be recorded simultaneously. The disadvantage is of course, that the laser energy is not tunable. Hence, this setup was only used for pre-characterisation. If not specifically noted, all measurements were done using the setup in Fig. 4.1.

4.2. Microscope setup for magnetic fields

During the experimental part of this thesis, it became necessary to perform measurements using an external magnetic field. In the laboratory where the Ti:Sapphire laser and triple Raman spectrometer are operated, there is a magneto cryostat by ICE Oxford available, that is built to reach magnetic fields up to 9 T. Unfortunately, these kind of bath cryostats do not allow to focus the laser light by a microscope objective, which was needed for all samples investigated in this work. It was therefore decided to use the Microstat MO model by Oxford instruments, which is a continuous flow cryostat capable of fields up to 5 T, and has a window compatible for microscope objectives. So far, this cryostat had however only been used for measurements on wafer pieces, that

did not require a micrometer precise positioning of the laser spot on the sample, which is however necessary for all samples used in this work. Since the cryostat is simply to heavy to place it on top of a xy-table as done with the CryoVac model, it was necessary to use a positioning system that can be put inside the cryostat. This was realized by two Attocube ANPx51/RES linear horizontal steppers. These piezo driven positioners are specified to work at down to 10 mK and for fields up to 31 T, the minimum step size is 10 nm with a maximal travel range of 3 mm. Their base area measures 15 x 18 mm, with a height of 9.2 mm. While this means they easily fit inside the sample chamber of a bath cryostat, a lot of work was necessary to adapt the Microstat MO to be compatible with this positioning system, which will be summarized in the following.

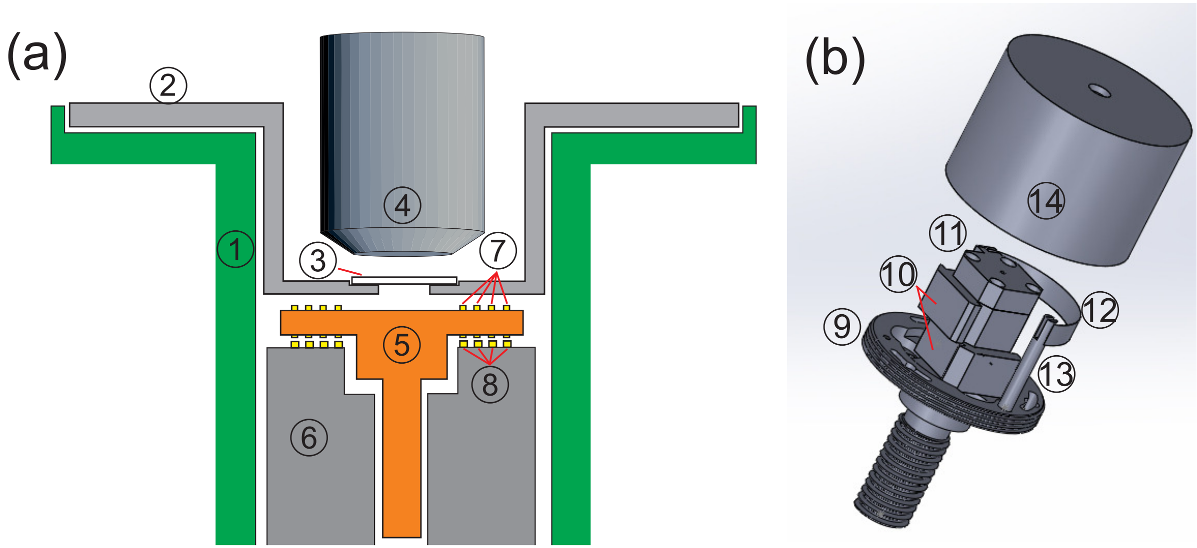

Figure 4.2.: *(a) General construction of the Microstat MO cryostat sample chamber without the Attocube system. (1) Side walls of the sample chamber, not cooled by helium (2) Frame of the cryostat window (3) Cryostat window,* 0.5 mm *tick (4) Microscope objective (5) Sample holder (6) Mount for the sample holder, delivering the cooling via mechanical contact (7) Contact pins for electrical applications (8) Gold contacts on the mount (b) Technical drawing of the new sample holder including the attocube system (9) Thread for mounting the heat shield (10) Attocube positioning system for x- and y-direction (11) Copper plate for mounting the sample (12) and (13) Heat contact for cooling the sample (14) Heat shield*

The Microstat MO has two separate vacuum chambers, one for the magnet coils and one for the sample, each of which having their own helium circuit. The cross section of the sample chamber is illustrated in Fig. 4.2 (a). The side walls (1) are not cooled by any helium circuit and are separating this chamber from the magnet coils at the outside

of it (not shown). The window frame (2) made of aluminium contains a 0.5 mm thick window made of spectrosil B, and allows a microscope objective (4) to focus light on the sample. The sample holder (5) is screwed into its mount (6), which means the cooling happens via this mechanical contact. For changing the sample, the holder is taken out of the cryostat by a special tool (not shown). For electrically contacting the sample, the holder has 12 contact pins (7), which are arranged in three groups of four, and are pressed onto gold contacts on the sample mount (8) when screwing the holder into the cryostat.

Figure 4.2 (b) shows a technical drawing of the sample holder that includes the two Attocube positioners (10). In order to provide enough space for the lower cube on the holder, it was necessary to reduce the number of contact pins to ten. This happens to be the number of needed contacts, as each positioner has five cables. The cubes are fixed by screws, which means threaded holes were added to the sample holder for the lower one. On top of the upper cube, there is a copper plate for mounting the sample (11). Since the cubes are not designed to cool a sample by conducting heat away, the copper plate has a direct heat contact to the sample holder below. This consists of several thin copper plates (12), that are soldered to a copper stick standing on the sample holder (13). Since the cubes maximal force along one axis is 1 N, it was important that the mechanical resistance of the heat conductor lies below that value, which limits the maximal heat capacitance. To ensure the sample could still be cooled down, the heat capacitance of the parts (12) and (13) and the amount of thermal radiation on the sample by its surrounding were estimated. Since the side walls of the sample chamber are not cooled, their thermal radiation adds to that through the cryostat window and lies at about 1.5 W. The thermal conductance of the heat contact on the other hand is only about $50\,\mathrm{mW\,K^{-1}}$, which would not be sufficient to keep the sample close to 4 K. To solve this problem, a heat shield (14) had to be used for reduction of thermal radiation, which is screwed down by an additional thread at the side of the sample holder (9) and hereby also cooled down. The estimated value of thermal radiation that goes through the heat shield hole at the top is only about 3.5 mW, allowing the heat conductor to keep the sample close to liquid helium temperatures. All parts shown in Fig. 4.2 (b) are made of oxygen free copper and gilded (except for the Attocubes themselves), and were fabricated by the mechanic factory of the faculty. In addition to the parts shown in the figure, a new window frame providing more space for the positioning system had to be built, as well as a modified tool for screwing the sample holder into the cryostat, and a new tool for screwing the heat shield to the sample holder.

The electrical connections for controlling the Attocubes were made using the ten remaining contact pins on the sample holder. The maximal electric resistance for running the cubes is $2.5\,\Omega$, however the cables in the cryostat running from the outside plug to the sample holder contact (8) had a resistance of about $60\,\Omega$. Soldering new cables in this value could be reduced to $1.5\,\Omega$. Finally, an adapter cable was made to connect the outside plug on the cryostat to the attocube controller.

Also the experimental setup surrounding the magnet cryostat had to be rebuilt, since the former setup is placed on an optical table with a ferromagnetic plate that is not suitable for magnet cryostats. The new setup does however consist of the same beam splitters and polarization optics, and hence is in principle the same.

In operation the spectral position of PL lines showed that the sample reaches temperatures comparable to what we know from the CryoVac cryostat. Running the positioners at low temperatures also works sufficiently well. The only inconvenience that appeared in operation is a slight hysteresis when changing the drive direction of the upper Attocube, which is most probably due to the mechanical force of the heat conductor. This excludes the positioning system from being used to scanning operation of two dimensional arrays. The second disadvantage that comes with this cryostat rebuilding, is that there are no electrical connections left for contacting the sample. This is however still possible when using the original sample holder; as new parts were built instead of modifying the old ones, the cryostat can be used at any time in its former configuration. The only thing that was changed permanently is the cable resistance between the outside plug and sample chamber.

Part II.

Intersubband excitations in wurtzite GaAs wires

Having described the basic principles of the chosen experimental technique and the available setup in our laboratory, we will now come to the first of two main topics in this dissertation: Measuring the one-dimensional subband structure of ultra thin wurtzite GaAs wires by inelastic light scattering. Doing this, we exploit the recent advances in the fabrication of MBE grown core-shell nanowires, which have succeeded in reducing the wire diameter to just a few tens of nanometers and therefore offering sufficiently high confinement energies [24]. The nanowires used in this work were grown in the group of Prof. Dominique Bougeard, mainly by Florian Dirnberger, and have core diameters of down to 25 nm.

Chapter 5 will introduce the growth process that was used to obtain the wires that were measured in the Raman experiments. Next, the theoretical background of wurtzite GaAs will be introduced, including the differences on phonon dispersion and electrical band structure compared to zinc blende GaAs. Lastly, the effect of confinement and its reported evidence in literature to this day will be discussed.

Finally, we will present our experimental results in chapter 6, which are obtained by inelastic light scattering, photoluminescence and photoluminescence-excitation. We find a series of Raman peaks, which can be interpreted as intersubband excitations of electrons and holes. The extracted values for the subband splittings and absorption peaks are compared to k·p band structure calculations derived by Paulo de Faria Junior, which can nicely reproduce the experiment. Most of the data in this chapter were published in Phys Rev B [25].

5. Theoretical background and state of the art

5.1. Synthesis of ultra thin core-shell wires

The nanowires used in this work were grown by Florian Dirnberger, using a Molecular Beam epitaxy (MBE) setup and the so called Vapour-liquid-solid (VLS) growth method. This process was first discovered by Wagner and Ellis in 1964 [26], and its basic principle can be seen in Fig. 5.1. The parameters that were used in this case can be found in more detail in [27], but a short summary will be given in the following.

As a first step, a gold layer of 0.05 Å is deposited onto a GaAs(111)B wafer. This wafer is transferred to the MBE chamber, where a constant background pressure of As Atoms is applied for the whole time, preventing As atoms in the substrate from evaporating. Heating up the wafer then leads to a formation of liquid gold/gallium nanodroplets on its surface, which act as a sort of catalyst for the formation of a wire. The actual growth process is started by applying a flow of Ga atoms into the chamber. These are absorbed by the liquid nanodroplet, which is accompanied by surface diffusion of atoms from the substrate, which together creates a supersaturation in the nanodroplet. Consequently, condensation occurs at the interface of droplet and substrate. The result is the growth of a GaAs nanowire with hexagonal cross section, whose diameter gets thicker for longer growth times, since for a certain wire length the atoms from surface diffusion do not reach the nanodroplet any more, and condensate directly at the side walls. The growth time together with the initial size of the droplet therefore determines the wire diameter; varying the time between 20-125 minutes increases the diameter from 20 to 110 nm and the length from 1 to 5 µm. Stopping the Ga flow terminates the growth of the wire, still maintaining the As background pressure.

Since a GaAs wire alone would suffer from significant loss of PL intensity due to surface trapped states [29], an $Al_{0.32}Ga_{0.68}As$ shell of nominally 15 nm thickness is added after the GaAs core is finished. To prevent this shell from oxidizing, the wires are finally

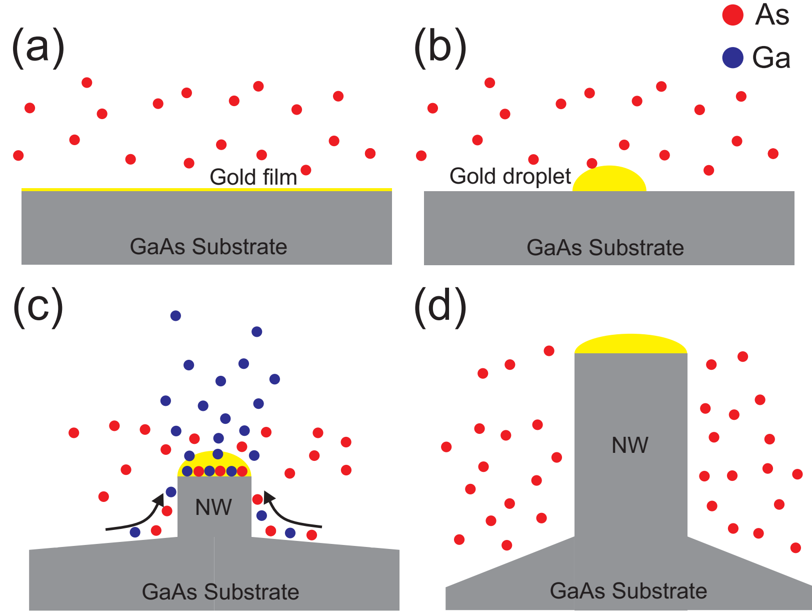

Figure 5.1.: *Schematic explanation of the VLS-method. (a) A thin gold layer is deposited on top of a GaAs wafer. The substrate is transferred to the MBE chamber, where a constant As background pressure is maintained. (b) The gold film forms a droplet when heated up. (c) The gold droplet then acts as a catalyst for Ga and As atoms, which condensate at its bottom to form a nanowire. (d) Since also diffusion from the substrate to the sides of the nanowire occurs, the wire has grown in hight and diameter at the end of the growth process. Inspired by [27, 28]*

capped with 7.5 nm of GaAs in the last step of the fabrication. This usage of protection layers ensures the suppression of non-radiative recombination via surface states [30]. A SEM (scanning-electron-micrograph) picture of a finished wire is shown in Fig 5.2 (a). This particular wire has a core diameter of approximately 25 nm, but already contains its shell and cap layer, making it broader in the picture.

For our purposes the wires need to be lying on a substrate, since we have to transfer photon momentum perpendicular to the wire axis in order to excite intersubband excitations. Therefore, the wires are broken off the growth substrate in an ultrasonic bath, and the liquid containing the wires is dropped on a Si-substrate with a 300 nm thick SiO_2 layer on top. After drying out, the wires are lying on this substrate, as shown in Fig. 5.2 (b). The gold numbers are used for orientation, as it is not possible to see the wires in the white light image of our measuring setup. Since not every wire shows a defect free PL emission, we have pre-selected wires which show a defect free, single PL emission peak at low excitation powers.

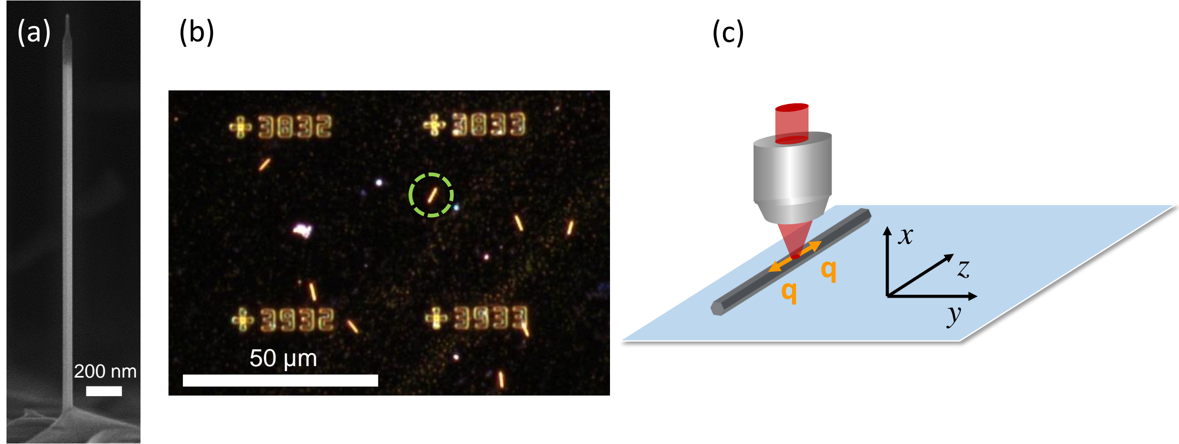

Figure 5.2.: *(a) SEM picture of an as grown nanowire standing on the growth substrate. The core diameter is approximately* 25 nm*, but the total diameter is larger due to the shell and cap layers. (b) Microscope image of wires dispersed on a Si-substrate that contains gold numbers for orientation during measurements. The green circle marks one of the single wires. (c) Coordinate system that is used to define the polarization configuration in Porto notation. A finite photon momentum q is transferred along the wire axis due to the numerical aperture of the objective.*

In figure 5.2 (c), the measurement geometry is illustrated. The plane in which the wire lies on the substrate is given by the coordinates y and z, with z being the growth direction of the wire. Therefore, x is the direction of light excitation and emission. This coordinate system will be used from now on to define the polarization configuration, using Porto notation, which is given in the form $\bar{k_I}\,(\epsilon_I, \epsilon_S)\,k_S$. Here, k_I and k_S are the propagation directions of the incident or scattered light, and ϵ_I and ϵ_S the directions of the linear light polarization. For example, exciting a wire with light polarized parallel to its growth direction, but detecting the light that is emitted perpendicular to it, is noted by $\bar{x}\,(z, y)\,x$. Fig. 5.2 (c) also shows the transfer of a finite photon momentum q along the wire growth direction, due to the numerical aperture of the used objective. This will be discussed later in section 6.4.3.

5.2. Formation of wurtzite crystal structure

Apart from the dimensionality of the wires, there is another striking difference between GaAs wires and bulk GaAs: Depending on the growth conditions, it is possible they condensate in the wurtzite crystal phase instead of zinc blende. The wires used in this

thesis are fabricated to posses a pure wurtzite phase structure, as shown by electron diffraction patterns [8].

The wurtzite and zinc blende crystal structures are compared in Fig. 5.3. As shown in this drawing, the two crystal structures differ mainly in their stacking order along the zinc blende [111], or the wurtzite [0001]-direction. For the zinc blende case, an ABCABC stacking is found, where each letter stands for a layer of Ga and As atoms (a). For wurtzite on the other hand, the C layer is missing and thus an ABAB stacking is formed (b). The ABC stacking is equivalent to two intertwined fcc lattices (one each for Ga and As atoms), the wurtzite to two hcp lattices. The usage of four indices for crystal directions and planes for wurtzite is also a consequence of the hexagonal form, as different indexing can form equivalent crystal planes in hexagonal lattices [31]. The [0001]-direction shown in Fig 5.3 (b) is also the wire growth direction and will be called c-axis from now on. For an ideal wurtzite crystal, the lattice parameters can be derived from the zinc blende form as $a_{wz} = a_{zb}/\sqrt{2}$ and $c = \sqrt{8/3}a_{wz}$ [32], where c is the lattice constant along the growth direction and a perpendicular to it. Experimental values are $a = 3.98\,\text{Å}$ and $c = 6.56\,\text{Å}$ [33].

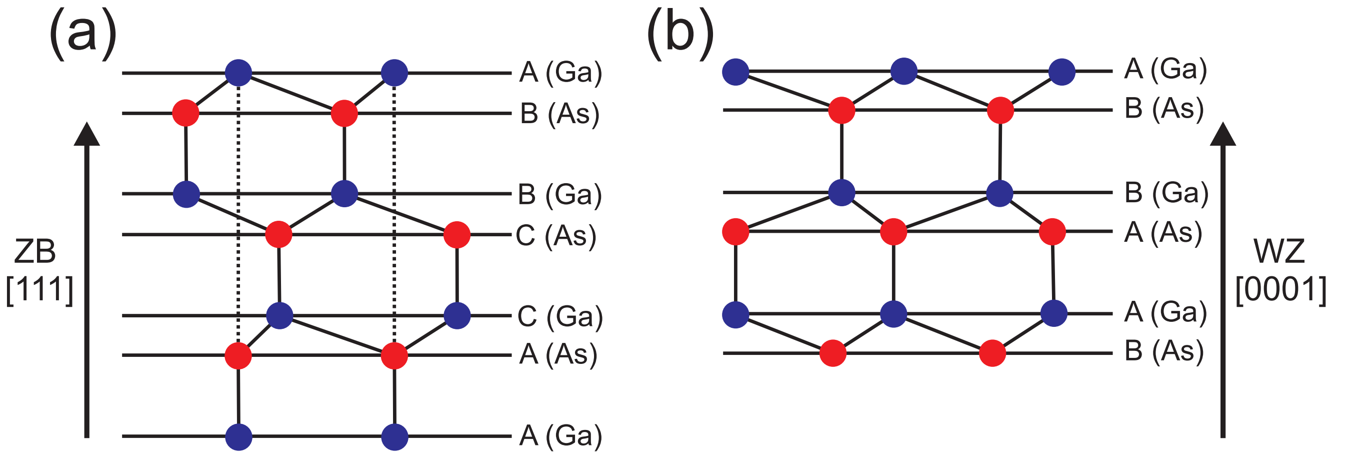

Figure 5.3.: *(a) Two-dimensional cross section of zinc blende GaAs, showing the stacking along the [111] crystal direction. The stacking order is ABCABC, with each letter standing for a layer of Ga and As atoms. (b) Cross section of wurtzite GaAs, showing the stacking along the [0001]-direction. Here, the stacking order is ABAB. Inspired by [15].*

The zinc blende and wurtzite structure thus only deviate from one another concerning the position of the third nearest neighbour for every atom, resulting in quite similar electronic properties, which will be shown later. There is however a difference in stacking

energy per atom between the two structures of about 12 meV [34], favouring the zinc blende over the wurtzite lattice. Consequently, bulk GaAs in wurtzite structure can only be found in a high temperature and pressure regime [33]. Hence, the question arises why GaAs nanowires can be found in the energetically unfavourable crystal structure.

The first and rather intuitive guess to answer this question, is the surface to volume ratio and small diameter of the wires, as it was argued by different groups [35, 36]. The problem in this picture is however, that critical diameters for which the wurtzite crystal structure should be stable, were predicted far to low. Therefore, the solution was identified in the VLS-growth process itself. It was found by Glas et al. [37], that the wurtzite phase occurs if the nucleation in the gold droplet happens at the triple-phase line. That means, the nucleus forming the wire is attached to gold, the growing wire and vacuum at the same time. It was later shown that also other parameters, like shape and volume of the droplet, together with the position of the nucleus are important [38].

As a consequence, wurtzite GaAs wires do not necessarily have to have a small diameter. It is either possible to grow bulk like wurtzite wires measuring several hundreds of nanometers in diameter [9], or on the contrary, grow ultrathin GaAs wires of just a few nanometers thickness in zinc blende structure [39]. Also changing the wire crystal structure during growth according to the conditions in the process has been demonstrated [40].

5.3. Raman spectroscopy of wurtzite wires

In the following chapter, the evidence of condensation in the wurtzite phase that is found in Raman measurements, will be discussed briefly. Raman spectroscopy is a well suited tool to experimentally differentiate between the zinc blende and wurtzite phase in nanowires.

The phonon dispersion of wurtzite GaAs is plotted in Fig. 5.4 (a). It is obtained by simply taking the dispersion of zinc blende GaAs, and folding the phonon branches back from the L to the Γ-point of the Brillouin zone [41]. This backfolding originates in the change from ABC to AB stacking configuration explained before. For the unfolded branches, the optical phonon energies in wurtzite GaAs are thus very similar to those in zinc blende GaAs. These phonons are the A_1(LO) and the E_1(TO) modes. The A_1(LO) mode is Raman allowed in $\overline{z}(y,y)z$ configuration, the E_1(TO) in $\overline{x}(z,y)x$ and $\overline{x}(y,z)y$. In addition, the backfolded $E_2{}^H$ and the $B_1{}^H$ modes are present, from which only the first one is Raman allowed.

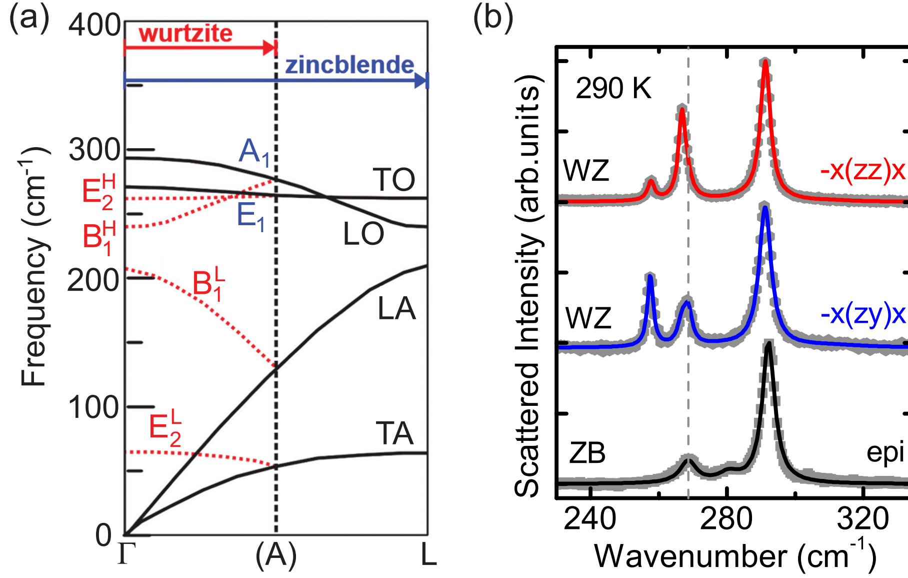

Figure 5.4.: *(a) Phonon dispersion of wurtzite GaAs obtained by folding back the branches from the L to Γ-point. Adapted from [42]. (b) Comparison of phonon lines for wurtzite and zinc blende GaAs. An additional peak appears for the wurtzite structure at* $257.5\,\mathrm{cm}^{-1}$. *Taken from [43].*

Figure 5.4 (b) displays a measurement of the optical phonons, comparing the two GaAs crystal structures. The two upper graphs both stem form a wurtzite wire, but were taken using different polarization configurations. The lowest graph shows zinc blende GaAs, illuminated along the equivalent crystal axis compared to the wires. The excitation energy was 1500 meV, which is just above the band gap at $T = 290\,\mathrm{K}$. There are three main peaks visible for the wurtzite wire. The highest one at $291.3\,\mathrm{cm}^{-1}$ is the A_1(LO) mode. According to Raman selection rules, this mode should not be allowed in either of the shown scattering geometries. The reason it still appears lies in the near resonant excitation and a consequently strong Fröhlich interaction, which is also found for bulk GaAs [23].

The dashed line in Fig. 5.4 (b) marks the position of the E_1(TO) mode. It appears in for $\overline{x}(z,y)z$ geometry at $268.6\,\mathrm{cm}^{-1}$. For $\overline{x}(z,z)x$ configuration it appears at a slightly lower energy. This behaviour can be explained by a mixing of phonon modes due to an asymmetry of atomic bonds, giving rise to a A_1(TO) mode at lower Raman shifts.

Finally and more importantly, a third mode can be found at $257.5\,\mathrm{cm}^{-1}$, that is absent in zinc blende GaAs. This peak can be identified with the ${E_2}^{H}$ mode, which is a backfolded branch in the phonon dispersion. Also the ${E_2}^{L}$ mode has already been found at a Raman shift of $64\,\mathrm{cm}^{-1}$ [44]. The appearance or absence of this modes is therefore

a way to determine the crystal structure of a GaAs wire by Raman spectroscopy.

Another service that Raman spectroscopy has offered to the research of nanowires is the observation of phonon resonances, that allows to make conclusions about the electronic band structure [45–48]. Some of these results will be presented in the next chapter, where a closer look will be taken on the electronic properties of wurtzite GaAs.

5.4. Electronic band structure of wurtzite GaAs

Just as for the phonon dispersion, there is also a big similarity between zinc blende and wurtzite GaAs in the electronic band structure: Also wurtzite GaAs is a direct band gap semiconductor, with the smallest gap at the center of the Brillouin zone. However, the energetic positions of some bands at the Γ-point relative to each other change for wurtzite GaAs.

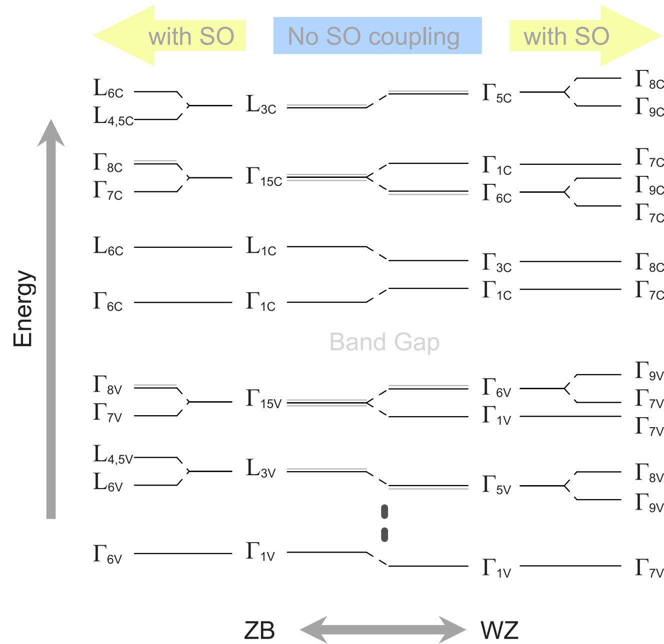

Figure 5.5.: *Important bands at the Γ-point of wurtzite GaAs without and including spin-orbit interaction. Some of the equivalent bands for the zinc blende structure are found at the L point. Taken from [32].*

An overview of how bands in zinc blende and wurtzite GaAs correspond to each other can be seen in Fig. 5.5. Here, the electronic bands at the Γ-point of wurtzite GaAs are listed, once without and once including spin-orbit coupling. As can be observed in this figure, some of these zone center bands are found at the L-point of zinc blende

GaAs. This is due to the same band folding argument that applies for the backfolding of phonon branches discussed before. An important consequence of the backfolding for the electronic band structure is the L_{6C} (L_{1C}) band from zinc blende, that becomes the Γ_{8C} (Γ_{3C}) conduction band in the wurtzite structure. This new band lies very close to the Γ_{7C} band (that corresponds to the lowest conduction band in zinc blende GaAs), rising the question which of the two is the lowest conduction band at the Γ-point for wurtzite GaAs. Theoretical works came to different conclusions, some found the Γ_{7C} to be the lowest conduction band [49], some the Γ_{8C} [32], some found it to be dependent on their used approximation [50]. On the experimental side, some groups argued to find Γ_{8C} at lower energy, based on the temperature dependence of PL [51], while others favoured the Γ_{7C} due to higher transition probabilities in order to explain the observed phonon resonances [46] or effects of strain in PL measurements [52]. The best evidence to this day are however magneto PL measurements by de Luca et al. [53]. This work exploits the fact, that the effective mass of the Γ_{8C} is larger than that of Γ_{7C} by more than one order of magnitude [50]. Extracting the exciton reduced mass out of the measured diamagnetic shift revealed that the lowest conduction band in wurtzite GaAs has Γ_{7C} symmetry. We will also find our experimental results to be consistent with this band ordering.

Next, we take a look on the valence band structure. Without spin-orbit coupling, the Γ_{15V} state of zinc blende is split by the wurtzite crystal field into the Γ_{6V} and Γ_{1V} states. The Γ_{6V} is fourfold degenerate and formed by p_x and p_y orbitals, the Γ_{1V} is double degenerate and formed of p_z states. Including spin-orbit coupling, the Γ_{1V} becomes the Γ_{7V} split off band, while the Γ_{6V} further splits into the Γ_{9V} heavy hole and the Γ_{7V} light hole band, which are energetically separated in wurtzite.

Having presented the band ordering, a closer look on the optical selection rules of wurtzite GaAs can now be taken. These are schematically drawn in Fig. 5.6 (b), following [54, 55]. Here, it can be seen which transitions are allowed for light that is either linearly polarized parallel or perpendicular to the wire axis. Critically, transitions from the heavy hole into the lowest conduction band are only possible for perpendicular polarization, while transitions from the light hole band are possible for both parallel and perpendicular polarization. A transition from heavy hole band to the next higher conduction band (Γ_{8C}) is also only possible for perpendicular polarization.

Fig. 5.6 (a) displays a collection of experimentally obtained values for the zone center bands. The low-temperature PL emission is found for wurtzite GaAs in the range of $1516 - 1517\,\mathrm{meV}$ [51, 58] to $1521 - 1524\,\mathrm{meV}$ [9, 56]. When going to room temperature,

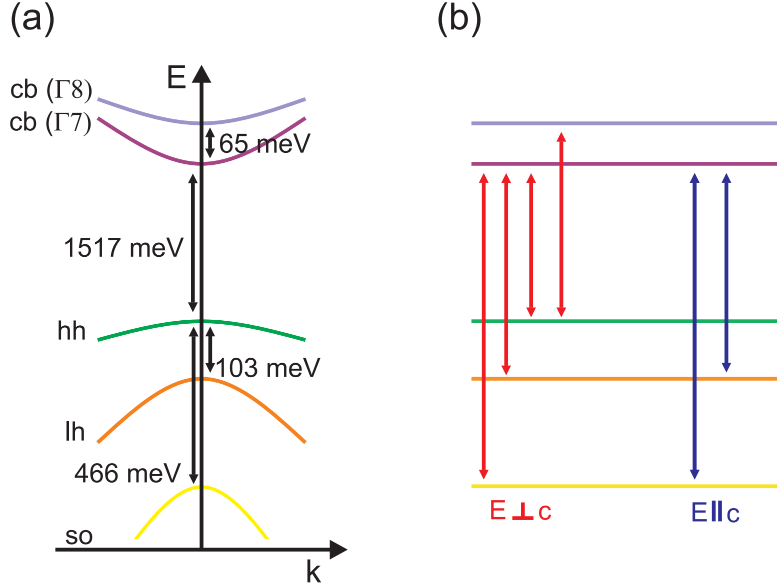

Figure 5.6.: *(a) Summary of experimental values for the most important bands at the Γ-point of wurtzite GaAs. (b) Optical selection rules for the bands shown in (a). The considered polarizations are linear, either perpendicular or parallel to the wire axis. Inspired from [46]. Value for $\Gamma_{7C} \rightarrow \Gamma_{8C}$ from [56, 57].*

it redshifts to 1444 meV [51]. The spacing between heavy and light hole bands, which is the most important difference compared to zinc blende GaAs, was quantitatively characterized using resonant Raman scattering by Ketterer et al. [46]. They exploited the already mentioned resonance of the LO phonon and its overtone due to Fröhlich interaction, and found different outgoing resonances for varying polarization configurations: For light polarized perpendicular to the wire axis, they observed a resonance pointing to a real intermediate state at 1516.5 meV, for parallel polarized light they additionally observed a real state at 1620 meV. From this, they conclude a heavy to light hole splitting of 103 meV. Similarly, the position of the split off band could be found 466 meV below the heavy hole band [47]. The Γ_{8C} conduction band was measured by PLE, and found to be approximately 65 meV above the Γ_{7C} band [56, 57].

5.5. Formation of one-dimensional subbands

The second important deviation from the band structure of bulk GaAs in our wires arises due to the radial confinement. When decreasing the wire diameter to just a few tens of nanometers, all of the bands shown in the previous section split into subbands.

This means, that the electronic wave functions perpendicular to the wire axis are now standing waves, while free motion of particles is only possible along the c-axis of the wire.

For an approximate derivation of the subband energies, the model of the cylindrical potential well [59, 60] will be considered. Later in the experimental part, we will use more exact calculations of the subband structure, that are done for a hexagonal cross section. However, the cylindrical well is already a good approximation, especially for the electron subbands. This model is characterized by the following confinement potential:

$$V(r,\theta) = \begin{cases} 0; & r < a \\ \infty; & r \geq a\,. \end{cases} \tag{5.1}$$

To derive the energy spectrum, the Schrödinger equation in polar coordinates

$$-\frac{\hbar^2}{2m}\left(\frac{\partial^2}{\partial r^2} + \frac{1}{r}\frac{\partial}{\partial r} + \frac{1}{r^2}\frac{\partial^2}{\partial \theta^2}\right)\psi(r,\theta) = E\psi(r,\theta) \tag{5.2}$$

has to be solved, which is done by separating angular and radial parts according to $\psi(r,\theta) = R(r)\,\Theta(\theta)$. The angular part leads to solutions of the form

$$\Theta_{(l)}(\theta) = \frac{1}{\sqrt{2\pi}}e^{il\theta}\,. \tag{5.3}$$

Because the solutions are required to be single valued, they should return to the same value when adding 2π. This implies that $l = 0, \pm 1, \pm 2, ...$, which means the angular momentum is quantized. After introducing the new variables $k = \sqrt{2mE/\hbar^2}$ and $j = kr$, the radial part of the Schrödinger equation becomes

$$\frac{d^2R(j)}{dj^2} + \frac{1}{j}\frac{dR(j)}{dj} + \left(1 - \frac{l^2}{j^2}\right)R(j)\ , \tag{5.4}$$

which is the Bessel equation. The solutions of the first kind $J_l(kr)$ are used, and the boundary condition from the beginning implemented, namely $J_l(ka) = 0$. This leads to subband energies of the form

$$E_{n,l} = \frac{\hbar^2 j_{n,l}^2}{2ma^2}\,, \tag{5.5}$$

where $j_{n,l}$ denotes Bessel functions vanishing at the boundary for $n = 1, 2\ldots$. The set of subbands for each n then consists of one solution for $l = 0$, but is double degenerate for $\mid l \mid > 0$. The total energy of charge carriers in a nanowire is then given by

$$E = E_{n,l} + \frac{\hbar^2 k_z^2}{2m} , \tag{5.6}$$

where the second term describes the free motion along the wire axis. Fig. 5.7 (a) shows a schematic picture of the above derived subband structure, with the quantum numbers n and l. Since the wires we use are undoped, the Fermi energy shown here is created by constant radiation of the laser, and depends on the excitation power. When only the lowest subband is occupied, we will consider the wire to be in the one-dimensional quantum limit, as all motion of charge carries then happens along the wire axis. The corresponding density of states is displayed in Figure 5.7 (b), showing the typical energy dependence for one dimensional systems:

$$n(E) = \sum_{n,l} \frac{1}{\pi\hbar} \sqrt{\frac{2m}{E - E_{n,l}}} \Theta(E - E_{n,l}) . \tag{5.7}$$

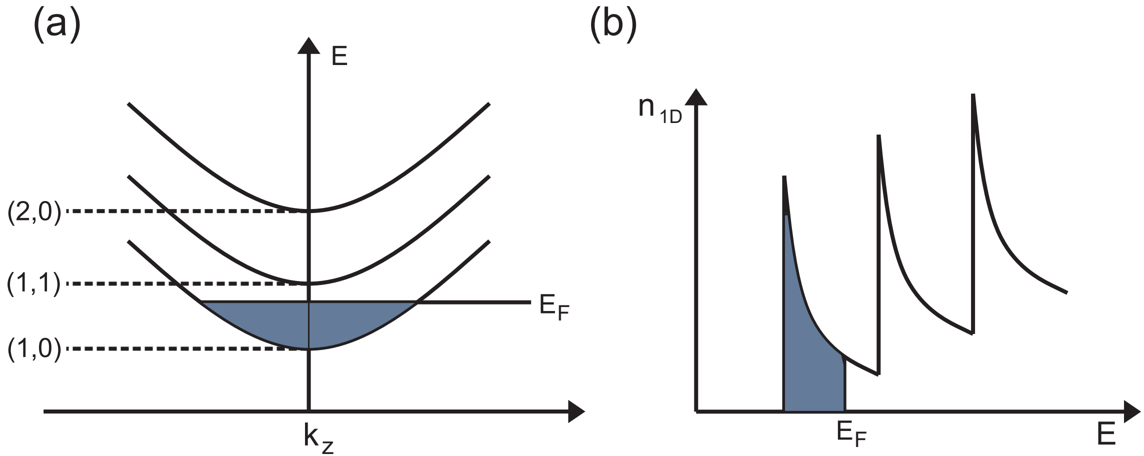

Figure 5.7.: *(a) One-dimensional subband structure for $n = 1, 2$ and $| l |= 0, 1$. In our case, the Fermi level will be induced by constant laser radiation. (b) Density of states for the subbands on the left, using the same occupation.*

As experimental evidence of quantum confinement in single wires, two main effects have mainly been observed by different groups: First, a shift of the fundamental PL to higher energies, that can be explained by equation 5.5. This formula states, that already for the lowest subband, decreasing the wire diameter quadratically increases the band energy. The resulting diameter dependent PL shift to higher energies has been observed by several groups [9, 38, 57, 61]. The second effect is the observation of hot PL, that occurs for excitation by high laser powers. When the occupation of higher subbands becomes sufficiently large, electron-hole pairs may recombine directly from

the first excited electron subband to the first excited hole subband, without relaxing to the lowest available state first. Consequently, a second PL peak at higher energies emerges [27, 62].

However, to the best of the authors knowledge, there is no direct measurement available, that displays the splitting of either the electron or hole subbands separately, and does not suffer from high excitation power induced renormalisation effects. An experimental method that was used in the past to measure subbands in GaAs-AlGaAs quantum well structures, is inelastic light scattering, the electronic version of Raman scattering. In the next section, a brief overview on how this technique was used on quantum well structures will be given.

5.6. Inelastic light scattering in low-dimensional GaAs structures

Electronic Raman scattering within two-dimensional electron systems was first measured in 1979 for modulation n-doped GaAs-AlGaAs quantum wells by Pinczuk et al. [63], and for GaAs-AlGaAs heterojunctions by Abstreiter et al. [64]. In these works, a series of broad Raman peaks (compared to phonon scattering) was found, that showed a resonant enhancement close to the $E_0 + \Delta_0$ band gap. Some years later, the observation of similar effects was realized in one-dimensional subbands by using an array of laterally patterned quantum wells, that confined the free carrier motion in one more dimension [65]. Also zero-dimensional quantum dots showed this kind of inelastic light scattering [66].

An electronic scattering mechanism that directly displays the splitting of neighbouring subbands is called a single particle excitation (SPE). In addition, two more electronic Raman features are known, which are collective excitations of free charge carriers. These are called the charge-density excitation (CDE) and the spin-density excitation (SDE) [67]. SPEs are mostly interpreted according to a two-step scattering mechanism, that is shown in Fig. 5.8 (a). Here, in the first step, an electron is excited from the valence band to a higher lying conduction subband. In the second step, an electron from the lowest conduction subband, that lies below the Fermi energy, recombines with the hole in the valence band. Hence, after the two steps an electron from below the Fermi level is excited to a higher subband state. CDEs on the other hand describe the in-phase oscillation of electrons against the positively charged background, whereas SDEs are oscillations, where electrons with opposite spin show a phase shift of π. Their appearance originates in the scattering mechanism shown in 5.8 (b). In addition to the process in (a), the

excited electron from the first two steps is annihilated in a third step, transferring its energy to another electron via Coulomb interaction. This means, that the single particle excitations are screened by the creation of collective excitations [68]. Hereby, the energy of the resulting peak in the Raman spectrum is shifted with respect to an unscreened SPE: CDEs are blueshifted compared to SPEs due to direct and exchange Coulomb interaction, while SDEs are redshifted due to attractive Coulomb exchange interaction. However, the three peaks can also be distinguished by polarization selection rules in the spectrum, since for linear polarizations SDEs appear only for crossed excitation and detection, while CDEs are only visible for the parallel configuration. SPEs on the other hand are observed for both crossed and parallel configurations.

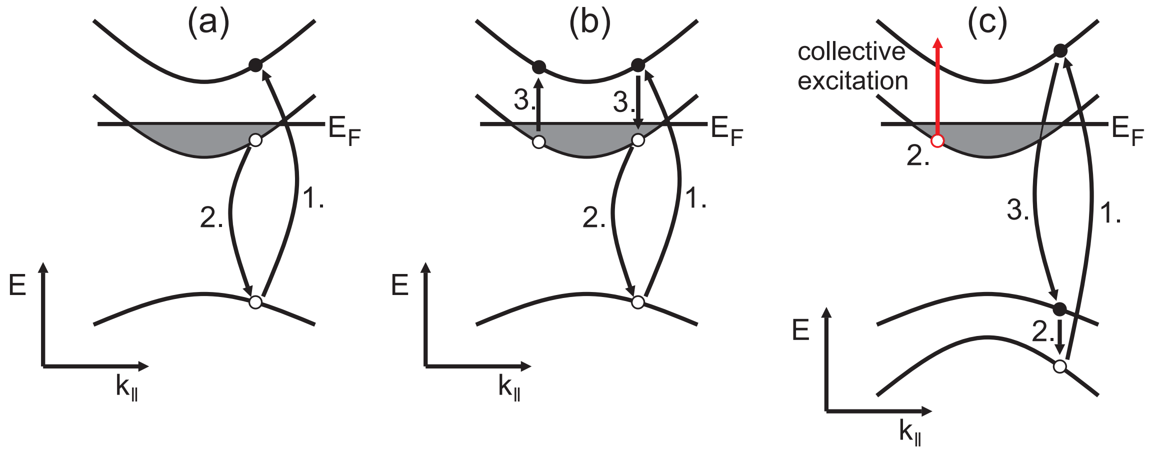

Figure 5.8.: *(a) Two step scattering mechanism responsible for single particle excitations. (b) Screening of single particle excitations by other excitations in the medium (c) Three step excitonic scattering mechanism responsible for off-resonant collective excitations. Inspired by [4].*

The scattering processes in Fig. 5.8 (a) and (b) results in a distinctive resonance behaviour of electronic Raman peaks [63]. When considering not just two, but a series of electron subbands, also a series of electronic Raman peaks that involve spacings between different subbands can be measured. Their resonance then shows two main features: On the one hand, the energetic distance between resonance maxima of different peaks matches the spectral distance of these peaks in the Raman spectrum. This is the case case, since the laser excitation in the first step has to hit higher subbands for higher excitation peaks, but the recombination in the second step still has to happen from the lowest subband. And secondly, the width of the resonance curves is comparable to the Fermi energy E_F, because for hitting a certain higher lying subband in the first step, the

excitation energy can only be varied by the size of E_F in order to still find an occupied state in the valence band for the recombination.

Different excitation energies also reveal differences between single-particle and collective excitations. It was shown that SPEs dominate the spectrum only in case of extreme resonance [69], but are screened for off-resonant excitation. For SDEs and CDEs, a more complex behaviour was found. First of all, these excitations were also observed for excitation energies far above the band gap [69]. Also, they may show much narrower resonance curves, that can be divided into ingoing and outgoing cases, and sit on top of broader curves that have a width of E_F [20]. To explain this behaviour, a three step third order scattering mechanism was proposed, that is sketched in Fig. 5.8 (c). Here, in the first step an exciton is created by laser excitation from a lower valence to a higher conduction band state. In the second step, this exciton is scattered to a lower energy state (here by changing the valence band) by Coulomb interaction, creating a collective excitation in the electron system. Finally, the exciton recombines in the third step.

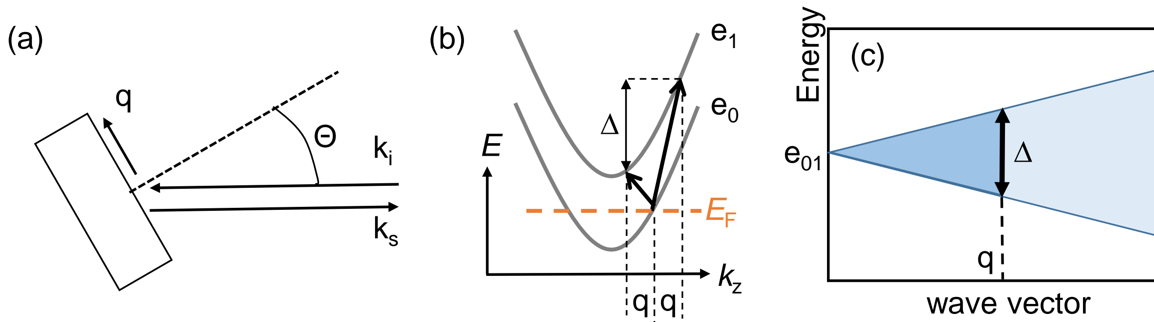

Figure 5.9.: *(a) Transfer of momentum to the medium by tilting the sample by Θ. (b) Maximal and minimal energy of a intersubband excitation depending on q (c) Upper and lower branch of the one-particle continuum, showing the minimal peak width Δ for a given q.*

Until now, it was assumed that all transitions in k-space are vertical. However, this is not necessarily the case, since it is possible to transfer different amounts of photon momentum into the sample by tilting it with an angle Θ, as depicted in Fig. 5.9 (a). If the incident and scattered laser wavelengths are similar ($\lambda_I \approx \lambda_S$), the transferred momentum q will be

$$q = \frac{4\pi}{\lambda_I} \sin\Theta \,. \tag{5.8}$$

The consequence for a intersubband SPE is shown in Fig. 5.9 (b). The two arrows

show the resulting minimal and maximal energy of the excitation, when a certain momentum q is transferred in the process. This leads to a broadening of the minimal peak width Δ, which is further illustrated in Fig. 5.9 (c). In this graph, the y-axis shows the possible energies for intersubband transitions in dependence of the momentum transfer q. For $q = 0$, there is only one possible energy, that corresponds to a vertical transition between subbands in k-space. For finite values of q, the blue shaded area marks the so called single-particle continuum, in which transitions are possible. If E_{01} is the spacing between the two lowest electron subbands, the upper branch of the single particle continuum is given by [4]

$$E_{01} + E\left(k_F + q\right) - E\left(k_F\right) = E_{01} + \frac{\hbar^2 q k_F}{m^*} + \frac{\hbar^2 q^2}{2m^*}\,, \tag{5.9}$$

and the lower branch by

$$E_{01} - \left(E\left(k_F\right) - E\left(k_F - q\right)\right) = E_{01} - \frac{\hbar^2 q k_F}{m^*} + \frac{\hbar^2 q^2}{2m^*}\,, \tag{5.10}$$

which yields a minimal peak width of

$$\Delta = \frac{2\hbar^2 q k_F}{m^*}\,. \tag{5.11}$$

Using the measurement geometry shown in 5.2 (c), we are able to excite intersubband excitations in wires lying on the substrate, as we transfer photon momentum perpendicular to wire axis. Due to the numerical aperture of the used objective, there will also be a finite momentum transferred parallel to the wire axis, leading to non-vertical intersubband transitions and an increased minimal peak width Δ.

Systematically tuning the momentum transfer parallel to the wire also enables the observation of intrasubband excitations. Hereby, the transition energy of the excitation is changed, leading to a measurable energy dispersion for all kinds of electronic excitations [69–77]. Since we are not able to do this in our setup, these transitions will not be discussed in more detail here.

6. Experimental results on GaAs nanowires

Finally, in this chapter the results of our measurements on wurtzite GaAs wires will be shown and interpreted. The first part will focus on the behaviour of the PL for different polarization and excitation energies and on PLE measurements. Next, the observation of electronic Raman peaks and their dependence on wire diameter, excitation energy and polarization will be demonstrated. In the third section, we will compare the experimental data to calculations done by Paulo de Faria Junior, present a scattering mechanism that explains the observed properties of the peaks and discuss their linewidth. In the end, the effects of different charge carrier densities due to changed excitation powers are shown and discussed.

For all the measurements, three wires with different diameters were used (with the small exception of Fig. 6.1 (c)). These wire diameters were nominally 25, 40 and 50 nm. By comparing the data to theoretical calculations, we realized that the 40 nm-wire was in fact only 31 nm and the 50 nm-wire only 41 nm in diameter. This will be explained in section 6.3.2, but for consistency, the wires will already be called 25, 31 and 41 nm-wires from the beginning. All of these wires are lying on a silicon substrate, using the measuring geometry introduced in Fig. 5.2 (c).

The short notation e_i, h_i and l_i is used for labelling the subbands of conduction, heavy- and light hole bands, respectively. The index $i = 0, 1, 2\ldots$ orders these subbands, denoting states of higher energy for increasing i.

6.1. PL characteristics of nanowires

6.1.1. Polarization and excitation energy dependence

In Fig. 6.1 (a), the PL of the 31 nm-wire is plotted for all four polarization configurations. At 1522 meV, the emission energy lies well within the range that was found by

other groups (see theory chapter). As it was also described before, the transition from heavy hole to conduction band is only allowed for light linearly polarized perpendicular to the wire axis. We therefore expect the PL to be polarized in this direction. The excitation energy was 1645 meV, enabling transitions from the light hole valence band to the conduction band, which are allowed for both parallel and perpendicular polarization with respect to the wire axis.

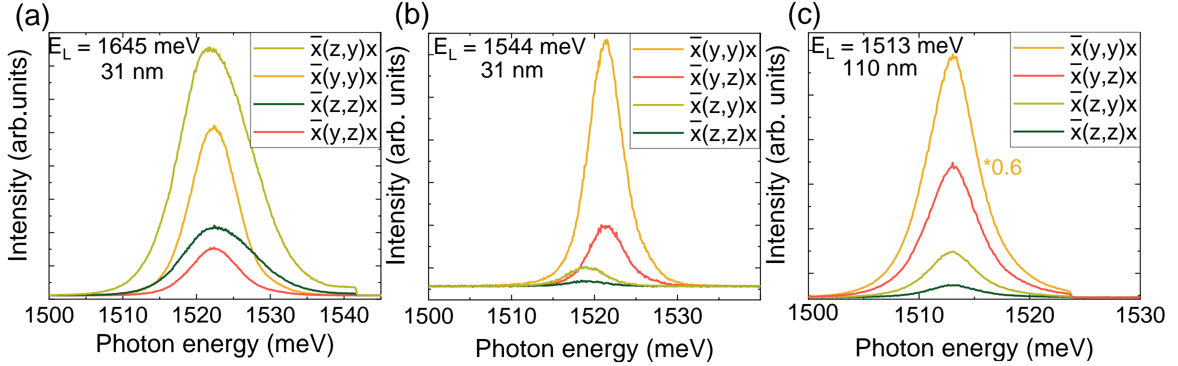

Figure 6.1.: *(a) PL of a* 31 nm-*wire for different polarization configurations, using an excitation energy above the light hole band gap. (b) Same as (a), but for excitation below the light hole band gap. (c) PL of a* 110 nm-*wire, excited below the light hole band gap.*

Clearly, the highest PL intensity can be measured for the $\bar{x}\,(z, y)\,x$ configuration in Fig. 6.1 (a), followed by the $\bar{x}\,(y, y)\,x$ configuration. So indeed, the emitted PL is polarized perpendicular to the wire as we expected. For excitation, we observe that light polarized parallel to the wire leads to higher intensities than perpendicular to the wire. According to the selection rules, both perpendicular and parallel light can induce transitions from the light hole to the conduction band. The higher intensity for parallel polarized light thus reflects a better absorption for this configuration, that most likely comes from a better overlap of wire material and light field.

This situation changes in Fig. 6.1 (b), since for an excitation energy of 1544 meV, only transitions from heavy hole to conduction band can be induced. Therefore, the best configuration for PL is the $\bar{x}\,(y, y)\,x$, where both excitation and detection are perpendicular to the wire axis. For $\bar{x}\,(z, y)\,x$ the PL is now strongly decreased compared to (a), and is found at slightly lower energy. This shift of peak position can consistently be found for all wires of comparable diameters when exciting transitions from the heavy hole band only. We suspect that the effect is hidden for excitations from the light hole band, since here the PL linewidth is much larger, as can be seen in (a). The energy shift does however vanish for larger wire diameters, which is demonstrated in Fig. 6.1 (c).

Here, heavy hole transitions are probed in a wire of 110 nm core thickness. The different polarization configurations appear in the same order with respect to PL intensity as in (b), but the energy shift between parallel and perpendicular excitation is absent. We therefore attribute this shift to strain on the wire induced by the silicon substrate. Such effects are known to shift the PL position [78]. Also, strain by the substrate would deviate stronger in different wire directions the smaller a wire diameter is, explaining the absence of the energy shift for larger diameters.

6.1.2. PLE

Having discussed the properties of the fundamental PL, the results of PLE experiments are presented in this section. Fig. 6.2 is a comparison of the PLE (red dotted line) with the PL (black solid line) for the 25 nm-wire (a) and the 31 nm-wire (b). Since the excitation energy was below the light hole band gap in every case, all measurements in Fig. 6.2 are recorded in the $\bar{x}\,(y,y)\,x$ configuration.

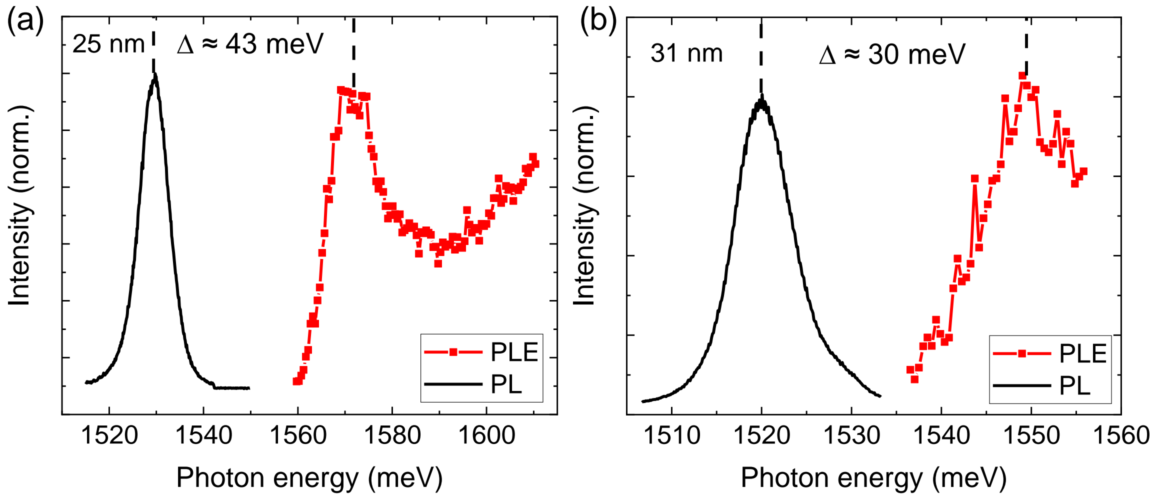

Figure 6.2.: *(a) PL (black) and PLE (red) of the* 25 nm*-wire. The first absorption peak of the PLE lies* 43 meV *higher than the fundamental PL. (b) Same as in (a) but for the* 31 nm*-wire.*

To obtain the data points on the PLE curve, the Ti:Sa laser wavelength was changed in small steps of 0.25 nm between different measurements, and the intensity of the hereby measured fundamental PL was extracted using a Gaussian fit function. However, whenever changing the laser wavelength, also the line filter for blocking side modes has to be adjusted, which becomes very time consuming in the case of PLE measurements. For

the 25 nm-wire, this could be avoided by placing a 800 nm short-pass filter before the sample. This filters out the laser side modes in the spectral region where the PL is found, meaning that we could take the line filter out of the laser path. For the 31 nm-wire, this was unfortunately not possible, as the spectral region of interest for PLE lies to close to the fundamental PL. Therefore, the line filter had to be used for the measurement shown in (b). Apart from taking a lot more time, there is another disadvantage to this method: The line filter changes its internal configuration at a wavelength of 790 nm, leading to a changing beam path for light exiting the filter already in the vicinity of 790 nm. Since a change of the beam path strongly reflects on the measured PL intensity, the curve for the 31 nm wire in (b) stops abruptly at the high energy side, before these technical issues come to play.

In addition, special care had to be taken of the applied laser power and the focus position on the sample, in order to keep the adjustment of the setup constant during a wavelength series. The laser power had to be readjusted by hand for each wavelength, as it showed that the PLE curve just follows power fluctuations of the laser otherwise. Concerning the position of the sample under the microscope objective, the main problem during a wavelength series were small drifts of the xy-table the cryostat is placed on. To exclude that an increase or decrease in the PLE just stems from a varying sample position over time, several small wavelength series were recorded. These series are overlapping in their excitation range and show, whether the PLE curve is indeed of physical origin. In Fig. 6.2, the mean values of those series are plotted.

Having solved these issues, we were able to obtain a clear peak in the PLE curve for the 25 nm-wire, that strongly resembles the expected $1/\sqrt{E}$ dependence of absorption peaks for one-dimensional systems. The PLE maximum is about 43 meV higher in energy than the fundamental PL, that stems from the heavy hole band gap ($e_0 \rightarrow h_0$). In this energy range above the heavy hole gap, we expect no other transition involving fundamental bands, as the light hole band gap lies about 103 meV above it [46]. We therefore conclude that a transition between higher subbands is responsible for this peak in PLE. Since the excitation of electron-hole pairs between higher subbands is only dipole allowed for equal subband indices, we assign the PLE to the transition from the first excited heavy hole to first excited conduction subband ($e_1 \rightarrow h_1$). This interpretation is supported by the diameter dependence of the PLE: For the 31 nm-wire, the distance between PL and PLE maxima shrinks to about 30 meV, yielding smaller subband spacings for larger wire diameter. We will also find the values obtained by PLE to be consistent with our results from Raman measurements, which are shown in the following chapter.

6.2. Observation of electronic Raman peaks

In our Raman measurements, we found two new Raman peaks that we interpret as intersubband excitations of electrons or holes. In this chapter, these peaks and their dependence on wire diameter, excitation energy and polarization configuration will be introduced. For the 31 nm-wire, also two additional new peaks were found at higher Raman shifts, which will be discussed later in section 6.4.4.

6.2.1. Diameter dependence

In Fig. 6.3, the Raman spectra containing the newly found peaks are presented for all three wires of 25, 31 and 41 nm core diameter. All spectra were recorded with a laser excitation power of 50 µW in the $\bar{x}\,(z,z)\,x$ polarization configuration. The excitation energies are 1664 meV, 1647 meV and 1640 meV for the 25 nm, 31 nm and 41 nm-wire respectively, all being slightly larger than the light hole band gap.

The raw data of the Raman measurements were normed in Fig. 6.3 for better comparability, and are represented by black dots. The solid magenta line is the sum of all fit functions, which are explained in the following.

The two most important peaks, which we named h_{01} and e_{01}, are presented by the blue and the red fit curves in Fig. 6.3, respectively. For both of those peaks, a Lorentzian line was used in Fig. 6.3. Comparing the different wires, we see immediately that they are found at lower Raman shifts for increasing diameter. For the 25 nm-wire, h_{01} and e_{01} sit at 16 meV and 28 meV, while they move to 12 meV and 20 meV for the 31 nm-wire, and to 8 meV and 12 meV for the 41 nm-wire. It is therefore apparent, that the scattering energy of these peaks is linked to the spacing of subbands, that becomes larger for smaller wire cross sections. It is also very interesting to see that for the 25 nm-wire, the sum of h_{01} and e_{01} (44 meV) almost perfectly equals the distance between fundamental PL and PLE maximum (43 meV), while it lies very close to it for the 31 nm-wire (32 meV compared to 30 meV). The separation of PL ($h_0 \rightarrow e_0$ transition) and PLE ($h_1 \rightarrow e_1$ transition) contains the energy spacings of the ground state to the first excited subband for the conduction band, as well as for the heavy hole band. Furthermore, we can see from equation 5.5 for the subband energies, that the spacing $h_0 \rightarrow h_1$ must be smaller than $e_0 \rightarrow e_1$, since the effective mass for the Γ_{7C} conduction band is smaller than for the heavy hole band [50]. Therefore, the peak h_{01} is interpreted as the subband splitting $h_0 \rightarrow h_1$, corresponding to a hole being excited from the heavy hole ground state to the first excited heavy hole subband. And consequently, the e_{01} peak is the splitting

$e_0 \rightarrow e_1$, corresponding to an electron excited from the conduction band ground state to its first excited subband. This interpretation will be further supported by the behaviour of h_{01} and e_{01} with respect to excitation energy, as well as comparing the experimental data to realistic $k \cdot p$-theory band structure calculations.

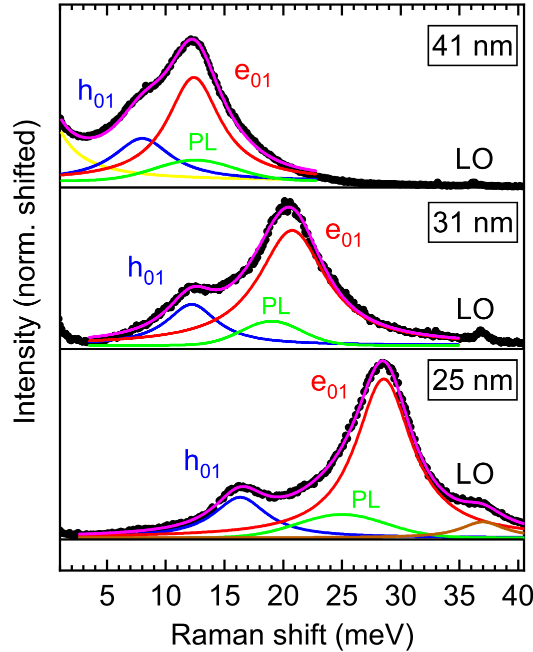

Figure 6.3.: *Raman spectrum of all wire diameters investigated. The raw data are represented by black dots. The solid lines are the fit curves for the* e_{01} *peak (red), the* h_{01} *peak (blue), light hole luminescence (green), the LO phonon (brown) and Rayleigh scattered light (yellow). The magenta line is the sum of all other fit functions.*

In contrast to the h_{01} and e_{01} peaks, the LO phonon that is also visible in the spectrum due to Fröhlich interaction, stays at a constant Raman shift for all wire diameters. For the 25 nm-wire, it was also included into the fitting procedure (brown solid curve). It appears to be broader in this case than for the other wires, which could possibly be explained by Landau damping. Since the phonon energy lies close to the e_{01} spacing for this diameter, the oscillation could decay into uncorrelated electron hole pairs. Such a mechanism was observed in a very similar fashion in graphene [79]. Other optical phonons are very weak in intensity (it was observed that they gain in intensity for thicker wires), and partially overlap with the strong e_{01} peak, which is why they are not

further discussed here.

In addition, a green solid curve is fitted into the spectra of Fig. 6.3, that has a Gaussian shape in contrast to all other fit functions. We interpret this feature as a hot PL from the light hole to the conduction band, $l_0 \rightarrow e_0$. As it is not possible to differentiate between Raman and PL features in this spectra, the excitation-energy dependence will be introduced in the next section.

6.2.2. Resonance behaviour

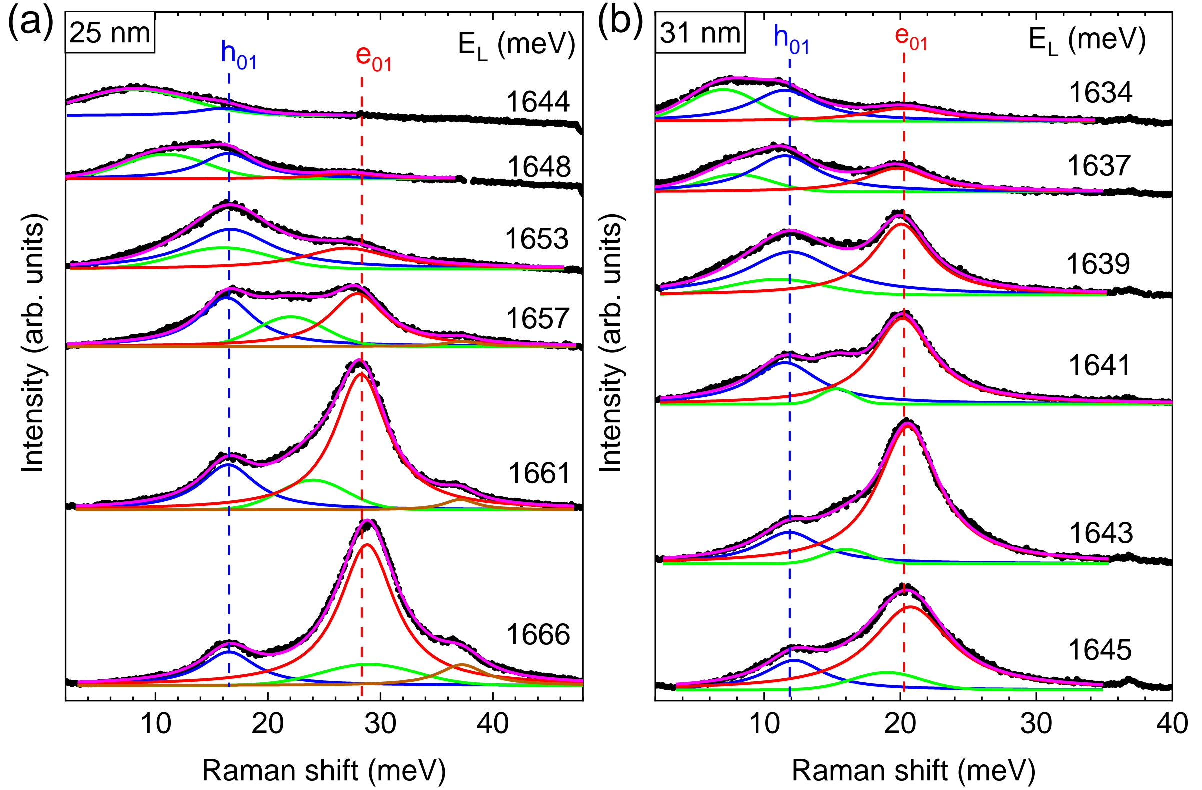

Figure 6.4.: *Raman spectra for different excitation energies for the* 25 nm-*wire (a), and the* 31 nm-*wire (b). The exact laser energy for each spectrum is given by* E_L (meV)*. The* h_{01} *(blue) and* e_{01} *(red) peaks stay at a constant Raman shift for different excitation energies, however their intensity varies strongly. The light hole luminescence (green) stays at an constant absolute energy, and therefore appears at different energies in the Raman spectrum when changing* E_L*.*

Fig. 6.4 displays the excitation-energy dependence of the Raman spectra for the 25 nm-wire (a) and the 31 nm-wire (b). This time, the measurement data represented by the black dots are not normed in order to demonstrate the resonance behaviour of

the h_{01} (blue) and e_{01} peak (red). As before, the green curve is the light hole hole PL and the magenta line the sum of all fit functions. The energy of the laser is given by E_L for each graph.

In this plot, we can see that the light hole PL does not stay at constant Raman shifts for different excitation energies. This becomes especially clear for laser energies where it sits between h_{01} and e_{01}, or appears at the low energy side of h_{01}. The simple reason for this behaviour is, that it has a constant absolute energy, as it is expected for any kind of luminescence. This energy is 1635 meV for the 25 nm-wire and 1626 meV for the 31 nm-wire. As we find the fundamental PL at 1529 meV for 25 nm and at 1522 meV for 31 nm, the values for the light hole PL are just slightly larger than the expected ones, since the $l_0 \rightarrow h_0$ distance was found to be 103 meV [46].

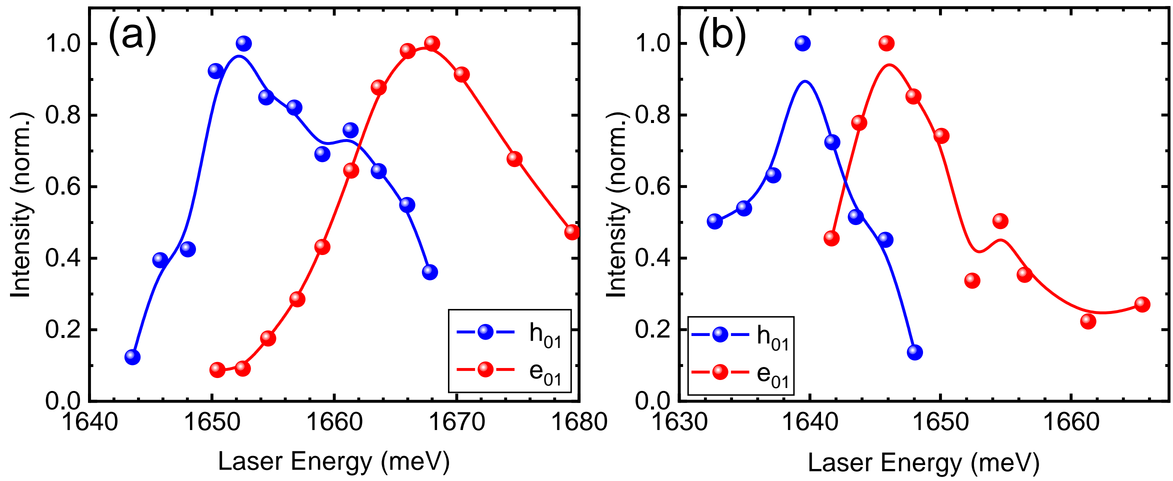

Figure 6.5.: *Resonance curves for the h_{01} and e_{01} peaks for the 25 nm-wire (a) and 31 nm-wire (b). The data points are obtained by using the area from the Lorentzian fitting curves shown above. Both curves are normed for better comparability of resonance maxima.*

The h_{01} and e_{01} peaks on the other hand always keep the same energetic distance to the laser for any excitation energy, proving that they are in fact Raman effects. The interesting observation for those two peaks is the strongly varying intensity for different laser energies. Since for presentation purposes, only a selection of excitation energies is shown in Fig. 6.4, the complete resonance curves of h_{01} and e_{01} are plotted in Fig. 6.5 for 25 nm (a) and 31 nm (b). The data points in these resonance curves are the areas from the Lorentzian fitting curves used in Fig. 6.4. Both peaks only appear in a small region of excitation energies, the resonance curves therefore start from the point where

the count rate was sufficient to obtain reasonable fit functions. All resonance curves were normed for a better comparability of the different resonance positions.

There are two interesting observations from the resonance behaviour. First of all, the energetic difference between the resonance curve maxima of h_{01} and e_{01} equals the spectral distance of these peaks in the Raman spectrum. For the 25 nm-wire, the difference of resonance maxima is about 2 meV larger than the spectral distance, whereas it is 1.5 meV smaller in case of the 31 nm-wire. When looking at this deviation, it has to be considered that the exact intensity of the Raman peaks, and therefore the resonance curves, are dependent on the stability of the setup during a measurement. Since the exposure times for getting reasonable spectra had to be around 45 minutes, the agreement of spectral distance to the spacing in resonance energy can be considered to be quite good. The second interesting observation is, that the maximum intensity of both peaks is reached when they coincide with the light hole luminescence in the Raman spectrum. Therefore, in case of extreme resonance, the outgoing photon has the energy of the light hole band gap $l_0 \rightarrow e_0$. From these two findings we can learn the following: The scattering mechanism for both peaks involves the same intermediate state, namely the light hole to conduction band gap. If the excitation energy is chosen to be larger than this gap by the spectral energy of h_{01}, this peak is resonantly enhanced, the same holds true for e_{01}. Thus, the resonances observed are of the outgoing type, using the light hole band gap as the second intermediate state. This information is very useful for finding the exact scattering mechanism, which will be done in section 6.3.1, after the polarization selection rules of the Raman peaks have been considered in the following section.

6.2.3. Polarization dependence

In Fig. 6.6, the Raman spectrum of the 25 nm-wire is shown for all four polarization configurations. The excitation energy lies close to the e_{01} resonance. Comparing the different polarizations, it is obvious that the Raman signal is only well pronounced in case of the $\bar{x}\,(z,z)\,x$ configuration. Therefore, all of the Raman spectra containing the h_{01} and e_{01} peaks are recorded using this configuration for all further experiments. In the lab, we obtained this configuration by looking at the PL first; when the excitation energy is larger than the light hole band gap, we know that excitation parallel and detection perpendicular to the wire gives the highest PL intensity (see Fig. 6.1 (b)). Therefore, after maximizing the PL by using the half wave plates in front and after the sample, we simply turned the detection configuration by 90°, in order to get $\bar{x}\,(z,z)\,x$. It

was verified that this procedure leads to the expected configuration, by placing a linear polarizer directly in front of the sample and comparing the linear polarization directions with the orientation of a wire on the substrate, which is known from optical microscope images like in Fig. 5.2 (b). We therefore know that the configurations in the caption of Fig. 6.6 are correct.

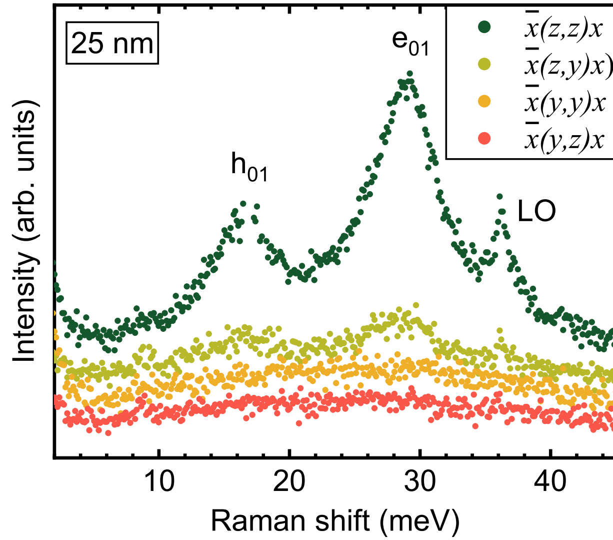

Figure 6.6.: *Comparison of all polarization configurations for the* 25 nm*-wire. The electronic Raman peaks are best pronounced for* $\bar{x}\,(z,z)\,x$ *configuration. The ordering of the configurations with respect to Raman intensity is the same for all measured wire diameters.*

With respect to excitation, the dependence of the Raman peak intensity on the polarization is the same as for the PL: Since the laser energy is larger than the light hole gap, polarization parallel to the wire axis is favoured. In contrast, the Raman intensity is maximized if the detection is also parallel to the wire; in the case of $\bar{x}\,(z,y)\,x$ configuration, only small traces of Raman peaks are visible. For both configurations using excitation perpendicular to the wire, all Raman peaks vanish completely. If we are exciting electron-hole pairs from the light hole to the conduction band, we would not expect this, since light hole transitions are allowed for both parallel and perpendicular polarisations. However, this dependency still tells us that the assumption of having light hole transitions is correct: The possibility, that the excitation actually starts from the heavy hole band and goes to a higher conduction band state is now ruled out, since

these excitations would only be allowed for polarizations perpendicular to the wire axis. Using this information, we can construct a scattering mechanism in the next step, that gives rise to all properties of the h_{01} and e_{01} peaks presented so far.

6.3. Interpretation as intersubband excitations

In this chapter, the interpretation of all experimental data shown so far as intersubband excitations of electrons or holes will be discussed. At first, the scattering mechanism for explaining the h_{01} and e_{01} peaks will be presented, which will further support the conclusions about the observed resonance behaviour. In the following, the experimentally measured values for the subband splittings will be compared to theoretical band structure calculations, and all data (including PL and PLE) to the calculated absorption. Finally, the linewidth of the e_{01} peak will be discussed in more detail.

6.3.1. Scattering mechanism

The h_{01} and e_{01} peaks were interpreted before as the spacings between the lowest and first excited subband in heavy hole or conduction band, respectively. This already implies, that we treat them as SPEs, which were introduced in section 5.6. We will discuss this assumption in more detail, when looking at the power dependence of the two peaks. In the introduction about SPEs, their scattering mechanism was described as a two step process (see Fig. 5.8 (a)), where a SPE in the conduction band is created by exciting an electron to the upper subband, and a recombination of another electron from the ground state back to the valence band at the same time. However, this scattering mechanism is not applicable for our situation. Since we interpret the h_{01} peak as the splitting of the two lowest heavy hole subbands, an equivalent two step scattering mechanism for excitations in the valence band would have to start directly from the heavy hole band. In the previous section, it was however stated that this possibility can be excluded due to the measured polarization selection rules. Therefore, we will interpret our results according to a third order three step scattering mechanism, that is sketched for our two peaks in Fig. 6.7. Such three step mechanisms were first discovered for electronic excitations by Danan et al. [20], but also found very recently in one-dimensional carbon nanotubes [80].

For the h_{01} peak, we propose the mechanism in Fig. 6.7 (a), that works as follows: In the first step, the incident laser photon excites an electron from the l_0 band to a virtual

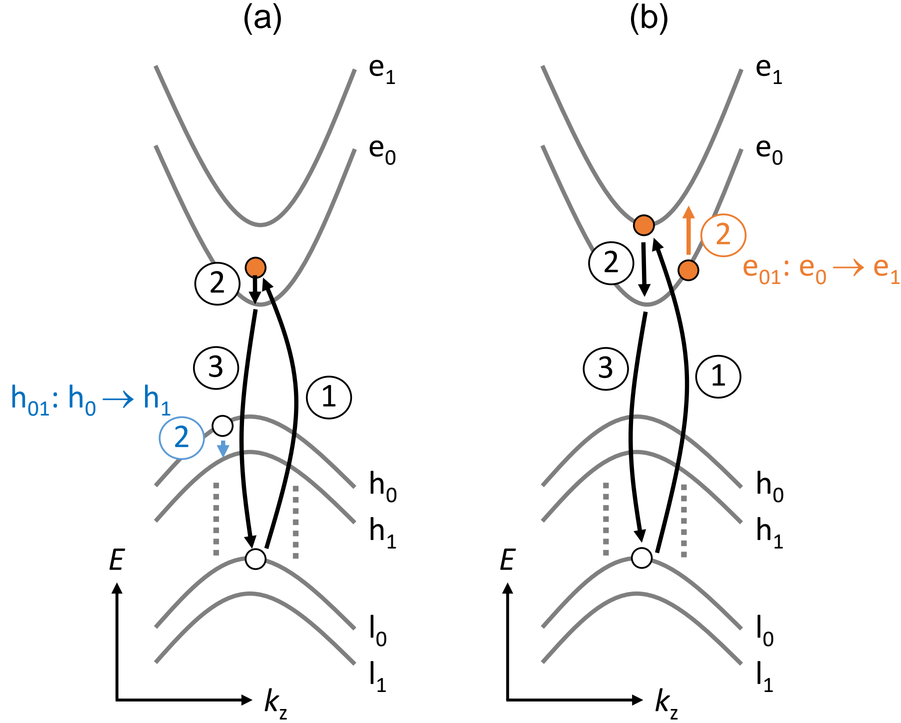

Figure 6.7.: *Scattering mechanism for the h_{01} peak (a) and e_{01} peak (b). Both processes are third order three step scattering mechanisms, which are enhanced by an outgoing resonance. The Fermi level that is needed to provide free carriers in the valence band (for h_{01}), or conduction band (for e_{01}), is provided by continuous laser radiation.*

state between the two lowest conduction subbands. In the second step, this electron is scattered into the e_0 band by Coulomb interaction with a hole in the h_0 band, which is itself scattered to the h_1 band by energy exchange. Finally, the electron recombines back from the e_0 to the l_0 band in the third step. In total, a hole was therefore excited from the h_0 to the h_1 state, and the emitted photon in the third step is lower in energy than the laser excitation by this subband splitting.

For the e_{01} peak, the process works very similar (see Fig. 6.7 (b)). Here, the electron is excited to a virtual state very close to the e_1 band in the first step. Then, it is scattered down to the e_0 band by exchanging energy with an electron, that sits in the e_0 band and is lifted to the e_1 band. In the third step, the first electron recombines back from the e_0 to l_0 state, leaving the created e_{01} excitation behind.

The resonance behaviour of this third order mechanism is described by a very similar formula as equation 3.9. The main difference is however, that the matrix element in the middle of the numerator, that describes the scattering between the two intermediate

states by the created excitation, now contains the Coulomb interaction Hamiltonian instead of the one for electron-phonon coupling. In other words, for this scattering process we can use the terminology of incoming and outgoing resonances as introduced in chapter 3.2. It was already argued, that the observed resonances are of the outgoing type, since in the case of their highest intensity h_{01} and e_{01} overlap with the $l_0 \rightarrow e_0$ PL in the Raman spectrum. We can directly see this from the scattering mechanism in Fig. 6.7: The second intermediate state of this mechanism will be the $l_0 \rightarrow e_0$ gap, if the laser energy is chosen to be larger than this gap by the energy of h_{01} or e_{01}. In the case of the e_{01} peak, it would also be possible that the first intermediate state is real, since it comes together with the e_1 band in case of resonant excitation. However, the $l_0 \rightarrow e_1$ excitation would have a significantly lower transition probability than the recombination via $l_0 \rightarrow e_0$, since only the latter of the two is dipole allowed. We therefore believe, that the first intermediate state is still virtual for the e_{01} peak, even in the case of resonant excitation. Consequently, for both peaks the resonances are of the outgoing type, using the dipole allowed transition $l_0 \rightarrow e_0$ as the second intermediate state.

For these scattering mechanisms, it is implied that there are free holes in the h_0 band or free electrons in the e_0 band, of which the laser excited electrons can scatter. It was stated before that the wires we use are undoped, which means that without any kind of optical excitations, the Fermi level should sit within the fundamental band gap. This is a stark contrast to all observations of electronic Raman scattering in GaAs quantum-well structures introduced in section 5.6: Here, all samples are modulation n-doped, which means that (depending on the exact sample preparation) at least one conduction subband is always occupied by free electrons. In our case, free carriers are present due to the constant laser radiation during the measurement. Depending on the laser power, we create a certain amount of free electrons in the e_0 band, and also free holes in the h_0 band, due to fast relaxation processes from the l_0 band on a picosecond time scale [81]. We will verify this hypothesis by performing excitation-power dependent measurements later in section 6.4.1.

6.3.2. Comparison to band structure calculations

After introducing our interpretation for the h_{01} and e_{01} peaks, we will take a look on whether the extracted values for the subband spacings agree with theoretical predictions. To do this, we collaborated with Paulo de Faria Junior from the group of Prof. Jaroslav Fabian, who provided calculations of the one-dimensional band structure, which are shown in Fig. 6.8.

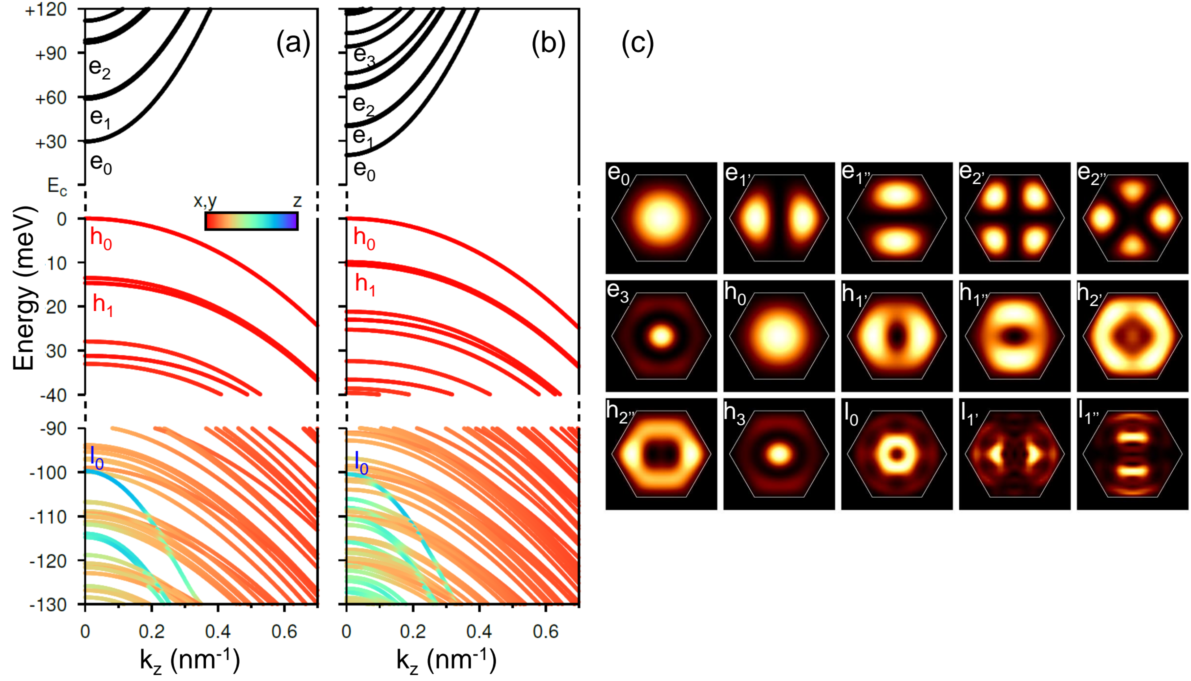

Figure 6.8.: *Realistic* $\boldsymbol{k} \cdot \boldsymbol{p}$ *band structure calculations for the* 25 nm-*wire (a) and the* 31 nm-*wire (b). The value of the bulk band gap* E_C *is omitted in this plots. The colours of the valence subbands are linked to the polarization of the transition dipole to the conduction band. (c) Probability densities at* $k_Z = 0$ *for the most important bands in the* 25 nm-*wire. For the excited subbands, there are two configurations, which show a small splitting in energy.*

The calculations shown are obtained by the $\mathbf{k} \cdot \mathbf{p}$ method, using the envelope function approximation, which incorporates the hexagonal symmetry of the wire cross section. Since the GaAs core is protected by a shell and cap layer as described earlier, the potential height is not infinite, and was averaged by a effective potential of 5 eV. The effective masses for the conduction, heavy and light hole bands were taken from [50]. A short summary of how these calculations were performed, and the sources of the used parameters, can be found in [25].

In Figure 6.8 (a), the conduction, heavy and light hole subbands (as indicated by the usual labels) are shown at the Γ point of the 25 nm-wire. The bulk band gap of wurtzite GaAs E_c is set to zero in this plots. Therefore, the separation of 30 meV between h_0 and e_0 bands is induced by confinement and leads to the diameter dependent blueshift of fundamental PL, as mentioned in section 5.5. For the splittings of electron and heavy hole subbands, we can see a good agreement with the values from our Raman

measurements. This also holds true fore the calculation of the 31 nm-wire in Fig. 6.8 (b), however only after a correction of the wire diameter. As mentioned right in the beginning of the experimental chapter, the wire we used had a nominal diameter of 40 nm. For this value, the values of h_{01} and e_{01} from our measurements were found to be too large compared to the calculations. This issue was solved by correcting the wire diameter to 31 nm, just as the nominally 50 nm-thick wire turned out to actually have a diameter of 41 nm. In these cases, the good agreement between measurement and calculations lies in the fact, that we can always find a wire diameter for which both the experimental values of h_{01} and e_{01} agree to the calculation simultaneously.

The colour code of the valence subbands reflects the polarization of the transition dipole to the conduction band. Here, red means that only transitions for light polarized perpendicular the wire axis are possible, whereas blue stands for a polarization parallel to the wire. It follows, that for transitions from the lowest light hole band l_0, the polarization has a stronger z component for the 25 nm-wire than for the 31 nm-wire. For the heavy hole bands on the other hand, in both cases transitions from h_0 and h_1 bands are only possible with perpendicular polarization. This supports our interpretation, that the first step of the scattering mechanism starts from the light hole band, as we only observe the Raman peaks in the $\bar{x}\,(z, z)\,x$ configuration. Since the incident polarization is parallel to the wire here, it can not induce a heavy hole transition, the same holds true for the recombination.

In Fig. 6.8 (c), the probability densities for the 25 nm-wire are calculated for the most important bands at $k_z = 0$. The cross section of the wires is indicated by the white hexagonal areas. It is apparent, that for the lowest conduction and heavy hole subbands e_0 and h_0, the density has cylindrical symmetry. For the first excited subbands on the other hand, the slightly asymmetric hexagonal cross section leads to two separate states, labelled $h_{1'}$ and $h_{1''}$ ($e_{1'}$ and $e_{1''}$) for the heavy hole (conduction) band. These two states experience a small shift in energy, which is however smaller than 1 meV in most cases. The strongest energy splitting can be seen found for the $h_{1'}$ and $h_{1''}$ states in Fig. 6.8 (a). However, even here the splitting is smaller than the observed linewidth of the Raman peaks in the experiment, which are typically larger than 5 meV, and therefore does not influence our interpretation. The linewidth we get from our experiment will be discussed in more detail in the following section.

6.3.3. Discussion of linewidth

So far, it was assumed that all optical transitions are vertical in k-space. This is however not strictly the case. In section 5.6 it was explained, that transferring photon momentum parallel to the sample plane leads to non-vertical transitions in k-space, and consequently to an one-particle continuum for intersubband excitations. It was already mentioned, that we can not deterministically tilt the sample in the cryostat to achieve this momentum transfer in our measurement. However, due to the large numerical aperture (0.8) of the used microscope objective, we will still transfer a finite momentum of maximum value

$$q = \frac{4\pi}{\lambda_I} 0.8 \tag{6.1}$$

parallel to the wire axis, as it was already indicated in Fig. 5.2. Hence, the minimal peak width of the electronic Raman peaks is defined by the one-particle continuum for the given value of transferred photon momentum.

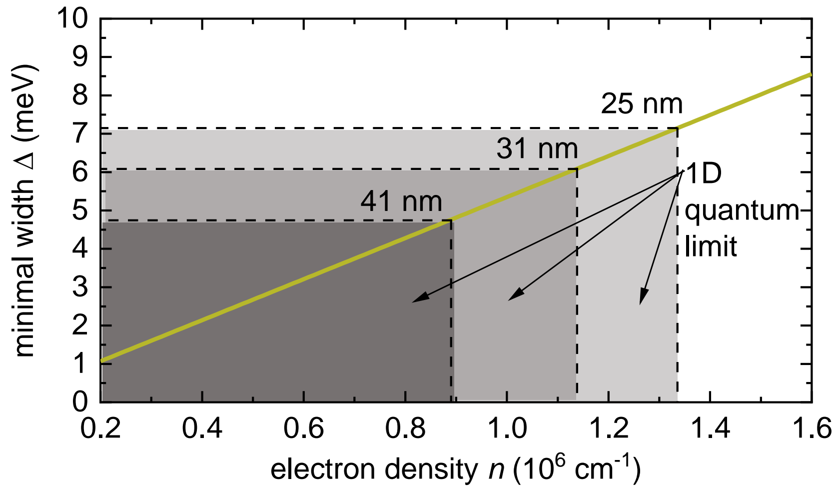

Figure 6.9.: *Linewidth of the e_{01} excitation in dependence of the charge-carrier density n. The range for which the different wires are in the one-dimensional quantum limit is indicated by grey boxes.*

As the minimal peak width is not only dependent on the transferred momentum q but also on the Fermi wave vector k_F, which is linked to the charge-carrier density by $k_F = n\frac{\pi}{2}$ in one-dimensional systems, it gets broader with increasing density n. Since the momentum transfer stays constant in all the measurements, analysing the linewidth of the peaks therefore allows us to draw conclusions about the charger-carrier density in

our samples. This is illustrated in Fig. 6.9. Here, the dependence of the linewidth on the carrier density is plotted by a linear function using the formula

$$\Delta = \frac{\pi \hbar^2 q}{m^*} n \,, \tag{6.2}$$

where q is given by equation 6.1 and the effective mass is $m^* = 0.06 m_e$ [50]. For us, it is especially interesting to see whether the wires are in the one-dimensional quantum limit during the measurement, and thus if only one or more subbands are occupied by electrons due to laser excitation. As the effective mass for holes in the heavy hole band is significantly larger than for electrons in the conduction band, we know that the wires leave the one-dimensional quantum limit, when the first excited conduction subband is occupied by electrons. Since the electron Fermi energy for this case is just the energy of the e_{01} peak, we can calculate the density for which the one-dimensional quantum limit is lost, as it is shown in Fig. 6.9 by the grey boxes.

In Fig. 6.3, we can read out linewidths for the e_{01} excitation of 5.8 meV, 7.0 meV and 5.5 meV for the 25 nm, 31 nm and 41 nm-wire, respectively. Comparing these values to Fig. 6.9, we can see that the 25 nm-wire is well within the one-dimensional quantum limit range, with a corresponding charge-carrier density of $1.1 \cdot 10^6\,\mathrm{cm}^{-1}$. However, the values in Fig. 6.9 correspond to the intrinsic case, without any sort of inhomogeneous broadening, giving the minimal peak width for a certain momentum transfer and charge-carrier density. Since we expect for example slight changes in the wire diameter along the wire length, which would also broaden the Raman peaks, the charge-carrier density obtained by comparing the experimental width to Fig. 6.9 can be seen as the upper limit, with the actual density being smaller. Consequently, also the 31 nm and 41 nm-wires, where the experimental width (7.0 meV and 5.5 meV, respectively) is just above the range of the one-dimensional quantum limit in Fig. 6.9, could actually still lie within it. It will be shown later by excitation-power dependent measurements, that this is indeed the case.

6.4. Effects of excitation power

Until now, all experimental data shown were taken with a laser excitation power of 50 µW. In this final part of the experimental chapter, the effects of changing power and therefore varying charge-carrier density will be presented and discussed.

6.4.1. Determination of charge-carrier density

In Fig. 6.10, all relevant effects of different laser powers on the Raman and PL spectra are summarized for the 31 nm-wire (a-c), and the 25 nm-wire (d-f). In (a) and (d), the Raman spectra for the two wires are shown for a series of different excitation powers. Since the measurement setup had been slightly changed in comparison to when the measurements in Fig. 6.3 and 6.4 were performed, the powers are now given relative to a power P_0, which corresponds to 50 µW in the previous measurements. This was assigned by comparing the intensity ratio of the h_{01} and e_{01} peaks. In the plots shown here, the Raman spectra are normed for a better comparability of those intensity ratios. The laser excitation energy is chosen to be slightly above the e_{01} resonance position in both cases. This means that it is possible to populate the lowest and first excited conduction subband by electrons. Due to Pauli blocking, the charge-carrier density will saturate at some point and not increase to arbitrarily high values. The first excited heavy hole subband on the other hand can not be populated by holes in this measurement, as the effective mass for this band is much higher, as already discussed in the previous section. In (b) and (e), the emergence of hot PL via the $e_1 \rightarrow h_1$ transition is displayed, which occurs when the first excited conduction subband is occupied. In contrast to the Raman measurements, the PL data are not normed. In (c) and (f), the intensity of this hot PL peak is shown by the blue dots with respect to the used laser power. A linear fit determines the power for which the occupation of the first excited electron subband starts.

The onset point of the hot PL can be used to calculate the charge-carrier density at the excitation power P_0. For the 31 nm-wire, we find the e_{01} excitation at 21 meV in the Raman spectrum for $0.5\,P_0$, before it redshifts with increasing power. Using this as the electron Fermi energy gives an electron density of $\approx 1.2 \cdot 10^6\,\mathrm{cm}^{-1}$ for the moment, when the first excited electron subband starts getting occupied. As this situation corresponds to a laser power of $1.2\,P_0$, as can be seen from the fit in Fig. 6.10 (c), we get a charge-carrier density of $\approx 1.0 \cdot 10^6\,\mathrm{cm}^{-1}$ for the power P_0. Comparing this density to Fig. 6.9, we can see that also the 31 nm-wire was in the one-dimensional quantum limit in all previous measurements. Consequently, approximately 25 % of the 7 meV linewidth are due to inhomogeneous broadening.

In a similar way, we find that the 25 nm-wire has a charge carrier density of $\approx 0.24 \cdot 10^6\,\mathrm{cm}^{-1}$ for an excitation power of P_0. It follows that 77 % of the measured linewidth of 5.8 meV are due to inhomogeneous broadening. It is not surprising that this is more than for the 31 nm-wire, as broadening due to wire width fluctuations becomes quantitatively

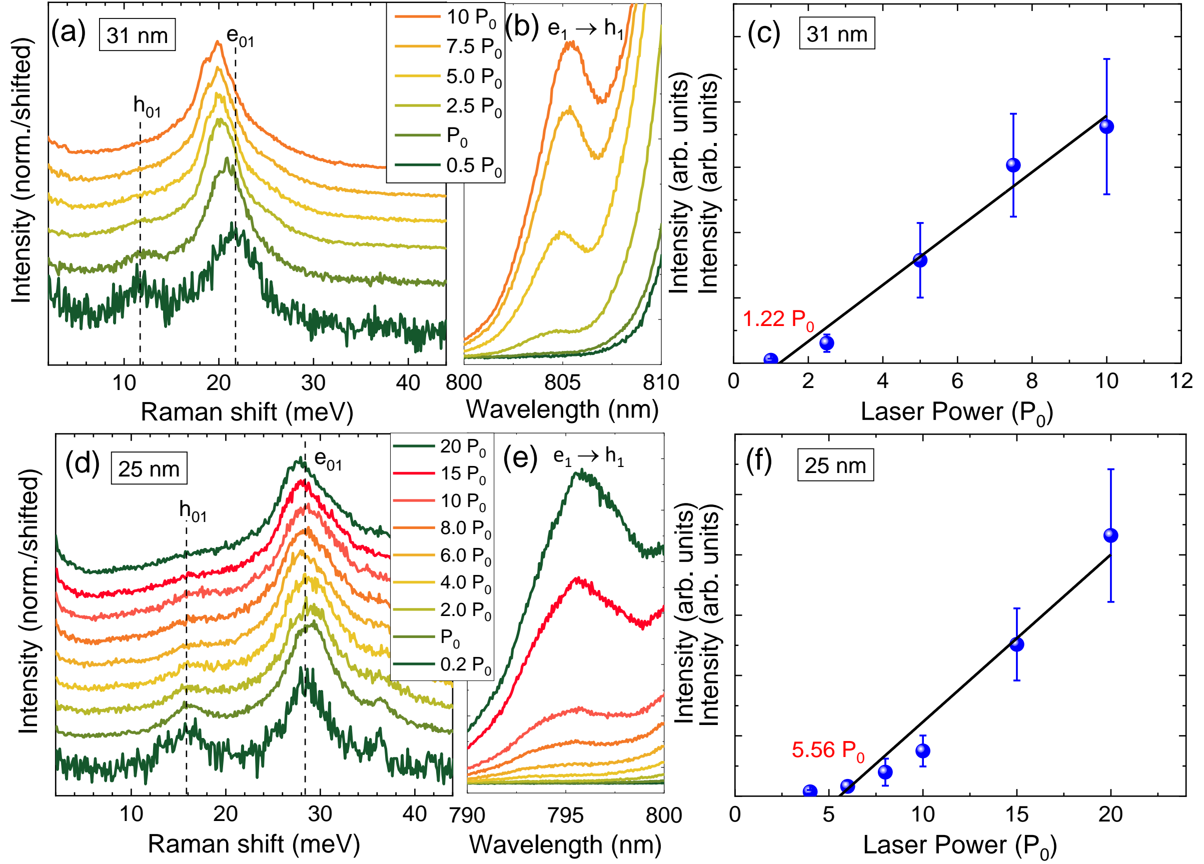

Figure 6.10.: *(a) Normed Raman spectra for the* 31 nm*-wire for different laser powers relative to* P_0*, which corresponds to* 50 µW *in the previous measurements. (b) Emergence of hot PL for increasing excitation power via the* $e_1 \rightarrow h_1$ *transition. (c) Intensity of the hot PL in (b) in dependence of the used power. The linear fit marks the power for which the first excited conduction subband is occupied. (d-f) Same as (a-c), but for the* 25 nm*-wire.*

more important for thinner wires, due to the $1/d^2$-dependence of quantization energies.

The electron density for the 25 nm-wire at the power P_0 is also very close to the Mott density in GaAs quantum wires, which was calculated to be $n_{Mott} = 3 \cdot 10^5\,\mathrm{cm}^{-1}$ [82]. Therefore, it is possible that excitons still play a role in the scattering process of the Raman peaks, for example as intermediate states. This influence of excitonic effects will be stronger, the thinner the wire is. First of all, because a constant excitation power creates a lower charge carrier density for thinner wires, which is a result of the smaller active airer. And second, since the exciton binding energies increase with decreasing wire diameters, due to reduced screening effects of interacting electrons and holes. This

was theoretically predicted for nanowires [83, 84] and shown experimentally [85, 86], with exciton binding energies being up to seven times larger than in bulk GaAs, depending on diameter and shape of the wire. However, having a mixture of excitons and free electrons in the 25 nm-wire will most probably not influence any of the scattering energies, since the authors of [82] also find a cancellation of the redshift due to band gap renormalisation and the blueshift due to vanishing of excitonic states, as it was described in the introduction section 2.2.

6.4.2. Power dependence of Raman peaks

After deriving the charge-carrier density from the hot PL characteristics, the consequences of the excitation power on the h_{01} and e_{01} peaks will be discussed in this section. It was already visible in Fig. 6.10 (a) and (d), that the h_{01} peak vanishes for increasing illumination power. We can understand this as a consequence of the varying electron Fermi level in the conduction band. When increasing the laser power, it is shifted upwards until eventually the first excited electron subband is occupied, and the hot PL sets in. As the scattering of the h_{01} peak is mediated by exciting an electron to a virtual state that lies by the energy of h_{01} above the conduction band edge, this process is suppressed by Pauli blocking, if the electron Fermi level in the conduction band is higher than the h_{01} scattering energy. This is consistent with the appearance of the hot PL: It is observed that the h_{01} is only pronounced for excitation powers, where the hot PL is not yet visible. Increasing the power, the h_{01} gets significantly weaker, before the hot PL sets in by shifting the electron Fermi level even higher to the first excited subband. Consequently, we can use this as a further proof that the wires are in the one-dimensional quantum limit for the power P_0; as long as the h_{01} peak is visible, this has to be the case, because otherwise the scattering mechanism is blocked. Furthermore, the assumption that was made when introducing the scattering mechanism, that stated we have free charge carriers in the lowest subbands due to constant laser radiation, is clearly justified by this power dependency.

Apart from the h_{01} peak vanishing, ramping up the laser power also results in a redshift of the e_{01} excitation. This effect is observed for both wires, but is stronger pronounced for the 31 nm-wire, where a higher charge-carrier density is created. Therefore, the question arises whether this can be interpreted as an plasmonic shift, or if our assumption that the Raman peaks are single-particle excitations is correct. The CDE plasmon can be ruled out, as it is expected to shift to higher energies with increasing carrier densities due to direct Coulomb repulsion. The SDE plasmon on the other hand does redshift

with growing carrier density, due to attractive Coulomb exchange interaction. However, this excitation is only observed in crossed configuration of incident and emitted linear polarizations, which is in contradiction to the selection rules we observe in Fig. 6.6, where we get the strongest signal for the $\bar{x}\,(z,z)\,x$ case. Furthermore, for different polarization configurations we see a drastic change in intensity of the Raman peaks, but no change in scattering energy that could be interpreted as a depolarization shift between CDE and SDE excitations. We therefore conclude, that the power dependent shift of the Raman peaks is not of plasmonic origin, and the Raman peaks are of single-particle character. This is further supported by the absence of a plasmon-phonon coupling in our measurements. This usually happens in polar GaAs, due to coupling of the macroscopic electric fields from plasmons to the LO phonon, and leads to significant energy shifts of the measured phonon energy [87]. This effect was often observed for intersubband excitations in modulation doped quantum wells [20, 63]. In Fig. 6.3, it was shown that the LO Phonon always appears at the same scattering energy for all the wires investigated. In case of the 25 nm-wire, where the LO energy is very close to the e_{01} excitation the LO peak seems to be broadened, which was interpreted in terms of Landau damping earlier, but not shifted in energy. Therefore, this is another strong argument for the single-particle character of the excitations. Finally, we would not expect the sum of the h_{01} and e_{01} excitations to equal the energetic difference between PL and PLE, if the Raman peaks included plasmonic shifts. Therefore we believe that our Raman peaks are indeed of single-particle character, and interactions with the background charge carriers do not play any role here. The reason for the redshift of these peaks with increasing power on the other hand is unknown at the moment, it will be discussed in section 6.4.4 that also band gap renormalisation effects are not likely to be its origin.

6.4.3. Comparison of all data to calculated absorption

After discussing all relevant Raman measurements at low excitation powers, the experiments that leave the wires in the one-dimensional quantum limit shall be concluded by comparing all experimental data (including PL and PLE) to the calculated absorption. This is done in Fig. 6.11 for the 25 nm-wire (a) and the 31 nm-wire (b).

For both cases in Fig. 6.11, the theoretical absorption is shown by the two curves in the upper part, where the red stands for absorption with perpendicular and blue for absorption with parallel polarization relative to the wire axis. For this curves, a Lorentzian broadening of 2 meV was assumed to achieve a better comparability to experimental data. In the lower part of Fig. 6.11 the experimental curves are shown. Here, the brown

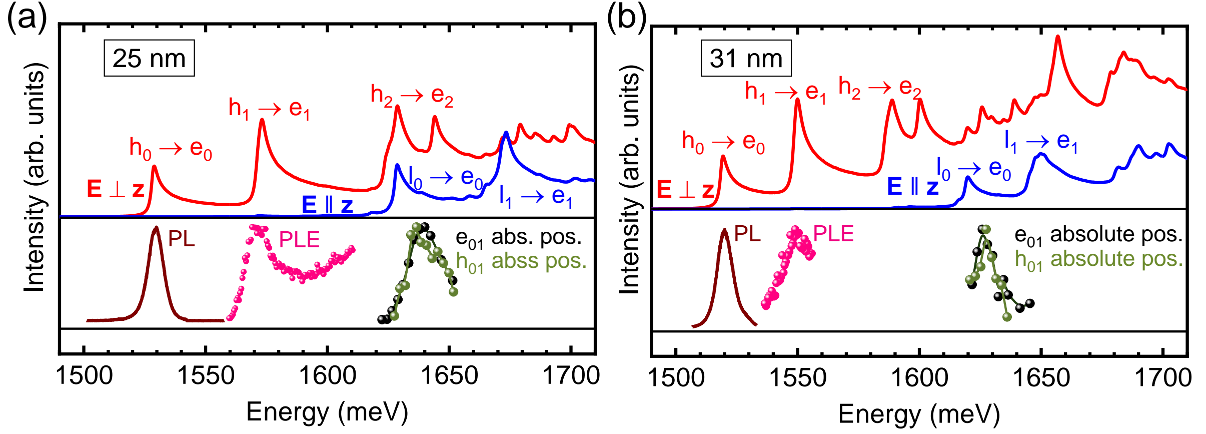

Figure 6.11.: *Comparison of PL, PLE and Raman resonance curves of h_{01} and e_{01} to calculated absorption for the* 25 nm-*wire (a) and the* 31 nm-*wire (b).*

spectrum is the fundamental PL. As for the band structure calculations, the fundamental band gap that corresponds to the PL was omitted, and the theoretical absorption curves are energetically shifted so that the $h_0 \to e_0$ transition agrees with the measured PL position. When subtracting the confinement induced increase of the band gap (as displayed in Fig. 6.8), we get effective values for the fundamental gap E_c of 1496.5 meV for the 25 nm and 1498, 5 meV for the 31 nm-wire. The reason why this values are about 20 meV smaller than the reported wurtzite GaAs band gap energy of around 1520 meV, could be a band gap renormalisation effect, due to the large number of photo-excited charge carriers. Another reason could be that for thinner wires we can not neglect the exciton binding energy any more. Even if the charge-carrier density is in the vicinity of the Mott transition, this binding energy could lead to a decreased band gap, assuming that the effects of band gap renormalisation and vanishing excitonic bound states partly cancel each other, as explained in section 2.2 and 6.4.1. In PL experiments, the effect of an increased exciton binding energy is however overcompensated by the confinement induced increase of the fundamental gap. Therefore, subtracting this from the PL energy could reveal the importance of excitonic effects due to the decreased wire diameter. This would also explain why the effective gap E_c is smaller for the 25 nm-wire.

The PLE data are included by the magenta dots in the lower part of Fig. 6.11. Here, in both cases the peak energy agrees very well with the $h_1 \to e_1$ transition in the calculated absorption. This underlines our interpretation of the h_{01} and e_{01} peaks as single particle excitations, since their sum gives the energetic distance between PL and PLE maxima as mentioned earlier.

The Raman resonance curves are shown in green (black) for the h_{01} (e_{01}) peaks in Fig. 6.11. In contrast to Fig. 6.5, these resonances are now shown on the absolute energy scale, which means that the energy of the scattered photon is plotted. First of all, it is now more obvious than before that both resonances use the same intermediate state, as the curves for the two peaks almost perfectly overlap each other. Furthermore, the resonance maxima agrees reasonably well with the $l_0 \rightarrow e_0$ transition in the calculated absorption. This energy is mainly given by the heavy-light hole splitting in wurtzite GaAs. By using the parameters from reference [50], this value was calculated to be 102 meV, very close to the experimental values reported in section 5.4.

6.4.4. High-power excitation

In this final section about experimental results on GaAs nanowires, the consequences of populating the first excited electron subband e_1 by high excitation powers of 5 mW will be discussed. These results are shown for the 31 nm-wire only, as it was not possible to achieve sufficiently high laser powers at the required excitation energies for the 25 nm-wire. As before, the $\bar{x}\,(z,z)\,x$ polarization configuration was used for this experiment.

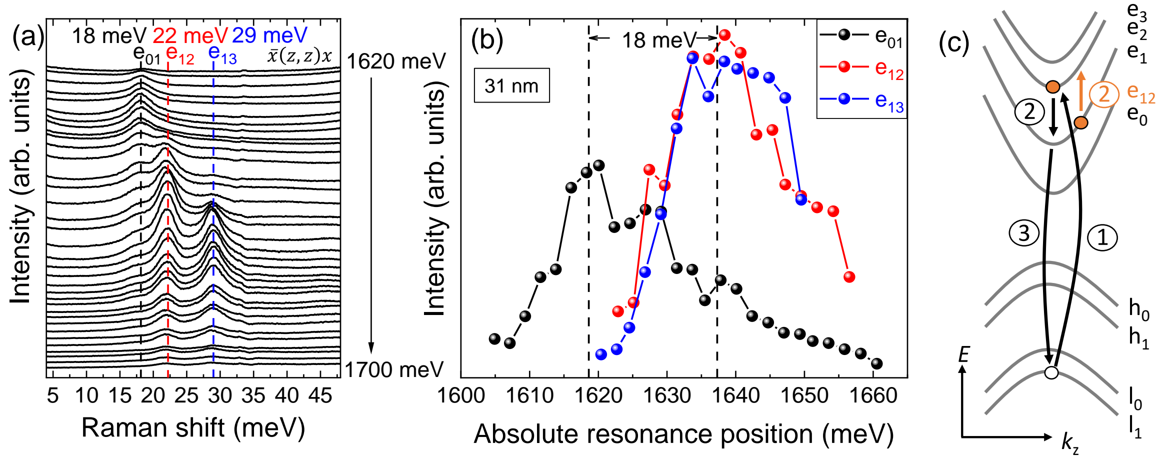

Figure 6.12.: *(a) Excitation-energy dependent series for the* 31 nm*-wire at* 5 mW *power in* $\bar{x}\,(z,z)\,x$ *scattering geometry. Two additional peaks are visible at higher excitation powers, named* e_{12} *and* e_{13}*. (b) Resonance curves for all peaks from (a) on the absolute energy scale. (c) Scattering mechanism for the* e_{12} *excitation, using the* $l_1 \rightarrow e_1$ *transition as the second intermediate state.*

In Fig. 6.12 (a), the Raman spectra are plotted for different excitation energies between 1620 meV and 1700 meV for 5 mW power. At this high power, the h_{01} excitation

is completely Pauli blocked and does not appear in the spectrum any more. The e_{01} excitation on the other hand is now redshifted to 18 meV, which is about $2-3$ meV lower than for the laser powers used before. In addition, two more Raman peaks now appear in the spectrum: The e_{12} peak at 22 meV and the e_{13} peak at 29 meV. These two peaks show a similar resonance behaviour as the e_{01}, but at higher laser energies. The resonance curves extracted from this measurements are shown in Fig. 6.12 (b) for all three peaks. Here, the absolute energy scale is applied again, by subtracting the scattering from the excitation energy, but this time the intensity is not normed. From this plot it is obvious, that the e_{12} and e_{13} resonances overlap on the absolute energy scale, which means that they use the same intermediate state in the scattering process. The situation is different for the e_{01} peak, whose resonance position lies 18 meV lower here. This difference of 18 meV just equals the energy of the e_{01} peak itself at this excitation power, and therefore the splitting between the lowest and first excited electron subband. Consequently, the excitation for the two additional peaks starts at the first excited subband, which is why we assign them to the splitting between first and second (e_{12}) and first to third (e_{13}) excited electron subband. Since the first excited hole subband h_1 stays unoccupied due to its much larger effective mass, we do not expect, and in fact do not find, any higher excitations within the heavy hole subband structure.

The resulting scattering mechanism is exemplary sketched for the e_{12} peak in Fig. 6.12 (c). In this case, the laser excitation starts at the l_1 subband, which means the second intermediate state responsible for the outgoing resonance is the $l_1 \rightarrow e_1$ transition. This means, that the difference of 18 meV between the resonance curves of e_{01} and e_{12}/e_{13} neglects the splitting $l_0 \rightarrow l_1$ in the light hole band. However, from the higher scattering intensity of the e_{12} and e_{13} peaks compared to e_{01} we can see, that this assignment of the second intermediate state for the higher peaks is correct: First of all, the transition also has to be dipole allowed in order to result in such high scattering intensities. And secondly, the resonance curves quite nicely reproduce the calculated blue absorption curve in Fig. 6.11 (b). Also here, the $l_1 \rightarrow e_1$ transition gives the higher absorption than the $l_0 \rightarrow e_0$, explaining the observed intensity ratio of the Raman peaks.

As already mentioned, for a power of 5 mW the e_{01} excitation is redshifted by about 3 meV compared to the lowest excitation power in Fig. 6.10 (a). Comparing the energies of the e_{12} and e_{13} peaks to the band structure calculations in Fig. 6.8 (b), it seems that they are also redshifted due to the high laser power needed for populating the first excited electron subband. From the calculations, we get energies of roughly 27 meV and 36 meV for e_{12} and e_{13}, compared to 22 meV and 29 meV from our measurement with

5 mW power. The experimental proof that all of the peaks are redshifted for high powers is given in Fig. 6.13. Here, a Raman spectrum of the 31 nm-wire is shown for a power of 50 µW, but a high excitation energy of 1656 meV, that enables the scattering mechanism of e_{12} and e_{13}. Due to the low power, the wire is still in the one-dimensional quantum limit, which is proven by the presence of the h_{01} peak. The population of the first excited electron subband, which is needed for the e_{12} and e_{13} peaks, is thus non-thermal. Consequently, the high energy peaks do not dominate the spectrum as in Fig. 6.12 (a), but can only be found as a high energy shoulder of e_{01}. By fitting this spectrum, we find energies of 21 meV, 24.5 meV and 34.1 meV for e_{01}, e_{12} and e_{13}, respectively. The value for e_{01} agrees well with the previously found position of this peak at low powers. The energies of e_{12} and e_{13} show that also these peaks are redshifted by about $2-4$ meV, when using a 5 mW excitation power.

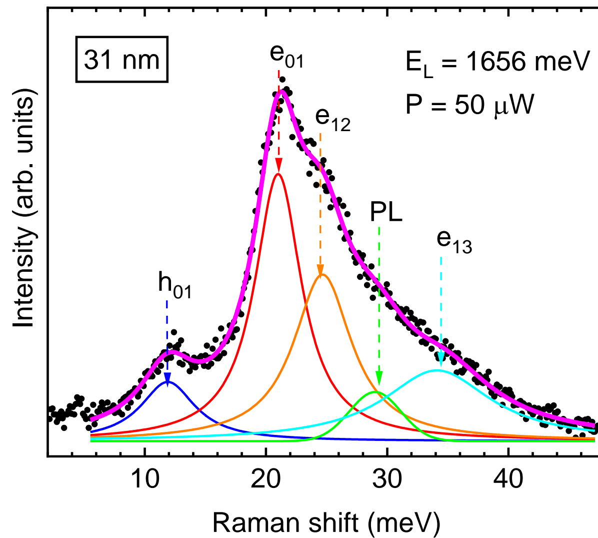

Figure 6.13.: *Raman spectrum of the* 31 nm-*wire using a low power of* 50 µW, *but sufficiently high excitation energy of* 1656 meV *to observe traces of the* e_{12} *and* e_{13} *peaks. The presence of the* h_{01} *peak shows that the wire is in the one-dimensional quantum limit.*

The most intuitive guess on why the Raman peaks are redshifted for increasing laser power is a band gap renormalisation effect, due to the larger charge-carrier density. However, there is a striking difference between our experimental results, and observations in the literature on renormalisation effects in modulation doped GaAs-AlGaAs quantum well structures. In [88] and [89], the authors show by applying a gate voltage, that the PL as well as e_{01} intersubband excitations undergo a redshift when the e_1 subband is

occupied by electrons. In [90], this is taken on step further by monitoring also the e_{12} excitations. Here it is demonstrated, that while the e_{01} excitations redshift due to attractive exchange interaction when populating the e_1 band, the e_{12} excitation blueshifts, since the e_2 band is still unoccupied and thus the repulsive direct coulomb interaction dominates. As already explained, this behaviour is not observed in our investigations, and hence the model proposed in literature is not applicable. We believe, that the redshift of our Raman peaks is due to a many particle interaction effect. However, the exact mechanism is still unknown to us and could not be explained within the time of this thesis.

7. Conclusion and outlook on part two

The goal of this project was to find intersubband Raman excitations in the one-dimensional subband structure of single nanowires. So far, in one dimension such effects had only been observed in arrays of laterally structured quantum wells. Recent progress in the growth of core-shell nanowires using the VLS-method in a MBE chamber, has driven such nanowires into the quantum confinement regime. The successful growth of these samples in the group of Prof. Bougeard, together with the equipment in our laboratories enabling low-temperature Raman measurements with tunable excitation energy in the GaAs band gap range, therefore led to the start of this cooperation.

The wires used for Raman experiments had nominal diameters of 25 nm, 40 nm and 50 nm. They were broken off the growth substrate and dispersed onto a silicon chip. In the next step a pre-characterization was done, to find wires with a single fundamental PL peak, without traces of defect states or trions. All measurements were done one the same wire for every diameter used. The fundamental PL was also used in the Raman experiments to maximize the focus of the laser beam on the wire, and to determine the polarization of incident and scattered light. In PLE experiments, a strong intensity maximum was found in an energetic region where no transition of bulk wurtzite GaAs is expected, pointing strongly towards the formation of one-dimensional subbands. The PLE peak was therefore assigned to the dipole-allowed $h_1 \rightarrow e_1$ transition of the first excited hole and electron subbands.

In the Raman experiments, two unknown peaks that could not be assigned to scattering by phonons, where found in the spectrum. Both of these peaks show a strong resonance, and are only visible for laser excitation energies just above the light hole band gap. As the spectral energy of these peaks scales with the wire diameter as expected for subband energies, and also their sum equals the distance between fundamental PL and PLE maximum, they were assigned to intersubband excitations. The first peak was named h_{01} and interpreted as a hole excitation from the lowest to the first excited heavy hole subband, while the second peak, named e_{01}, was assigned to an electron excitation from lowest to the first excited conduction subband.

From the resonance curves of the h_{01} and e_{01} peaks, it could be concluded that the scattering process for the two peaks uses the same intermediate state. The reason is, that the distance between resonance maxima is the same as the spectral distance of the peaks in the Raman spectrum. Analysing the polarization selection, this intermediate state could be identified as the $l_0 \rightarrow e_0$ transition. Consequently, a three step third order scattering mechanism was proposed, where the excitation and recombination process involves the light hole band, and the scattering is enhanced by an outgoing resonance via the $l_0 \rightarrow e_0$ transition. The free charge carriers that are needed to enable the scattering mechanism are created by the continuous laser radiation, since the wires are undoped.

To check whether the obtained values for the splitting between the first two electron or hole subbands are reasonable, we cooperated with Paulo de Faria Junior, who provided realistic k·p band structure calculations. In case of the 25 nm-wire, the calculated values agreed well with the experimental ones. In case of the 40 nm and 50 nm-wires, the comparison with the calculated band structure led to a correction of the wire diameters to 31 nm and 41 nm, respectively. In these two cases, the agreement between theory and experiment is given by finding a wire diameter for which both the experimental heavy hole and conduction band splittings fit to the calculation at the same time.

To get an idea of the charge-carrier density during the Raman experiments, the minimal linewidth of the e_{01} peak, which is induced by momentum transfer due to the numerical aperture of the microscope objective, was calculated with respect to the charge-carrier density. The charge-carrier densities, for which the wires are in the one-dimensional quantum limit, were derived from the measured $e_0 \rightarrow e_1$ splitting for every diameter. Comparing this calculation to the experimental peak width, it showed that the 25 nm-wire was in the one dimensional quantum limit for the used excitation power of 50 µW. The other two wires were found slightly above the critical density for the one-dimensional quantum limit. This did not allow to make a definite conclusion, since the experimental linewidth is expected to contain inhomogeneous broadening. It was shown by monitoring the $h_1 \rightarrow e_1$ hot PL in laser-power dependent measurements, that also these wires were in the one-dimensional limit for 50 µW. Also, the charge-carrier density could be determined more precisely, which also revealed the percentage of inhomogeneous broadening in the peak width.

Power-dependent experiments also showed that the h_{01} excitation vanishes for increasing carrier density, which was explained by Pauli blocking of the scattering mechanism, when increasingly populating the conduction band with electrons. It was also shown

that all Raman peaks redshift, when the carrier density increases. Together with the measured polarization selection rules, it was concluded that this shift is not of plasmonic nature, and the Raman excitations are mainly of single-particle origin. This was supported by the absence of both a depolarization shift and a plasmon-phonon coupling, as well as the good agreement between PLE and Raman data.

For a high excitation power of 5 mW, when the first excited conduction subband is occupied by electrons, two additional Raman peaks could be resolved for the 31 nm-wire. These were interpreted as e_{12} and e_{13} excitations, and are resonantly enhanced to the $l_1 \rightarrow e_1$ transition. It could be shown that also these peaks are redshifted by the high excitation power compared to the single-particle case. However, this behaviour is in contradiction to observed Raman peak shifts in modulated quantum well structures due to band gap renormalisation. Therefore, the exact mechanism leading to this redshift remained unknown.

Since all electronic Raman effects in our measurements have been interpreted as single-particle excitations, the question arises why it was not possible to observe plasmonic effects, which are very common in GaAs quantum structures. The most obvious guess would be, that doping free wires, as we have examined, do not show collective excitations of charge carriers. In former experiments on GaAs quantum-well structures, the samples were usually modulation doped, which enables high electron densities and mobilities at the same time. In contrast to that, all free charge carriers in our core-shell wires were created by continuous laser radiation. Consequently, these carries are constantly relaxing and recombining back to lower band states, which probably hinders the formation of any collective oscillations. Hence, one way to go forward could be to introduce free electrons into the wires, either by doping atoms or by contacting wires electrically, in order to find CDE and SDE excitations.

One other experiment that is very common for GaAs quantum-well structures, is to measure the dispersion of intraband excitations by tilting the sample, and therefore varying the transfer of photon momentum parallel to the sample plane. However, the need to use a microscope objective to focus the laser beam on single wires lying on the substrate, complicates such experiments immensely. First of all, the tilting axis would have to be perpendicular to the wire axis, which is not trivial since the wires are randomly orientated on the substrate. This random positioning also becomes an issue, when wires of interest are in the middle of the substrate, as tilting it then moves them away from the cryostat window so much, that they cant be reached with the working distance of the objective any more. And lastly, experience with tilting two-dimensional

crystals showed, that it is virtually impossible to read or focus on the gold numbers for orientation on tilted silicon substrates, when using a 100X objective. Finding the desired wire, and focussing the laser beam on it using tilt angles, is therefore even harder to manage. One possible way to overcome these problems could be to fabricate substrates with a diffraction grating on top, providing the momentum transfer parallel to the wire axis. The big disadvantage of this method would be that it is very time consuming. It would be necessary to produce different gratings for every needed momentum transfer value, and to pre-characterize the wires put on top every time.

One experiment that could be realized a lot easier, would be to investigate the effects of external magnetic fields on the electronic Raman excitations. The described micro Raman setup from section 4.2, that was built for two-dimensional crystals, could also be used for single nanowires. A magnetic field could be used to further confine charge carriers in the wires. Typical effects in one-dimensional structures are the formation of skipping orbits, that become closed orbits inside the wire for sufficiently large field strengths [60]. Therefore, it could be rewarding to check if a Landau substructure of the discovered Raman peaks is experimentally achievable.

Part III.

Resonance effects in $MoSe_2$-WSe_2 heterostructures

In this third part of the thesis, resonant Raman measurements on $MoSe_2$-WSe_2 heterostructures will be presented. The initial motivation for this project was to exploit the accessibility of the $MoSe_2$ direct band gap by the Ti:Sapphire laser, enabling a tuning of the excitation energy across the A exciton transition. This could potentially reveal new Raman features, that are not visible in the off-resonant case. To avoid the problem of strong PL that over shines the Raman lines in the resonant case, these experiments were done on a heterostructure, that partially quenches the emission of intralayer excitons.

As in the previous part, the theoretical foundations of the material system will be presented first, starting with a short overview over the crystal structure and electronic properties of TMDCs. In the following, the properties of the already known Raman modes will be summarized, before finally discussing heterostructures of $MoSe_2$ and WSe_2. In the end of this chapter, the process of our sample production is shortly explained.

In chapter 9, the experimental results of the described measurements are presented. As will be shown, we find a so far unknown Raman peak at low wavenumbers, which is only visible close to the trion energy of $MoSe_2$. The dependence of this peak on polarization, temperature, external magnetic fields and twist angle of the heterostructure is then presented. This allows us to propose, that the peak must stem from an interlayer effect rather than being confined to the $MoSe_2$ monolayer. Unfortunately, we so far have no understanding of the exact mechanism that leads to the formation of this Raman peak. Therefore, only possible explanations on the effect are discussed in the end of chapter 9.

8. Basic principles of TMDCs

The discovery that graphite could be thinned down to single layer graphene in 2004 [10] by mechanical exfoliation started a huge research area about two dimensional crystals. It was soon realized, that also monolayers of other layered van der Waals crystals could be prepared by this method, including the TMDC MoS_2 [11]. In contrast to graphene, these types of materials are semiconductors [91–93], and thus better suited for optical experiments. In the following, the basic properties of this material class are discussed. Among TMDCs, MoS_2 is considered to be the prototype material due to its high natural occurrence [94]. Therefore, many basic properties presented in this chapter were first derived for MoS_2, but are also applicable for $MoSe_2$ and WSe_2, which are used in this work.

8.1. Crystal structure of TMDCs

TMDCs are described by the formula MX_2, where M stands for a transition metal (like molybdenum or tungsten) and X for a chalcogen atom like sulphur or selenium. Their crystal structure was first described by Dickinson and Pauling for the case of bulk MoS_2 in 1923 [95]. In their bulk form, TMDCs consist of individual layers stacked on top of each other, which are only bound by weak van der Waals forces. Within one of those layers, the atoms are covalently bound and arranged in trigonal-prismatic unit cells, as can be seen in Fig. 8.1 (a). This means that in contrast to graphene, one monolayer consists of three layers of atoms, with two chalcogen layers surrounding one layer of transition metals. The overall height of such a monolayer is then about 6 Å. The distance between chalcogen atoms in a unit cell is called a and measures 3.288 Å for $MoSe_2$ [96] and 3.286 Å for WSe_2 [97]. For the ideal crystal, b is then given by $b = \sqrt{7/12}a$.

When stacking such monolayers on top of each other, there are two possible configurations, which are illustrated in Fig. 8.1 (b). In case of the 2H configuration, two neighbouring layers are twisted with respect to each other by 60°. Hereby, the transi-

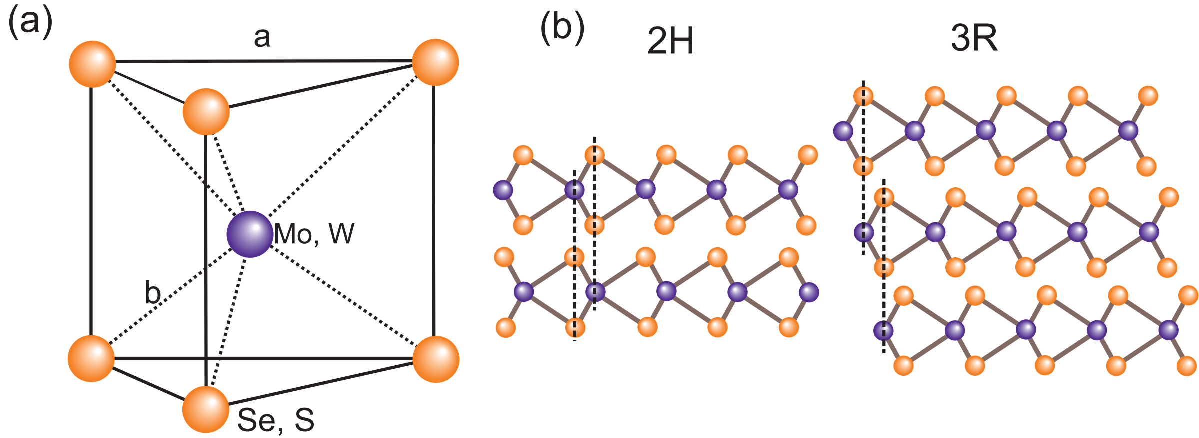

Figure 8.1.: *(a) Trigonal prismatic unit cell of the TMDC crystal structure. The transition metal atom in the center is surrounded by six chalcogen atoms at the corners. (b) The two possible stacking configurations for multilayer TMDCs. In case of the 2H type, two neighbouring layers show a relative twist angle of* 60°*, whereas the 3R configuration corresponds to relative twist angles of* 0°*.*

tion metal atom of the upper layer lies on top of the chalcogen atoms of the lower one, and vice versa. The stacking order repeats after two layers and leads to a hexagonal symmetric crystal. In contrast, for the 3R configuration the relative twist angle of neighbouring layers is 0°. Consequently, the chalcogen atoms of the upper layer lie on top of the transition metal of the lower one. This stacking order repeats after three layers and leads to a rhomohedral symmetry. Naturally occurring MoS_2 is predominately observed in the 2H configuration [94], which makes it also the standard configuration for other TMDCs. Therefore, all natural multilayers in this thesis show the 2H stacking, the 3R is only used for artificially stacked heterostructures.

8.2. Electronic properties

8.2.1. Band structure of TMDCs

As a consequence of the crystal structure, the Brillouin zone adapts a hexagonal form [91], that is illustrated in Fig. 8.2(a). Before the discovery of mechanical exfoliation, several band structure calculations of TMDCs were done for their bulk form [92, 93, 98, 99], and showed that these materials are indirect semiconductors. Within the hexagonal Brillouin zone, the valence band maximum was found at the Γ-point and the conduction band minimum between the Γ- and K-point. However, since it turned out that MoS_2

monolayers could be produced just like graphene [11], TMDCs came back into the focus of scientific investigations. Several theoretical works predicted a transition from an indirect to a direct band gap semiconductor when thinning down TMDCs to a single layer [100–102]. These predictions were verified in 2010, by finding a drastic increase in the PL intensity for monolayer MoS_2 compared to bilayer samples [12, 13]. The same behaviour was soon also measured for $MoSe_2$, WSe_2 and WS_2 [103–105].

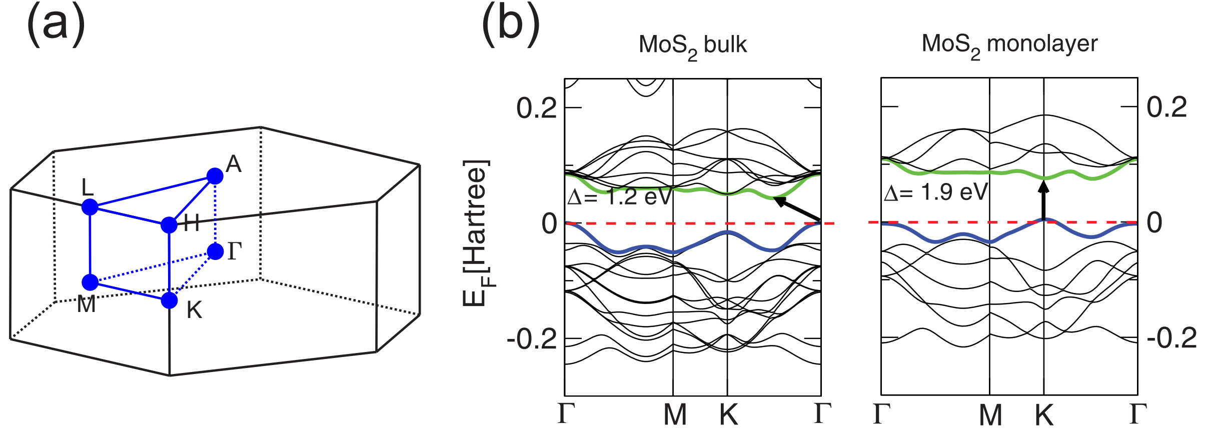

Figure 8.2.: *(a) Hexagonal Brillouin zone of TMDCs, showing the most important symmetry points. (b) Transition from an indirect band gap for bulk MoS_2 (left) to a direct one for the monolayer. The direct gap at the K-point stays unchanged in this transition, whereas the extrema of the indirect gap shift to higher or lower energy. Adapted from [106].*

The transition from indirect to direct band gap is shown for MoS_2 in Fig. 8.2 (b). By calculating the bulk and monolayer band structure of MoS_2, it can be seen that the valence band maximum at Γ shifts downward and the conduction band minimum between Γ and K upward, when thinning MoS_2 down to a single layer. This leaves a direct band gap at the K-point. This transition can be explained considering the interlayer interaction seen by the atomic orbitals, that the states at different points in the Brillouin zone are made of [13, 107]: The states at the K-point are mostly made of d-orbitals by the transition metals, that are localized in the middle of a TMDC monolayer and thus are not influenced by neighbouring layers, leaving the K-point gap almost unchanged when going from bulk to monolayer. The states near the Γ-point on the other hand are linear combinations of d-orbitals from transition metals and p_z-orbitals from the chalcogen atoms. The latter lie at the surface of a TMDC monolayer, and are therefore strongly influenced by interactions with neighbouring layers.

In addition to becoming a direct semiconductor, another important effect happens

for TMDC monolayers compared to their bulk counterparts. Since the monolayer does not have an inversion center any more, the Kramers degeneracy is lifted, and together with spin-orbit coupling leads to a spin splitting of conduction and valence bands at the K-points [107–112]. As the K-points are connected by time reversal symmetry, the splitting shows opposite sign in K^+ and K^- valleys, as can be seen in Fig. 8.3. When comparing molybdenum and tungsten based TMDCs, one finds that the valence band splitting shows the same sign in all materials, but the conduction band splitting is reversed, accompanied by conduction band crossings close to K for the molybdenum compounds. Calculated values for $MoSe_2$ give a splitting of $\Delta_{CB} = -22\,\text{meV}$ for for the conduction band and $\Delta_{VB} = 186\,\text{meV}$ for the valence band. For WSe_2 the corresponding value are $\Delta_{CB} = 37\,\text{meV}$ and $\Delta_{VB} = 466\,\text{meV}$ [113]. These numbers were experimentally confirmed by many working groups, finding very similar values [105, 114–119].

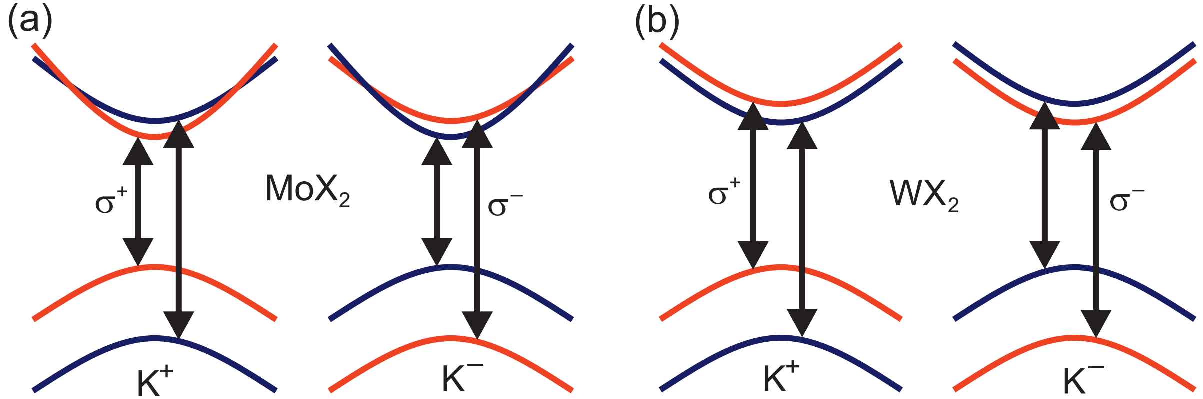

Figure 8.3.: *Spin splitting and optical selection rules for molybdenum based TMDCs (a) and tungsten based TMDCs (b). Red bands are spin up states, blue spin down. Allowed optical transitions are indicated by arrows.*

The valley specific spin splitting of the electronic bands also leads to valley dependent optical selection rules [109, 120], which are shown in Fig. 8.3. The notation of K^+ and K^- valleys already implies, that optical transitions are only possible using σ^+ circular polarized light in the former, and σ^- circular polarized light in the latter valley. A transition starting from the upper valence band is hereby called an A exciton, whereas a transition from the lower valence band leads to a B exciton [99]. From the conduction band ordering it follows, that the A exciton has an optically bright ground state in molybdenum, but a dark ground state in tungsten based materials.

Exciting a TMDC monolayer with circularly polarized light consequently leads to an excess of created excitons in the chosen valley compared to the other one. This effect is

known as the valley polarization, which can be measured in PL by comparing the ratio of emitted σ^+ and σ^- polarized photons following a valley selective excitation [121–124]. In the special case of $MoSe_2$ however, a valley polarisation can only be created for near resonant excitation, and even then still reaches significantly smaller values than for the other TMDCs [125]. It is believed that this behaviour partly stems from the optically bright A exciton state, which does not lead to a reservoir of spin polarized charge carriers like in the tungsten based materials.

8.2.2. Excitons in TMDCs

In section 2.1 of this thesis equation (2.2) was derived, that quantifies the exciton binding energy and the Rydberg series of excited excitonic states. In ideally two-dimensional systems this formula is however modified, since the electron and hole wave functions are confined in the sample plane and therefore show a stronger overlap. In this case, the energy of excitonic states can be expressed as [60]

$$E_r^{2D} = E_r\left(\infty\right) - \frac{R^*}{\left(n-\frac{1}{2}\right)}, \tag{8.1}$$

where, as before, $E_r\left(\infty\right)$ is the band to band transition energy and R^* the modified Rydberg constant. Compared to the formula for three-dimensional crystals, the binding energy of the ground state ($n = 1$) is therefore enhanced by the factor four.

However, in the case of TMDCs, the observed exciton binding energies even exceed the values predicted by equation 8.1. This was first explained by Chernikov et al. [17] and is illustrated in Fig. 8.4. In contrast to a bulk crystal, for TMDCs the electric field lines between electron and hole partly extend to the vacuum surrounding the sample, which reduces the screening of Coulomb interaction and consequently enhances the exciton binding energy. This effect is even stronger for excited exciton states, as the Bohr radius increases and therefore even more field lines propagate outside the sample, leading to a deviation from the Rydberg series.

Overall, the described effects cause exciton binding energies in the range of a few hundred meV for TMDC monolayers, which makes excitons stable even at room temperature. A summary on the exact binding energies which were experimentally obtained for different materials can be found in [126]. Despite these huge binding energies, excitons in TMDCs are still regarded as Wannier-Mott excitons, since the Bohr radius lies in the range of nanometres and hence still extends over several unit cells [127, 128].

Having discussed the binding energies, a closer look will now be taken on the exci-

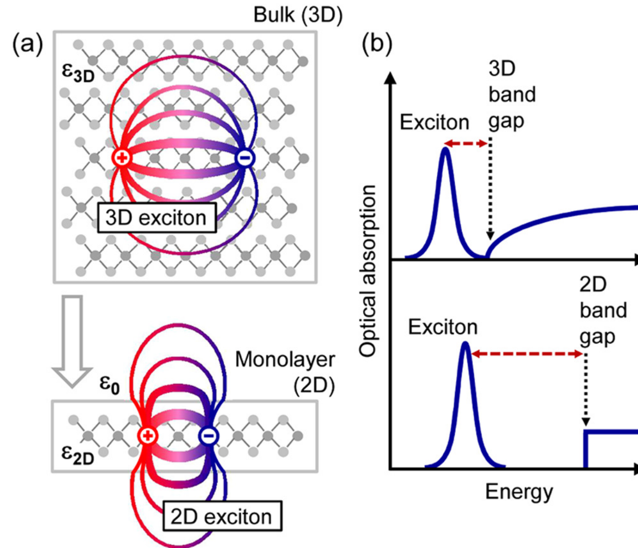

Figure 8.4.: *(a) Screening of the Coulomb interaction between electron and hole for bulk and two-dimensional crystals. For two-dimensional monolayers the electric field lines propagate partly outside the sample. (b) Consequences for the exciton binding energy, showing a enhanced gap between fundamental band gap and excitons in two dimensions. Taken from [17].*

tonic complexes that show up in PL measurements for $MoSe_2$ and WSe_2. Fig. 8.5 (a) comprises a reflectivity (upper part) and a PL measurement (lower part) of monolayer $MoSe_2$ at cryogenic temperatures. In reflectivity the A and B excitons show up, which are separated by the valence band splitting, as explained earlier. In PL, a strong emission line can be found at about 1.66 eV, that clearly corresponds to the A exciton. However, 30 meV below that another strong PL feature appears, that was identified as the negatively charged trion by gate voltage dependent measurements [129]. Such a trion can be seen as an excitonic quasiparticle, consisting of an additional electron bound to an A exciton, and thus having a larger binding energy than the neutral exciton, here by 30 meV. In order to build trions, these additional electrons have to be present in the conduction band due to doping. It is usually observed by gate voltage dependent measurements (see [129]) that $MoSe_2$ is naturally n-doped, and therefore the observed trions are negatively charged. The trion PL peak vanishes from the spectrum for increasing temperatures, which will become more important later when discussing our experimental results.

In WSe_2, there are a lot more excitonic particles observable in PL, which is mostly due to the dark excitonic ground state in tungsten based TMDCs [130–132]. Fig. 8.5 (b) shows a gate voltage dependent PL measurement of a WSe_2 monolayer at cryogenic

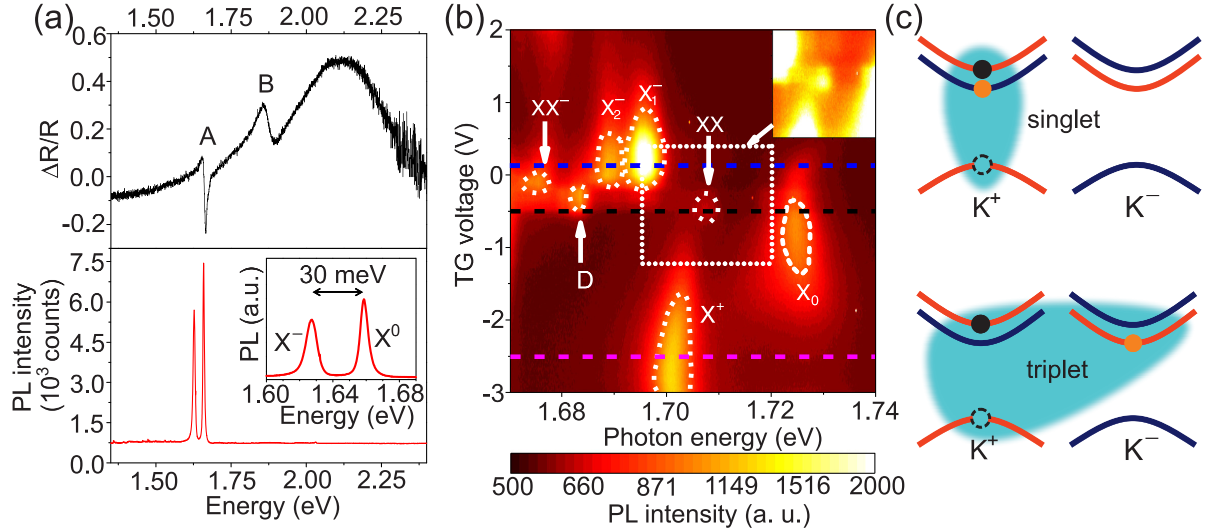

Figure 8.5.: *(a) Reflectance contrast (upper part) and PL measurement (lower part) of $MoSe_2$ at cryogenic temperatures. In reflectance, the A and B excitons show up, in PL the A exciton and* 30 meV *below that the negatively charged trion. Adapted from [129]. (b) Gate voltage dependent PL spectra of WSe_2 at cryogenic temperatures. X^0 stands for the neutral A exciton, XX the neutral biexciton, X^+ the positively charged trion, X_1^- the negative triplet trion, X_2^- the negative singlet trion, D the dark A exciton and XX^- the negatively charged biexciton. Adapted from [130]. (c) The two types of negatively charged trions in tungsten based TMDCs. The singlet trion (upper part) has a higher binding energy and hence appears at lower PL energy than the triplet trion (lower part).*

temperatures. In addition to the $MoSe_2$ PL, also neutral biexcitons (XX), the dark A exciton (D) and the negatively charged biexciton (XX^-) can be found in this material. Most important for this thesis is however the splitting of the negatively charged trion, into a triplet state (X_1^-) and a singlet state (X_2^-). These types of trions are sketched in Fig. 8.5 (c). For the singlet trion, the two electrons have opposite spin, with the optically excited electron (black) sitting in the upper conduction band and the doping electron (brown) in the lower conduction band of the same valley. For the triplet trion, the doping electron sits in the lower conduction band of the opposite valley, and therefore has the same spin as the optically excited one. In this case, exchange interaction opens a gap in the trion dispersion, and the triplet trion is observed at higher energies [133]. This splitting is typically detectable in the PL of tungsten based TMDCs (for WS_2 see for example [134]). The positively charged trion (X^+) on the other hand does not have a triplet state, since the additional hole always sits in the upper valence band, and therefore sits in the opposite valley than the optically excited hole. Below the PL peaks

shown in 8.5 (b), even more peaks can be observed in WSe_2, which are interpreted as defect bound excitons [135, 136], but are not of further importance for this thesis.

8.2.3. Behaviour under external magnetic fields

To conclude the electrical properties of monolayer TMDCs, their behaviour under external magnetic fields perpendicular to the sample plane shall be briefly discussed. For TMDCs, the energetic shifts of the electronic bands were initially explained by summing up contributions from spin, valley magnetic moment and orbital magnetic moment. The latter of these contributions lifts the degeneracy of the optical band gaps in different valleys, that is present at zero magnetic field [137]. Recently, this approach was gradually abandoned, as several groups presented models that could explain the experimentally observed band shifts by first principle calculations [138–141]. In the following, the effect of a magnetic field on the PL is just presented phenomenologically.

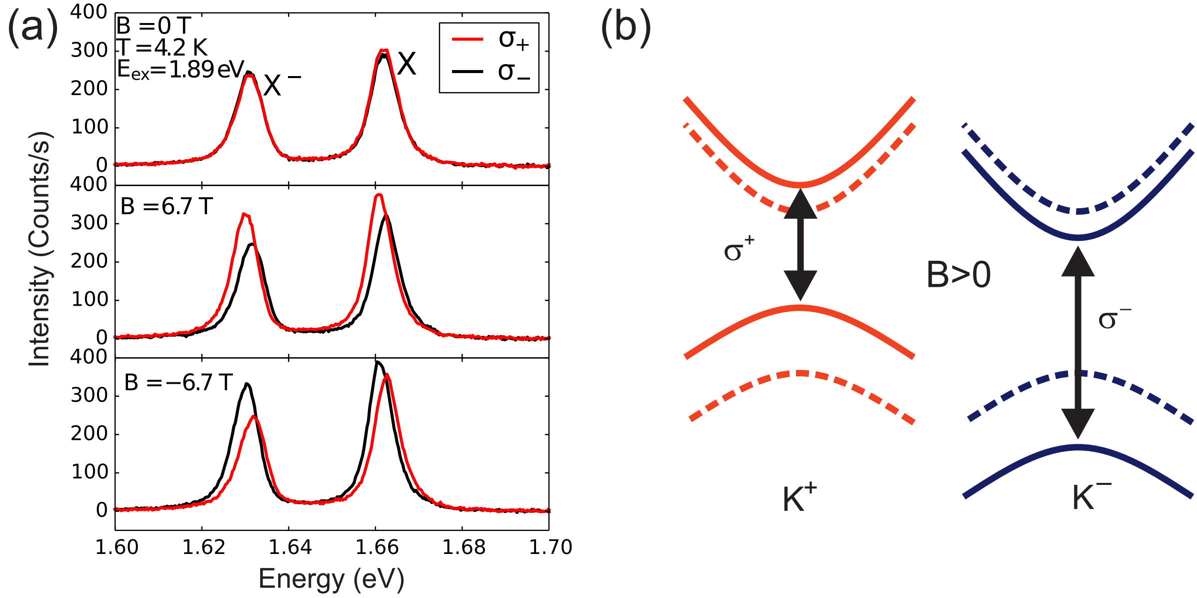

Figure 8.6.: *(a) Polarization resolved PL of monolayer $MoSe_2$ for zero magnetic field and ±6.7 T. Adapted from [142]. (b) Shift of conduction and valence band in $MoSe_2$ due to a positive perpendicular B-field. Dotted lines present the situation without magnetic field.*

Fig. 8.6 (a) displays a low-temperature PL experiment of $MoSe_2$ for zero and ±6.7 T. For this PL measurement, the sample was excited by unpolarized light, however in the emission σ^+ (red) and σ^- (black) polarized components were resolved. In case of zero

magnetic field, the PL curves for both circular polarisations match almost perfectly, indicating that both valleys are equally populated and have an identical band gap. For positive magnetic field, two differences are apparent; an increase of intensity, accompanied by a decrease in photon energy of σ^+ polarized light compared to σ^- polarization. The reason for this behaviour are the band shifts drawn in Fig. 8.6 (b). The dotted lines show the position of bands without external magnetic field, the solid lines for a positive field perpendicular to the sample. As can be seen, in the K^+ valley both valence and conduction band are shifted upwards in energy, however the valence band by the larger amount, leading to a decreased band gap. In the K^- valley, the situation is reversed. As the K^+ transition is now energetically favourable, it appears at higher intensity in the PL spectra. For negative magnetic fields, the situation is just the opposite, which is shown in the lowest panel of Fig. 8.6 (a).

The energetic shift between σ^+ and σ^- polarization gives rise to the so called effective g factor g_{eff}, which is given by

$$E_{\sigma^+} - E_{\sigma^-} = g_{eff}\mu_B B\,, \tag{8.2}$$

where μ_B is the Bohr magneton. In the example of Fig. 8.6 (a), this led to $g_{eff} = -3.8$ for monolayer $MoSe_2$ [142]. A summary of experimentally measured effective g factors and a comparison to calculated values can be found in [138] and [140].

8.3. Raman spectroscopy of TMDCs

8.3.1. Intralayer modes

Similar to the electronic properties, the vibrational modes in TMDCs were first described for bulk MoS_2, for example by Verble and Wieting in 1970 [143]. The number of optical phonons reduces for the monolayer compared to bulk. However, many of the additional modes in the bulk are connected to monolayer modes (apart from shear and breathing modes), as they have the same atomic displacements within one layer, but varying phase shifts between neighbouring layers [144]. Also, due to the changing space group of the crystal, the given names of the modes change for different layer number. For simplicity, in this thesis only the notation for the bulk crystal will be used.

The most important intralayer optical phonon modes in TMDCs are the A_{1g} and the E^1_{2g}, which are shown in 8.7 (a) and (b), respectively. The A_{1g} is an out-of-plane mode, which is characterized by a single branch in the phonon dispersion, while the in-plane

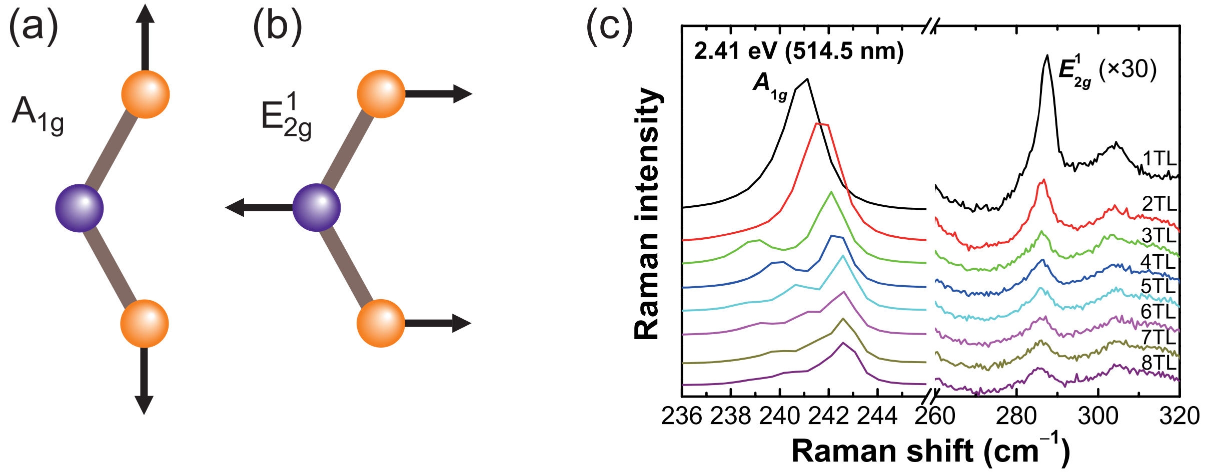

Figure 8.7.: *Atomic displacements for the A_{1g} phonon mode (a) and the E^1_{2g}-mode (b). (c) Raman spectra of both phonon modes in $MoSe_2$ for different layer numbers. Taken from [145].*

mode E^1_{2g} has two branches for LO/TO propagation, which are degenerate at the Γ-point [144, 146]. Both of these modes are Raman active in the backscattering geometry used in this thesis, but show different polarization selection rules; the A_{1g} appears for co-polarized linear polarization only, while the E^1_{2g} shows up for both co and crossed linear polarizations.

Fig. 8.7 (c) is a typical spectrum of these modes for different layer numbers of $MoSe_2$ at room temperature. The A_{1g}-mode shows up at about 241 cm^{-1} for monolayers and shifts to higher wavenumbers when increasing the number of layers [147, 148]. This is explained by the intuitive picture, that each additional layer adds another "spring" to the out-of-plane vibration of the atoms. For three layers ore more, a second mode at slightly lower energy appears, which is due to an out-of-phase vibration of the atoms in the middle layer. The E^1_{2g} shows up close to 290 cm^{-1} in $MoSe_2$, and shifts to lower wavenumbers for increasing sample thickness. For this mode, the stronger screening of long-range coulomb interaction for more layers leads to a reduction of the force constant [149]. In case of WSe_2, the A_{1g} and E^1_{2g} are at almost the same energy (≈ 250 cm^{-1}) at the Γ-point and therefore difficult to differentiate [103, 144]. In $MoSe_2$ on the other hand, the spectral difference between these modes is a good way to determine the number of layers in a sample.

With respect to the laser excitation energy, it is observed that the A_{1g}-mode is resonantly enhanced with the A and B exciton transitions [145, 150]. In contrast, the E^1_{2g}-mode shows resonances with higher excitonic transitions, which involve electronic

states outside the K-point of the Brillouin zone. The explanation for this behaviour uses the vibration direction of the atoms in relation to the atomic orbitals. As already mentioned, the states at the K-point of the Brillouin zone are mostly made out of transition metal d-orbitals, which are confined within one monolayer. The A_{1g}-mode therefore shows a high electron-phonon coupling to these states, due to its out-of-plane vibration of chalcogen atoms [151, 152]. The E^1_{2g} on the other hand does not change the thickness of a monolayer, and hence does not couple to K-point states. It is only enhanced for higher transitions such as the C-exciton, which involves conduction band states close to the Γ-point, and therefore also p-orbitals of the chalcogen atoms.

8.3.2. Interlayer modes

For multilayer TMDCs, there are also two phonon modes that are absent in the monolayer: The so called layer shear and layer breathing modes [153, 154]. These modes are vibrations of complete layers with respect to each other; either in the xy-direction, which is called the shear mode (see Fig. 8.8 (a)), or in the z-direction, which is the breathing mode (8.8 (b)).

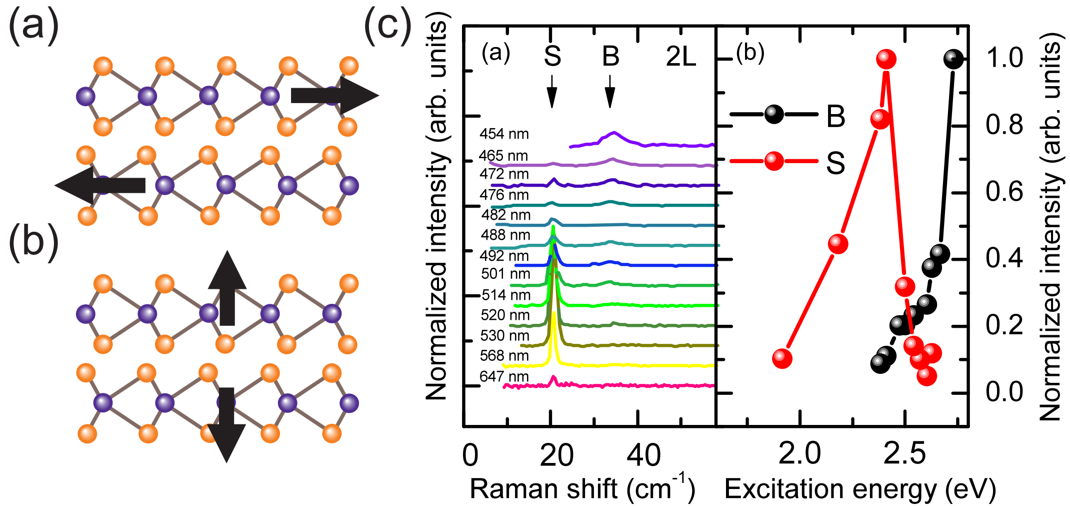

Figure 8.8.: *Vibration directions of the layer shear mode (a) and the breathing mode (b). (c) Left panel: Shear and breathing modes in the Raman spectrum of bilayer $MoSe_2$ for different laser lines. Right panel: Excitation energy dependence for the breathing mode (black) and the shear mode (red). Taken from [150].*

Since the restoring forces for those modes are only the weak van der Waals interactions between the individual layers, they are found at very low Raman shifts, as can

be seen in the left panel of Fig. 8.8 (c): Here, the shear mode is found just above $20\,\mathrm{cm}^{-1}$ and the breathing mode close to $35\,\mathrm{cm}^{-1}$ for bilayer $MoSe_2$ [150]. Just as for the A_{1g} and E^1_{2g}-modes, the Raman shift does however depend on the number of layers. For the shear mode, adding more layers increases the number of out-of-phase oscillations, as neighbouring layers show a phase shift of π, which increases the energy. For the breathing mode the opposite happens; here the number of in-phase oscillations is increased for thicker samples, leading to a redshift of the Raman peak [155]. Also the polarization selection rules resemble the A_{1g} and E^1_{2g}-modes [156]; the breathing mode is only observed for co-polarized linear polarizations, whereas the shear mode appears for both co and cross-polarized linear polarizations.

The behaviour of these modes with respect to laser excitation energy is shown in Fig. 8.8 (c). From plotting the modes intensity for different laser lines, it is concluded that the shear mode shows a resonance at 2.4 eV, which is close to the C exciton. The breathing mode on the other hand does not show a clear resonance within the range of the laser energies applied here, but rather increases in intensity with photon energy. Both of these modes are therefore not resonantly enhanced with the A and B exciton states [145, 150]. This is also not expected, since the modes do not change the thickness of a monolayer, and therefore do not couple to the Mo-d-orbitals, which the K-point states are made of.

8.4. TMDC heterostructures

Having described the properties of monolayer TMDCs, the consequences of stacking two different monolayers on top of each other to form a heterostructure are presented in the following. In this case, only the combination of $MoSe_2$ and WSe_2 will be discussed.

8.4.1. Moiré lattice and atomic reconstruction

The first point to consider when stacking different van der Waals materials on top of each other, is the kind of superlattice the heterostructure is arranged in. This property is dependent on the twist angle of the layers, which in TMDCs takes values between $0°$ and $60°$ due to the hexagonal crystal structure [157]. For non-zero twist angles, the formation of a Moiré supperlattice is expected, that was observed in twisted bilayers of graphene first [158], but later also for bilayers of MoS_2 [159] or TMDC heterostructures [160]. Such a Moiré lattice is drawn in Fig. 8.9 (a) for an relative twist angle of $\Theta = 10°$.

Here, a new, much larger periodicity is observable, that is inversely dependent on the twist angle, forming a smaller supercell for larger angles. For artificially stacked bilayers of the same material, a twist angle is required in order for a Moiré lattice to form, since the lattice constants of the individual layers are identical. For heterobilayers, already the slight mismatch of lattice constants should induce a Moiré structure for 0° or 60° twist angle. However, it was shown by Weston et al [161] for homobilayers and Rosenberger et al for heterobilayers of TMDCs [162], that for small deviations from 0° or 60°, no Moiré lattice, but a reconstructed crystal structure is found.

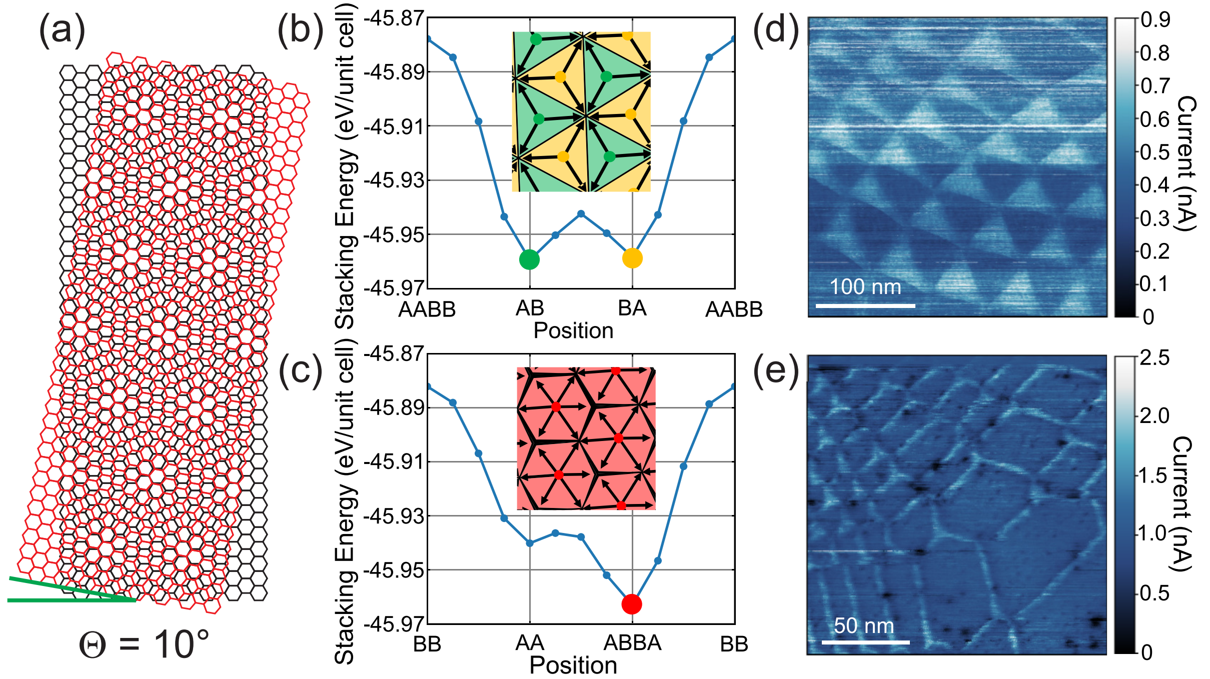

Figure 8.9.: *(a) Moiré superlattice of two monolayers with honeycomb structure for a twist angle of $\Theta = 10°$. (b) Stacking energy for different high-symmetry points in a Moiré structure for a small deviation from 0° twist. (c) Same as (b) for a small deviation from 60° twist. (d) Conductive AFM picture for a R-type reconstructed heterostructure, showing triangular domains. (e) Same as (d) for a H-type structure, showing hexagonal domains. Adapted from [162].*

The foundation of atomic reconstruction is the stacking energy of different high-symmetry points in the Moiré structure, as plotted in Fig. 8.9 (b) for small deviations from 0° stacking and in (c) for small deviations from 60° stacking. For the former case, two points within the Moiré lattice show a minimum in stacking energy, which are called AB and BA here. The BA position corresponds to a point in the Moiré lattice, where the chalcogen atoms of the upper layer lie on top of the transition metal atom of the

lower layer. As already shown in Fig. 8.1 (b), this corresponds to an ideal 3R stacking. The position AB also replicates an ideal 3R stacking, but reverses the order of the layers, with the transition metal of the upper layer lying on top of the chalcogen atom of the lower layer. These points periodically repeat over the Moiré lattice. As their stacking energies are degenerate minima, the heterostructure forms triangular domains (see insert of (b)), in which the heterostructure adapts the configuration of exactly the AB or BA point. For small deviations from 60° twist, there is only one minimum in the stacking energy, which is the ABBA point. In this symmetry point, the transition metal of the upper layer lies on top of the chalcogen atom of the lower layer and vice versa, which is the ideal 2H configuration. The domains therefore are hexagonal. Fig. 8.9 (d) and (e) give the experimental evidence of the atomic reconstruction, showing triangular or hexagonal domains in a conductive AFM measurement. This reconstruction however only occurs for small deviations from 0° or 60° stacking, which will only be called R-type and H-type from now on. For larger twist angles, the Moiré period and therefore the size of the domains gets smaller, increasing the amount of energetically unfavourable domain walls, until for a certain angle the formation of a Moiré lattice is preferable again. For this critical deviation angle different values have been reported, ranging from 1° [162] to about 5° [163]. A criteria to decide whether a heterostructure is reconstructed or not, is the spectroscopy of shear modes, which is discussed in the following.

Interlayer shear and breathing modes had been investigated for twisted homobilayers of TMDCs and heterostructures before the discovery of atomic reconstruction [165–170]. In general, it was observed that the breathing mode appears for all twist angles, while the shear mode only shows up for closely aligned H- or R-type bilayers. It was later confirmed by Holler et al, that this is a direct consequence of having a reconstructed crystal structure or a Moiré lattice [164]. Fig. 8.10 shows a low-frequency Raman measurement at room temperature of several $MoSe_2$-WSe_2 heterostructures, whose twist angles are given in the upper right panel. It is generally indicated whether the sample is of H- or R-type, with the deviation from the ideal stacking given in brackets. The first two graphs in the left panel belong to H-type heterostructures and show a strong shear mode at $18\,cm^{-1}$. The following three are R-type structures, which show a weaker mode at slightly lower wavenumber ($17.4\,cm^{-1}$), as displayed in (b) in more detail. The last three structures have either a larger deviation from the ideal stacking angle (6°) or are completely misaligned. These do not show any sign of a shear mode at all. The reason for this behaviour is, that the shear mode needs an atomic registry as its restoring force, which is only given if the sample undergoes atomic reconstruction. The shear mode

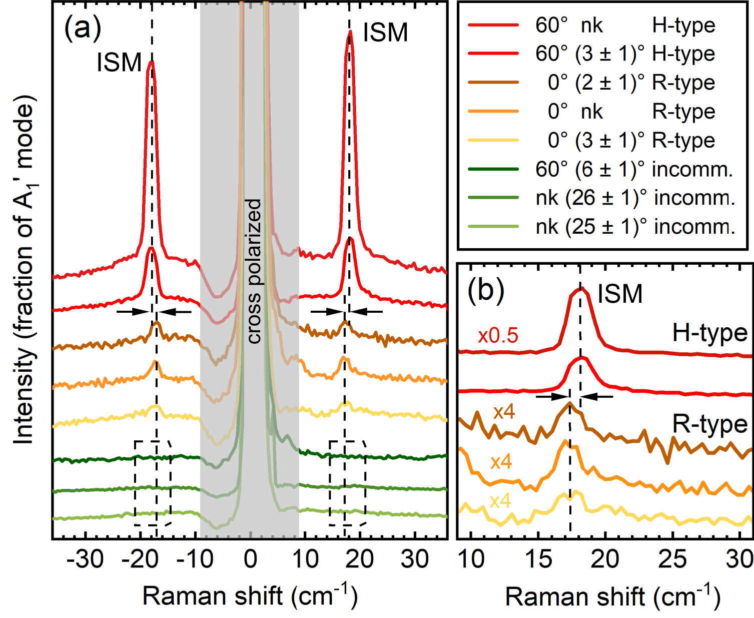

Figure 8.10.: *(a) Comparison of shear modes for $MoSe_2$-WSe_2 heterostructures with different stacking angles, which are listed in the right upper panel. Here, the general orientation is given (H-, R-type or incommensurate), as well as the deviation from ideal H- or R-type. (b) More detailed comparison of shear modes in H-type and R-type. Adapted from [164].*

can therefore not be observed, when a Moiré lattice is formed. The breathing mode on the other hand only needs the van der Waals interaction of neighbouring layers as its restoring force, and appears for every twist angle. The reason it can not be observed in Fig. 8.10 is that this measurement was done using crossed linear polarization, where the breathing mode is not allowed.

In case of Moiré lattices, there is another interesting effect observable in Raman measurements, that is known as Moiré phonons [163, 171]. These are acoustic phonons, that are folded back to the Γ-point of the Brillouin zone by the Moiré supercell. Their energy is therefore directly linked to the twist of the layers. This means, that modelling the phonon dispersion and comparing it to the experimental Raman shifts allows to precisely determine the twist angle on a certain point of the Moiré lattice.

8.4.2. Interlayer excitons

The most prominent feature of TMDC heterostructures is the formation of interlayer excitons [172, 173]. For these complexes, electrons and holes are separated spatially into the different monolayers the heterostructure is made of. This separation of charge carriers is caused by the band alignment that is sketched in Fig. 8.11 (a). Applying the Anderson rule, it was shown theoretically that most combinations of TMDCs (including $MoSe_2$-WSe_2) form a type II band alignment [174, 175]. Hence, when exciting charge carriers optically, electrons from the WSe_2 monolayer relax to the conduction band of $MoSe_2$, whereas holes do the opposite and tunnel to the valence band of WSe_2. The Coulomb interaction between electrons in the $MoSe_2$ conduction band and holes in the WSe_2 valence band then forms the so called interlayer exciton (indicated green in Fig. 8.11 (a)). The PL spectrum for such a sample is shown in Fig. 8.11 (b). The PL peaks of the two monolayers are found at the expected energies, however they are quenched in intensity due to the charge carrier tunnelling process. Below that, at roughly 1.4 eV, a new PL peak emergences, that belongs to the interlayer exciton.

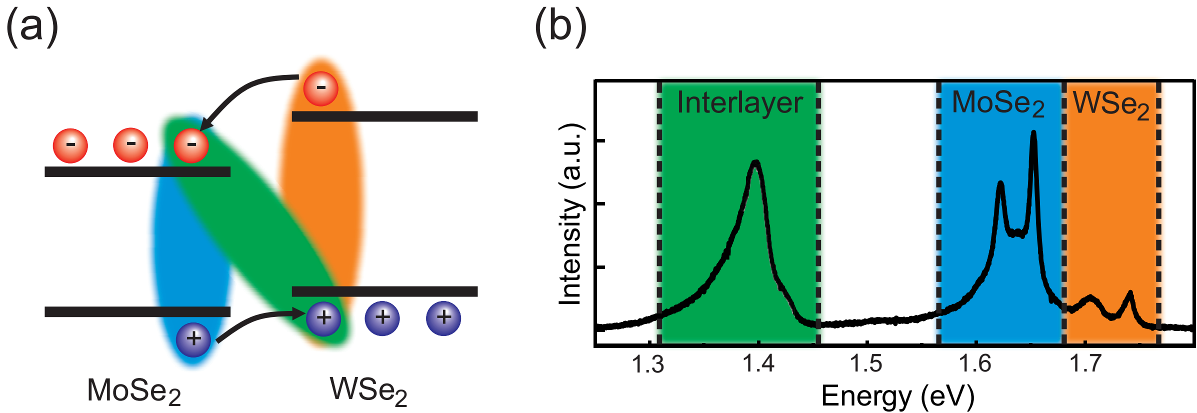

Figure 8.11.: *(a) Type II band alignment for a heterostructure of $MoSe_2$ and WSe_2. Electrons tunnel to the $MoSe_2$ layer and holes the other way around, leading to the formation of an interlayer exciton (green). (b) PL spectrum of a $MoSe_2$-WSe_2 heterostructure at cryogenic temperatures. Below the intralayer PL lines, a new peak emerges that belongs to the interlayer transition. Adapted from [173].*

In order to get a strong optical emission of interlayer excitons, the recombination of electrons and holes has to be momentum-allowed. To achieve this, the K-points of the Brillouin zones of the constituent layers have to lie on top of each other in reciprocal space. The relevant parameter to align the points of the Brillouin zone in reciprocal space is the twist angle of the two layers in real space. For a H-type heterostructure,

the K_+ points of the first layer are aligned with the K_- points of the second layer (and vice versa), whereas the K_+ lies on top of K_+ and K_- on top of K_- for a R-type heterostructure [176, 177]. For other twist angles, also the points in reciprocal space are misaligned, leading to a drastic decrease of interlayer PL [170]. It was shown by Parzefall et al, that the intensity of the interlayer PL shows a step at the critical angle where atomic reconstruction is achieved [163], with the reconstructed structure emitting significantly more PL compared to a Moire lattice.

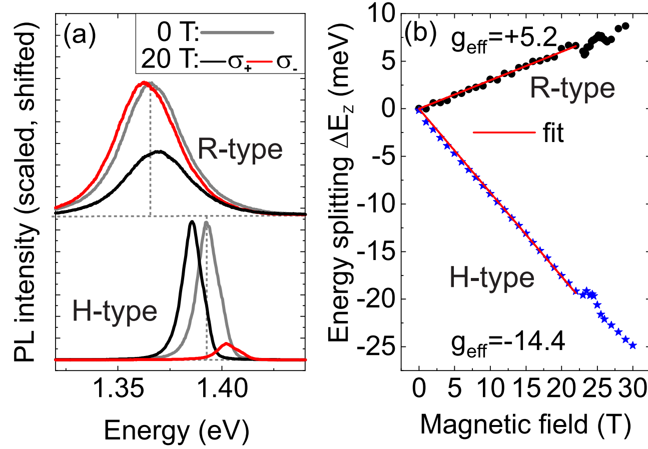

Figure 8.12.: *(a) Interlayer PL of a $MoSe_2$-WSe_2 heterostructure for R- and H-type stacking. For zero magnetic field (grey curve) the PL is broader and at lower energy than for H-type. Circular polarized detection (red and black curves) shows that the Zeeman shift reverses sign for the two stacking types. (b) Extracted effective g-factors from (a). Adapted from [178].*

The difference between H- and R-type stacking is also important when looking at the interlayer PL in external magnetic fields. As the interlayer excitons recombine between inequivalent K-points for H-type stacking but between equivalent K-points for R-type structures, the observed Zeeman shift changes drastically for the two configurations [176, 177]. A measurement visualizing the difference of the two stacking types is shown in Fig. 8.12. In panel (a), the interlayer PL is shown for R-type (upper part) and H-type (lower part) structures, once for zero magnetic field (grey curve), and once the emission of σ_+ (black) and σ_- (red) polarized light for a perpendicular magnetic field of 20 T. Comparing the two stacking configurations, one can see the Zeeman shift is considerably smaller for R-type than for H-type, and also reverses its sign. The extracted effective g-factors are plotted in panel (b), giving a value $g_{eff} = 5.2$ for R-type and $g_{eff} = -14.4$ for H-type.

Furthermore, it can be seen in Fig. 8.12 (a), that already at zero magnetic field the interlayer PL looks different for the two configurations; the R-type gives a broader linewidth and lower energy PL compared to the H-type. Having assigned the different interlayer luminescence characteristics to the stacking type via the observed Zeeman shift, the PL characteristic can now be used as another deciding criteria, which sort of stacking type a heterostructure has got. This procedure was also used to pre-characterize the samples used for the comparison of shear modes in Fig. 8.10.

8.5. Sample preparation

All samples used in the following experimental chapter were made using mechanical exfoliation, that successfully produced monolayers of graphene [10] and other van-der-Waals materials like MoS_2 [11] for the first time. Specifically, we use the PDMS transfer method, that was introduced by Castellanos-Gomez et al. [179], and will be described in the following. The bulk crystals that are the starting material for the process are bought from HG Graphene.

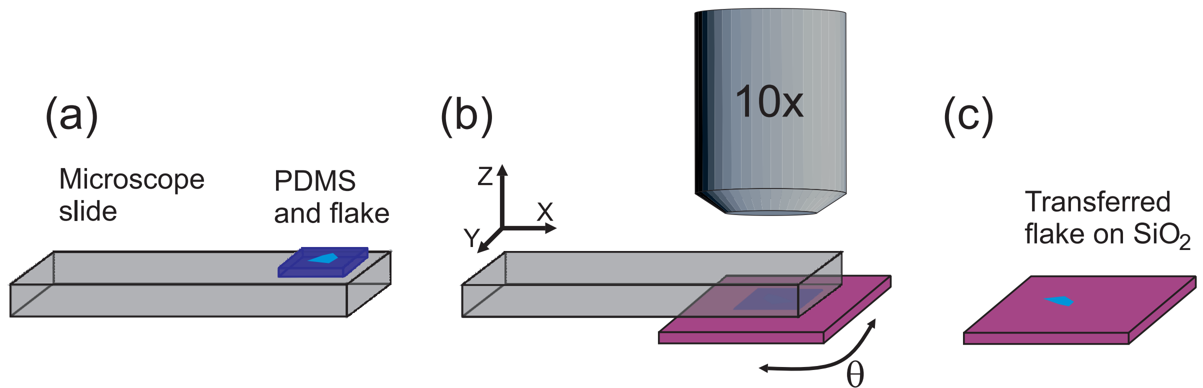

Figure 8.13.: *Most important steps of the PDMS transfer method. (a) Microscope slide with PDMS film, that has an exfoliated TMDC flake on top. (b) Transfer of the flake onto a SiO_2 substrate, using a X-Y-Z stage for the microscope slide and a rotary stage for the substrate. The process is monitored through a 10x microscope objective. (c) SiO_2 substrate containing the transferred TMDC flake.*

In the fist step of the preparation, a nitto tape is used to cleave off some TMDC layers from a bulk crystal. This process is possible due to the weak van der Waals interactions between the individual layers. The nitto tape is then gently pressed on top of a PDMS gel film and removed again, which leaves a much lower number of layers sticking on the

PDMS. This gel film itself is mounted on a microscope slide of glass (as illustrated in Fig. 8.13 (a)), and can therefore be examined under a light microscope setup. Monolayers can be identified this way, by having the lowest optical contrast compared to the gel material.

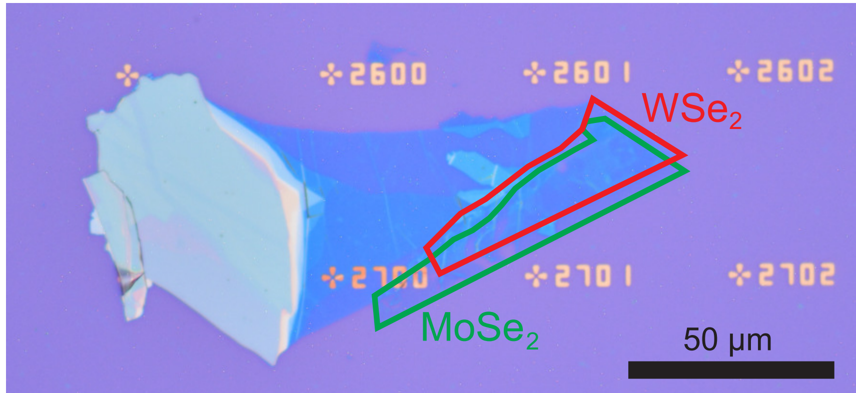

Figure 8.14.: *Light microscope image of the $MoSe_2$-WSe_2 heterostructure MW01. The monolayers were aligned along their longest edges, which indicate crystallographic directions.*

If a monolayer of the required size is identified on the gel film, it is transferred to a silicon substrate with a 285 nm thick SiO_2 layer on top. For this transfer, the microscope slide is mounted up side down in a X-Y-Z stage with micrometer screws, allowing a fine positioning of the slide during the stamping process. The substrate is itself mounted on a rotary stage, which is important for aligning crystallographic axis when fabricating heterostructures. In the next step, the PDMS film is gently put in contact with the substrate, which is monitored through a 10x magnifying microscope objective (see Fig. 8.13 (b)). After the whole flake touches the substrate, the film is removed again extremely slowly. Since PDMS behaves like a solid on short timescales, but like a liquid on longer ones, the flake stays on the silicon substrate, as it is sketched in (c).

For the production of a heterostructure, this process is simply repeated, stamping the second flake on top of the first one. As it is most of the time required to achieve a specific twist angle between the layers, the two flakes are aligned using the rotary stage the substrate is placed on. This is possible, since TMDCs tend to brake along their crystallographic directions during the exfoliation, which means the flakes often show straight edges that can be aligned or anti-aligned. An example is the heterostructure MW01 which is shown in Fig. 8.14. This structure has an R-type stacking and will be used in many of the upcoming measurements. The picture also shows an array of gold

numbers on the substrate, which makes it easier to find the flakes when the sample is mounted into a cryostat.

9. Experimental results on $MoSe_2$-WSe_2 heterostructures

In this chapter, the experimental results on low-temperature resonant Raman measurements of $MoSe_2$-WSe_2 heterostructures are presented. We find a new low-energy Raman peak, that is resonantly enhanced with the $MoSe_2$ trion energy, and is not known so far in the literature to the best of the authors knowledge. In the first two sections, the pre-characterisation of samples and the necessity of using heterostructures instead of monolayers will be discussed, before turning the attention to the new Raman peak and its resonance, temperature and polarization dependence. A possible connection to trion states is discussed, as well as the dependence on the twist angle of the heterostructure. Finally, possible interpretations for this phenomena are proposed.

The samples used in this chapter were pre-characterized by PL, magneto PL, and Raman spectroscopy, to determine if they are H- or R-type stacked, or to measure the exact twist angle in case of Moiré structures. For details about these procedures see [163, 164, 178].

9.1. Non-resonant temperature dependence

The goal of our experiments was to measure the Raman spectra of $MoSe_2$ in extreme resonance with its excitonic transitions at low temperatures. For $MoSe_2$, this is possible using a Ti:Sapphire laser, as it covers the whole energetic range of the optical band gap. Since monolayer $MoSe_2$ is a direct semiconductor, there are however two practical problems arising when performing resonant Raman measurements. The first one is the strong PL, that is stronger by several orders of magnitude than every Raman line and therefore obscures them completely. This problem will be discussed in the next section. Another problem that is addressed in this section, is the the asymmetric broadening of the laser line due to resonance fluorescence, that occurs when the laser energy directly matches an excitonic transition.

Usually, when measuring Raman spectra at room temperature using a set of Bragg filters, the exact spectral position of Raman lines is determined by shifting the spectrum in such a way, that it is symmetric for the Stokes and Antistokes side. At low temperatures, unfortunately the phonon lines vanish at the Antistokes side, since the branches are not occupied any more. In addition to that, we can not easily measure the Stokes and Antistokes side simultaneously using a triple Raman spectrometer any way, as the spectral range is cut off to one side at the laser frequency. The only way to determine the exact phonon positions is then to shift the middle of the laser to exactly $0\,\mathrm{cm}^{-1}$, which is getting problematic for an asymmetrically broadened laser line due to resonance fluorescence. Therefore, a non-resonant, temperature-dependent characterization measurement was done, that later allows to adjust every spectrum according to the position of the $MoSe_2$ A_{1g}-mode.

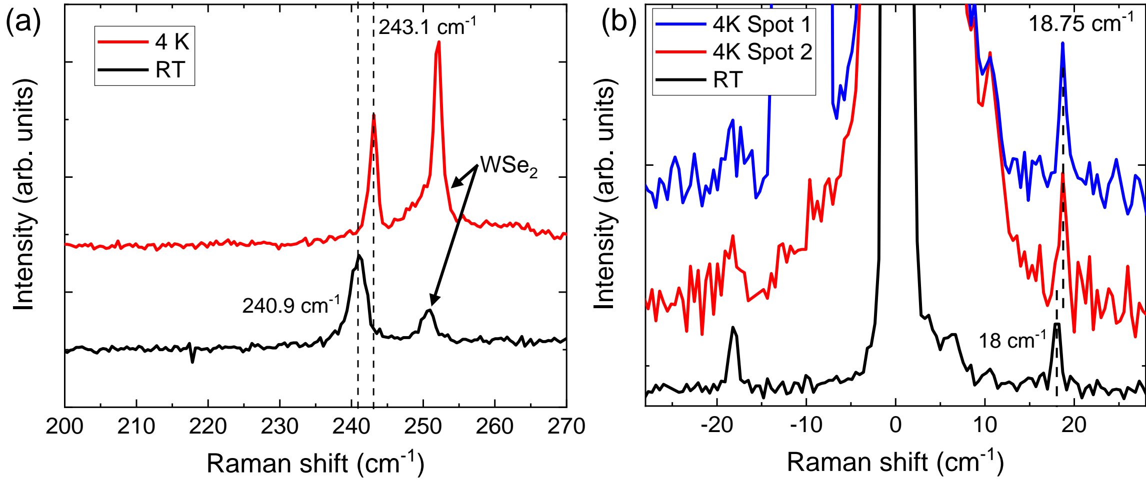

Figure 9.1.: *(a) Comparison of the $MoSe_2$ A_{1g}-mode position on a $MoSe_2$-WSe_2 H-type heterostructure for room temperature and $4\,\mathrm{K}$, measured using a green laser and co-polarized linear polarization. The higher energy peak at $250\,\mathrm{cm}^{-1}$ stems from the A_{1g} and E^1_{2g}-modes of WSe_2 and was not used for characterisation. (b) Comparison of the shear mode on a $MoSe_2$-WSe_2 H-type heterostructure for room temperature and $4\,\mathrm{K}$, measured using a green laser and cross-polarized linear polarization. The shear mode also shifts to higher energy when cooling down the sample, but by less than $1\,\mathrm{cm}^{-1}$.*

Fig. 9.1 (a) shows the result of a Raman measurement done on a H-type $MoSe_2$-WSe_2 heterostructure (MW11), using a green laser of $2.33\,\mathrm{eV}$ energy, a set of Bragg filters for blocking the laser line and a single stage Raman spectrometer. The black curve was taken at room temperature and the red one at nominally $4\,\mathrm{K}$, using co-polarized linear polarization. It is commonly known that phonons shift to slightly higher energies when

cooling down the sample, which is due to the anharmonic atomic binding potential, that leads to a thermal expansion of the crystal lattice [31]. For $MoSe_2$ this effect was already measured, however not for temperatures of 4 K [180], and not for heterostructures. In Fig. 9.1 (a), we therefore determined the exact position of the $MoSe_2$ A_{1g}-mode at room temperature, by comparing Stokes and Antistokes side (not shown), and then measured the temperature dependent shift. As marked in the figure, the mode is found at $240.9\,\mathrm{cm}^{-1}$ for room temperature and at $243.1\,\mathrm{cm}^{-1}$ for 4 K. For R-type structures, the values were slightly different, $241.3\,\mathrm{cm}^{-1}$ for room temperature and $243.4\,\mathrm{cm}^{-1}$ for 4 K. As described, we will use the values for 4 K to norm all of the spectra from now on.

For the interpretation of our results, it will also be important to know the low-temperature position of the interlayer shear mode. To find this mode in the spectrum at 4 K turned out to be quite difficult, which is why it was only possible for our best H-type structure (pi29) and at crossed linear polarizations. This measurement is shown in Fig. 9.1 (b), and was also done using a green laser and a set of Bragg filters. Consistent to the data shown in Fig. 8.10, we find the mode at $18\,\mathrm{cm}^{-1}$ for room temperature. For a temperature of nominally 4 K, we see the mode at $18.75\,\mathrm{cm}^{-1}$, which is a smaller blueshift than for the A_{1g}-mode. As it got difficult to identify the mode in the background noise, two different spots were measured to confirm the data.

9.2. Quenching of intralayer PL

In this section, the solution to obscured Raman lines by PL in case of resonant excitation is presented. It was already mentioned that we use a $MoSe_2$-WSe_2 heterostructure, to make use of the type II band alignment. As the electrons are accumulated in the $MoSe_2$ layer and the holes in the WSe_2 layer, not only interlayer excitons are formed, but also the magnitude of intralayer PL is reduced. The effectiveness of this process is however strongly dependent on the interlayer coupling strength, that is not equal on every point of the sample. We therefore always focus the laser on points that show the best available interlayer exciton PL.

In Fig. 9.2 (a), the PL of a R-type $MoSe_2$-WSe_2 heterostructure at $T = 4\,\mathrm{K}$ is displayed for two different sample spots . These spectra were recorded using a green laser and a single stage spectrometer. The strong feature between 1300 meV and 1400 meV is the luminescence of the interlayer exciton, the two peaks between 1600 meV and 1700 meV trion and A exciton of $MoSe_2$, with the WSe_2 PL lines (that lie at slightly higher energy) just being cut off. The important point of this comparison is the inverse dependency

of the inter and intralayer PL intensity; for spot one, the better interlayer PL strength goes in hand with a much stronger quenching of the intralayer lines compared to spot two. In order to find the best spot for a Raman experiment, we can therefore look for a spot with strong interlayer PL first.

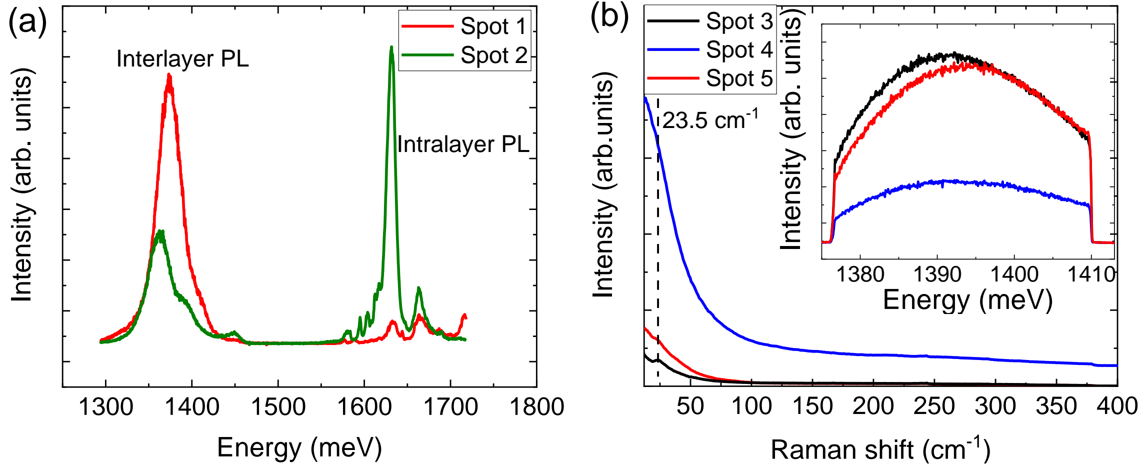

Figure 9.2.: *(a) PL measurement at* $T = 4\,\mathrm{K}$ *on a R-type* $MoSe_2$*-*WSe_2 *heterostructure for two different spots. A stronger interlayer PL indicates a better quenching of the intralayer PL lines. (b) Consequence of different intralayer PL quenching strengths on a Raman measurement, with laser excitation resonant to the trion of* $MoSe_2$*. The respective interlayer PL for the points three to five is shown in the inset. For the point with the best intralayer quenching properties, a Raman peak at* $23.4\,\mathrm{cm}^{-1}$ *can be resolved.*

The consequences of different intralayer PL quenching strengths for resonant Raman measurements are visualized in Fig 9.2 (b). These spectra were taken using the Ti:Sapphire laser and the triple Raman spectrometer, the temperature was nominally $4\,\mathrm{K}$ and linear co-polarized light was used. The laser energy is tuned to about $1.63\,\mathrm{eV}$, which is close to the trion resonance of $MoSe_2$. For each point on the sample shown in the plot, the interlayer PL was recorded and is shown in the inset. The reason this PL is cut off at the sides, is the triple Raman spectrometer. When using the same spectrometer configuration for PL and Raman measurements (which is preferable for correlating Raman and PL spectra of the same sample points), the light travels through all three stages, and the spectral range is cut out at the slit between first and second spectrometer stage. For PL measurements, this leads to a very narrow spectral window, especially for the broad interlayer exciton PL. However, since we are only interested in the maximal PL intensity, this is no problem for us. As the laser energy is in resonance with the trion, a weaker intralayer PL quenching leads to a strong resonance fluores-

cence, that broadens the laser line around $0\,cm^{-1}$. This effect is clearly observed for spot four (blue curve). For the other spots, especially for spot three, it is observed that a stronger interlayer PL reduces the resonance fluorescence, and suddenly a Raman peak is resolved at $23.4\,cm^{-1}$. The properties of this peak will be discussed in the following sections.

9.3. Excitation energy dependent spectra

After going through the necessary steps to perform a Raman measurement in extreme resonance to the $MoSe_2$ transitions at low temperatures, we will now discuss the results. Fig. 9.3 (a) is a series of Raman spectra measured on a R-type heterostructure (MW01) at nominally 4 K for different laser excitation energies between 1722 meV and 1614 meV, as indicated at the right side of the plot. The laser was linear co-polarized and the excitation power 500 µW with an exposure time of 60 s per spectrum.

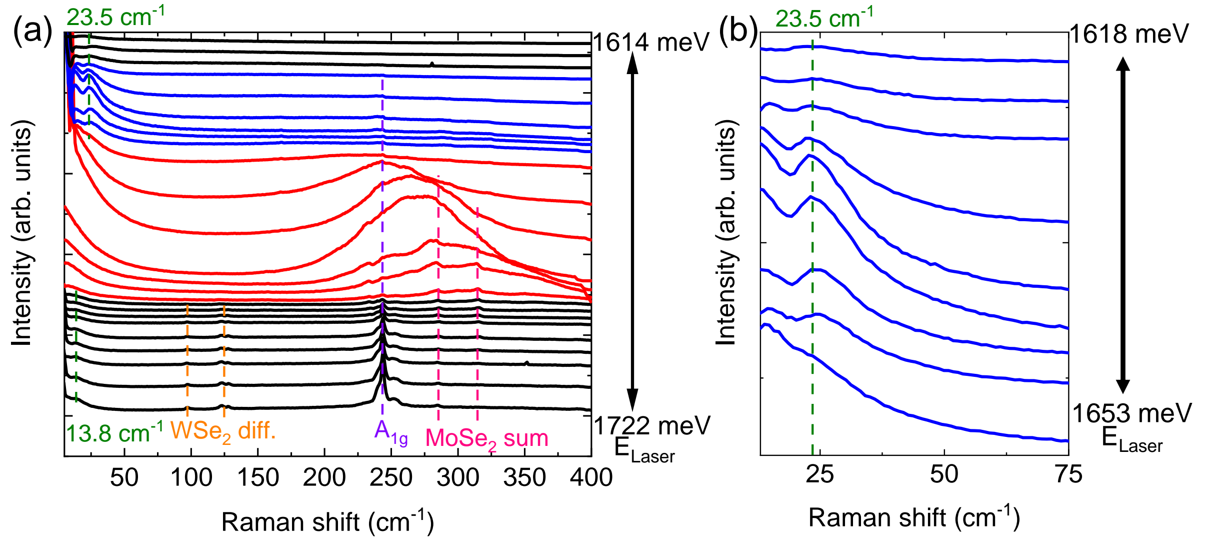

Figure 9.3.: *(a) Raman spectra of a R-type $MoSe_2$-WSe_2 heterostructure at $T = 4\,K$ for different laser excitation energies between 1722 meV and 1614 meV. Spectra in resonance with the $MoSe_2$ A exciton are drawn red, those in resonance with the $MoSe_2$ trion blue. (b) Spectra in resonance with the $MoSe_2$ trion of the same measurement as (a), highlighting the appearance of a low energy excitation (LEEX) for this laser energies only.*

We will start the discussion at the high energy side of excitation energies. The highest energy of 1722 meV lies in between the neutral and charged exciton of WSe_2. Note that

due to the charge carrier separation in the heterostructure, we expect the WSe_2 trion to be positively charged. This positive trion should be located just above 1700 meV, as known from gate dependent PL measurements [130, 131], see also Fig. 8.5 (b). In other words, with decreasing excitation energy, we first go into resonance with the WSe_2 positive trion, followed by the $MoSe_2$ neutral exciton (marked by the red graphs) and the $MoSe_2$ negative trion (blue graphs).

The most prominent Raman peak for high excitation energies is the A_{1g}-mode of $MoSe_2$. The fact, that this mode is observed with its highest intensity for energies above the neutral exciton of $MoSe_2$, reflects an outgoing resonance for this phonon. For the same reason, the A_{1g}-mode of WSe_2 is only observed very weakly at $252\,\mathrm{cm}^{-1}$; since the laser energy is already below the neutral exciton of WSe_2 and the resonance type is outgoing, it does not appear at high intensity here. The peaks at higher spectral energies than the two A_{1g}-modes most likely stem from sum processes, commonly observed in this spectral region [150, 181] and are not of further interest here. Below the A_{1g}-modes, two weak features can be observed at $97\,\mathrm{cm}^{-1}$ and $122\,\mathrm{cm}^{-1}$. These peaks stem from the WSe_2 monolayer and were previously assigned to difference processes; $E_{2g}^{1}\,(M)^{TO_2} - LA\,(M)$ and $E_{2g}^{1}\,(M)^{LO_2} - LA\,(M)$, respectively [182]. The fact that they are still visible at $T = 4\,\mathrm{K}$, where the optical phonon branches should not be occupied, rises the question whether they should rather be interpreted as defect activated scattering of acoustic phonons. Finally, at $13.8\,\mathrm{cm}^{-1}$, a very weak peak is detected for excitation energies in the vicinity of the WSe_2 trion, which will be included into the interpretation of our results later on.

Going to lower laser energies, resonant excitation with the neutral exciton of $MoSe_2$ is reached. The spectra in this energetic region are marked red. Here, two effects can be observed; first of all, a strong resonance fluorescence towards the laser line, which is most likely caused by acoustic phonon scattering. And second, a broad peak appears in the spectrum between $250\,\mathrm{cm}^{-1}$ and $300\,\mathrm{cm}^{-1}$, which we assign to the PL of the $MoSe_2$ trion. When the laser hits the neutral exciton, more trions are formed through scattering of phonons, since the energy of the A_{1g}-mode and the spacing between neutral and charged excitons in $MoSe_2$ roughly match. This leads to an effective scattering mechanism via this phonon mode, explaining why the trion PL is only strongly observed in this range of excitation energies.

For excitation energies in the range of the $MoSe_2$ trion, there is again a resonance fluorescence measurable, together with the appearance of a low-energy excitation at $23.5\,\mathrm{cm}^{-1}$ (called LEEX from now on). This feature is clearly identified as a Raman

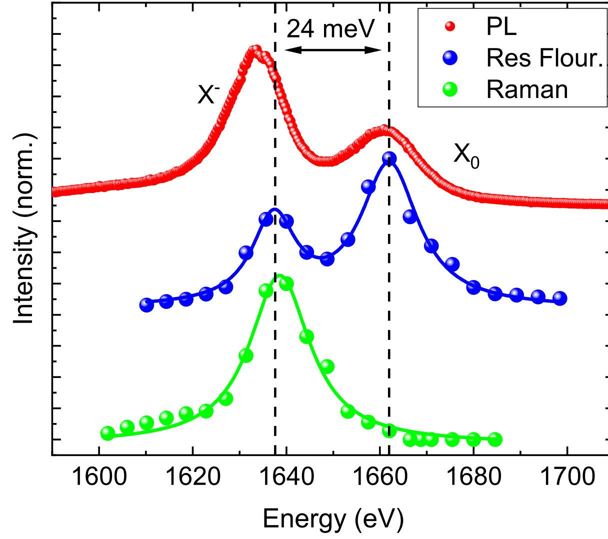

Figure 9.4.: *Comparison of the LEEX intensity with respect to laser excitation energy (green), to the resonance fluorescence extracted from the same measurement (blue) and a low-temperature PL spectra of monolayer $MoSe_2$ (red). All graphs are normed.*

peak due to its constant Raman shift for changing excitation energy. Fig. 9.3 (b) is an excerpt of the same measurement series, highlighting the appearance of the LEEX peak for a small range of excitation energies only. In the following, we will analyse the resonance behaviour of this peak in more detail.

Fig. 9.4 compares the LEEX intensity with respect to excitation energy (green) to the resonance fluorescence extracted from Fig. 9.3 (a) (blue) and a low-temperature PL measurement of a $MoSe_2$ monolayer (red). The intensity of the LEEX was extracted by plotting its count rate with respect to the background signal, and fitted with a Lorentzian line. The fluorescence corresponds to the count rate in the Raman spectrum at $15\,\mathrm{cm}^{-1}$, and is fitted by the sum of two Lorentzian curves. Comparing these different measurements, it is obvious that the neutral exciton peak of the fluorescence matches with that of the PL measurement, while a slightly smaller spacing between neutral and charged exciton is found in fluorescence than for the PL. We think that this is due to the fact, that in the fluorescence, which is a quasi instantaneous process, the energy of free trions is measured, while the PL involves relaxation of excitons to their lowest possible states, and therefore shows localized trions at lower energy. The energetic distance between the neutral A exciton and free trions would thus be 24 meV. The ratio of trion

to neutral exciton intensity in the fluorescence is 0.69, which we can assign to a charge-carrier density of $n \approx 6 \cdot 10^{11}\,\mathrm{cm}^{-1}$ by comparison to theoretical models [183]. For the LEEX, the maximum in intensity correlates very nicely with the free trion peak of the fluorescence. We therefore conclude that it is resonantly enhanced with the trion, but not with the neutral exciton. We can exclude the possibility of a resonant enhancement with biexcitons (which have been found between neutral and charged exciton in $MoSe_2$ by four-wave-mixing experiments [184]), since there is no super-linear behaviour of the fluorescence for different excitation powers, which will be shown later.

9.4. Temperature dependence of resonance effects

To further confirm our assumption that the LEEX peak is resonantly enhanced with the trion of $MoSe_2$, we ran a couple of excitation-energy dependent series for different sample temperatures. For temperatures higher than 4 K, the trion PL shifts to lower energies and decreases in intensity, until it vanishes completely in the range between $150 - 200$ K [129]. If the LEEX is resonant to the trion, its resonance should show the same dependency on temperature.

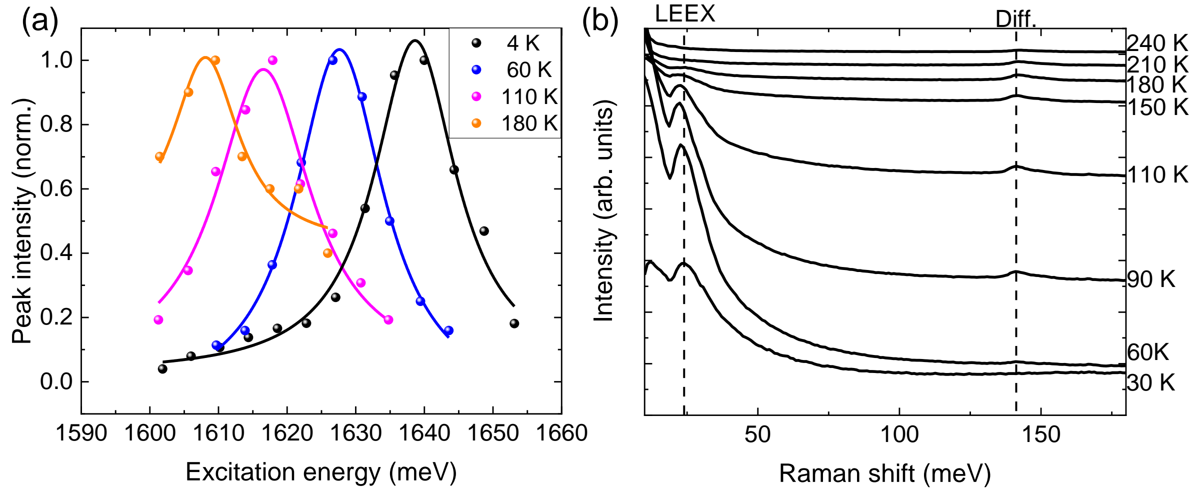

Figure 9.5.: *(a) Resonance curves for the LEEX peak for different temperatures. The points are the count rate relative to the background signal, the solid lines Lorentzian fits. (b) Temperature-dependent spectra of the LEEX, measured at the maximum position on the resonance curve for each temperature. The LEEX decreases in intensity and moves to lower Raman shift for rising temperature.*

Fig. 9.5 (a) shows a selection of resonance curves for the LEEX peak, that were

extracted from excitation-energy dependent series at different temperatures. All other conditions (sample, power and polarization) are the same as for Fig. 9.3. For better clarity, only the results for every second temperature measured are plotted here. The data points have been fitted using Lorentzian curves. As can be seen, the maximum of the LEEX resonance indeed shifts to lower energies when increasing the temperature. The maximum intensity for the highest temperature of 180 K furthermore agrees well with the spectral position of the trion that is found in PL [129]. The reason the number of data points decreases for increasing temperature is due to the fact, that also the LEEX intensity decreases, and therefore is observable for fewer excitation energies the higher the temperature gets. This behaviour is shown in Fig. Temp2D (b).

In Fig. 9.5 (b), the Raman spectrum is plotted for every temperature measured above 4 K, using the laser energy where the LEEX peak shows its highest intensity for the respective temperature. In other words, the excitation energy used for the spectra in Fig 9.5 (b) decreases with increasing temperature, following the resonance maxima shift from Fig. 9.5 (a). First of all, it is obvious that the LEEX peak gets weaker for higher temperatures, and vanishes from sight for about $T \approx 200\,\mathrm{K}$. Also the resonance fluorescence associated with the trion decreases, indicating that the formation of trions gets unfavourable at a certain point. Furthermore, a red shift of the LEEX is detected, which is especially prominent when comparing the spectra for 30 K and 110 K; here, the LEEX is already moved to a lower shift by about $2\,\mathrm{cm}^{-1}$.

Another interesting effect can be observed at $141\,\mathrm{cm}^{-1}$. Here, a peak appears for higher temperatures, that was not visible for 4 K and 30 K. This peak is known in literature to be a difference process of $E^1_{2g}(M) - LA(M)$ [181]. To measure this peak in the spectrum, the E^1_{2g} branch has to be occupied, which is not the case for low temperatures, leading to its disappearance. In contrast to the low-energy peaks from WSe_2, that were also assigned as difference processes before, we can confirm that the interpretation in literature is correct for this peak. It also shows us that all heating functions of the cryostat were working properly, and we can trust the nominal increase of sample temperature. Lastly, the opposite temperature behaviour of the LEEX peak and this difference process proofs, that the LEEX peak is most definitely not a difference process of phonons. Also the possibility of a defect activated acoustic phonon can be ruled out, as these peaks seem to survive for all sample temperatures, as seen before for WSe_2. The observed resonance and temperature dependency leaves us with three possible scenarios: A pure electronic scattering event, involving a fine structure of the trion, a first order Raman peak that is resonantly enhanced with the trion only, or a

interaction process of the electronic system with a phonon mode, that also needs a stable trion to take place.

9.5. Power and polarization behaviour

Before discussing the different possibilities to interpret the LEEX peak, a short look should be taken on the power and polarization dependence. Fig. 9.6 (a) displays the LEEX peak at $T = 4\,\mathrm{K}$, 1631 meV laser energy and linear co-polarization for different excitation powers. Apart from the LEEX intensity increasing with excitation power, no further effect (for example change of the Raman shift) can be observed. Hence, the peak shows the power dependence that is expected for any sort of first order Raman lines.

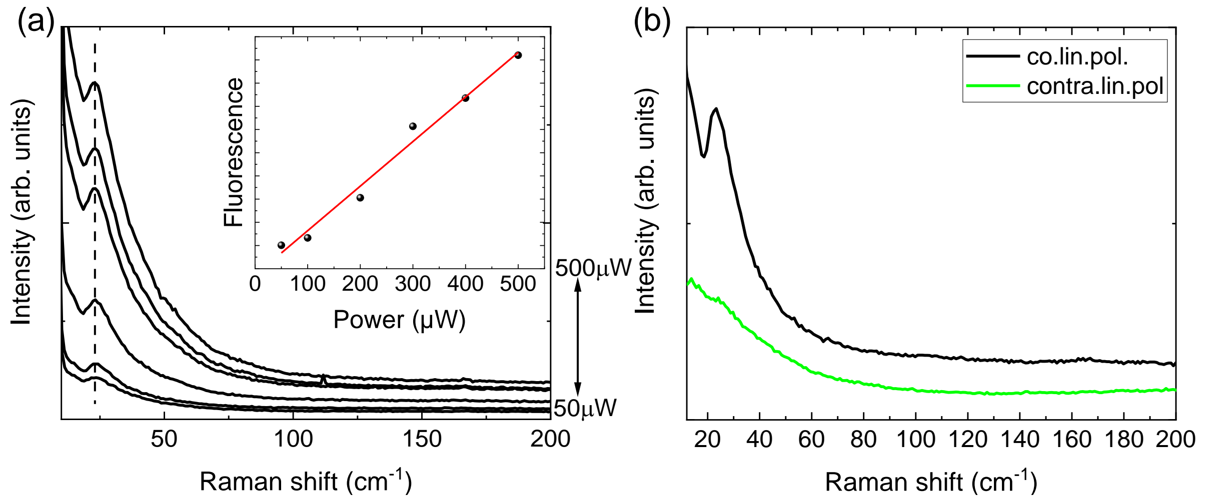

Figure 9.6.: *(a) Response of the LEEX to different excitation powers. The inset is the power-dependent intensity of the resonance fluorescence extracted from this measurement. (b) Behaviour of the LEEX for different linear polarization configurations, once for co and once for crossed.*

The small inset of Fig. 9.6 (a) is the intensity of the resonance fluorescence extracted from the same measurement. As before, the values were read out by taking the intensity close to the laser line with respect to the background intensity. The data points can be fitted linearly, showing that there is indeed no super-linear dependence of the fluorescence on power, excluding biexcitons as a possible intermediate states for the Raman resonance.

Fig. 9.6 (b) compares the LEEX peak for different polarization configurations, namely for linear co and cross polarization. The peak is strongly suppressed in case of cross polarization, and therefore shows a similar behaviour as the A_{1g} or the layer breathing

mode. Hence, for all following spectra showing this peak, linear co-polarized light will be used.

9.6. Possible connection to trion states

When discussing the reason for the temperature dependency of the LEEX peak, the possibility of having a pure electronic scattering event involving a fine structure of the trion was brought up. These trion states, between scattering could take place, could then only be a singlet and a triplet trion, as introduced in the theory chapter. There, singlet and triplet trions were shown and explained for tungsten based TMDCs, where the lowest K-point transition involves the higher lying conduction band. For $MoSe_2$, this situation is different, since the A exciton transition involves the lower conduction band, and the conduction band splitting is $\Delta_{CB} = -22\,\mathrm{meV}$ [113]. Hence, it is not expected that the doping electron for the trion sits in the upper conduction band. A triplet trion in $MoSe_2$ would therefore have to have both electrons in the same valley and the same band, which is predicted to be impossible due to Pauli blocking [183]. Recently, Klein et al. found traces of triplet trions in MoS_2 [185]. This was interpreted in terms of the small conduction band splitting in this material, that leads to a dark A exciton ground state when including electron-hole exchange interaction. For $MoSe_2$ however, this situation is not applicable. To the best of the authors knowledge, nobody has ever found traces of triplet trions in $MoSe_2$. Still, there is a chance that the triplet trion could serve as an intermediate state in Raman scattering, since in a quasi instantaneous process this quasiparticle may not have to be stable. We shall therefore take the consideration of scattering between trion states into account, and suggest a possible process in the following section.

9.6.1. Proposed scattering mechanism

Fig. 9.7 illustrates the scattering mechanism we suggest for participating singlet and triplet trion states. The ground state in this mechanism is a singlet (or intervalley) trion, which is drawn on the right side of the first box (a). Here, both electrons occupy the lower conduction band, but in different valleys, forming a spin singlet. We expect these trions to be present in the sample, because of the constant laser radiation in resonance with the trion energy. Due to the laser excitation, also the energetically higher lying triplet trion could be formed, as shown on the left side of (a). As already mentioned, this

triplet trion would require to have both electrons in the same valley and band, which is a consequence of the conduction band ordering in $MoSe_2$. The formation of this triplet trion would then be considered as the first intermediate state in the scattering event.

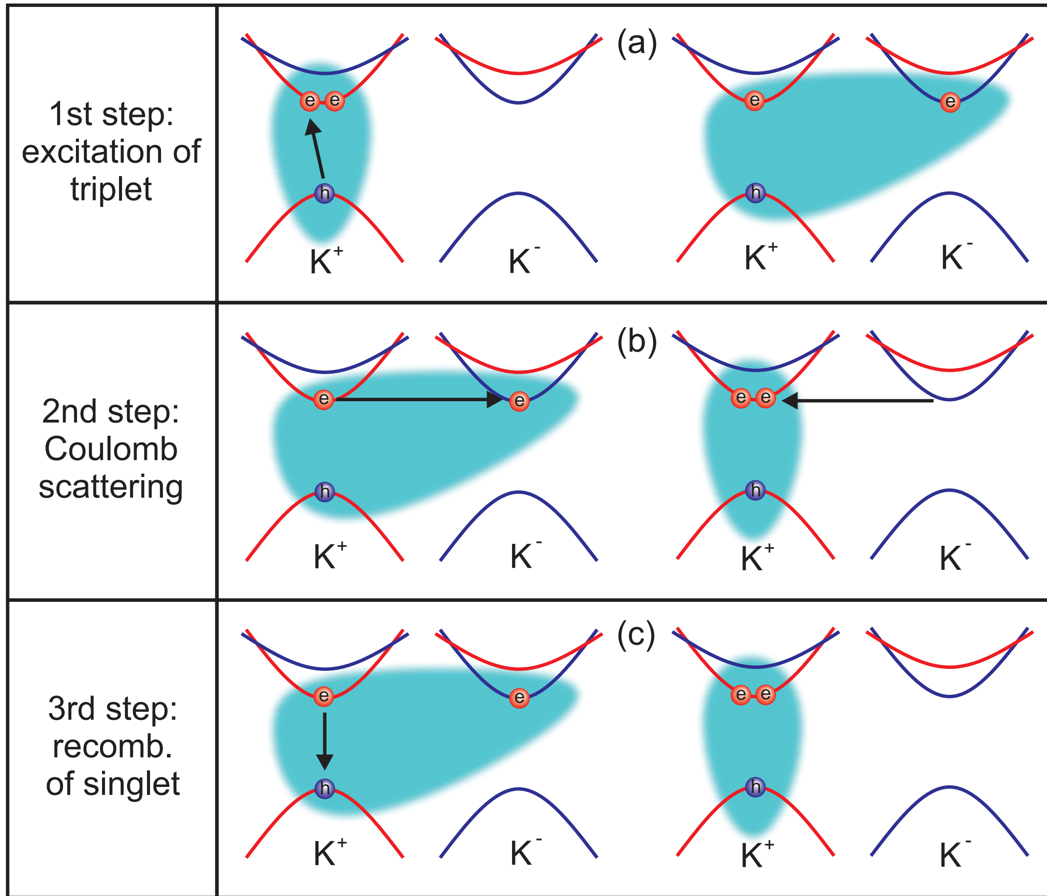

Figure 9.7.: *Scattering mechanism involving a fine structure of the trion. (a) First step: Excitation of a triplet trion (left), in addition to the already present singlet trion (right) (b) Second step: Trions exchange energy and momentum by Coulomb scattering (c) Third step: Recombination of the singlet trion (left), leaving a triplet trion in the crystal (right)*

In the second step of the scattering mechanism, the laser excited triplet trion would scatter of the already present singlet trion via Coulomb scattering. In this process, the trions created in step one exchange energy and momentum, which means the laser excited triplet trion becomes the energetically lower singlet trion and vice versa. In the third step (c), this newly formed singlet trion would then recombine, emitting a photon that is lower in energy by the singlet/triplet splitting than the indecent photon, and leaving a triplet trion in the crystal. The singlet trion that recombines is therefore the

second intermediate state of the process. Since both of these intermediate states are real, this scattering mechanism would be doubly resonant.

After the recombination of the singlet trion, a triplet trion stays in the sample, which is the final state of this scattering event. Hence, a singlet trion (ground state) is converted into a triplet trion (final sate), with the energy difference of indecent and emitted photon revealing the singlet/triplet splitting in $MoSe_2$. This energy would then be $23.5\,\mathrm{cm}^{-1} \equiv 2.91\,\mathrm{meV}$. We will test this hypotheses in the following section by measuring the LEEX peak under external magnetic fields.

9.6.2. External magnetic fields

If the assumption of scattering between different trion states is correct, we should see an effect on the LEEX peak when applying external magnetic fields to the sample. We performed this experiment using the Microstat MO cryostat together with the Attocube positioning system, as described in the methods part. This cryostat is built into a different setup, however, the laser and spectrometer stay the same with all other optical components being equivalent to the standard measuring setup.

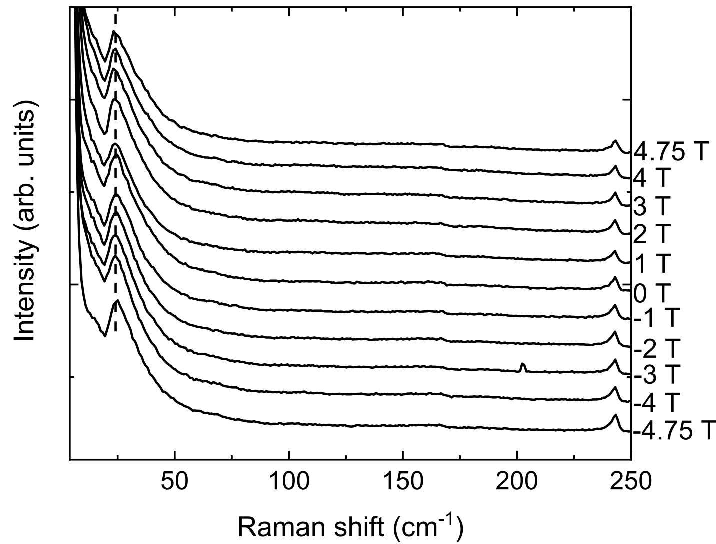

Figure 9.8.: *Spectra of the LEEX peak for external magnetic fields between* $\pm 4.75\,\mathrm{T}$. *No change in any of the LEEX properties can be observed.*

Since the electrons in $MoSe_2$ occupy opposite spin states in case of the singlet trion,

but the same spin state for the triplet trion, we would expect an perpendicular external magnetic field to strongly influence the size of the singlet/triplet splitting. Fig. 9.8 shows an experiment, where the B-field was varied between ± 4.75 T when measuring the LEEX peak with the optimal excitation energy of 1631 meV, using linear co-polarized light. Obviously, there is no change in any of the LEEX properties, such as peak position, linewidth or intensity. For linear polarization, when excitation happens in both valleys at the same time, the magnetic field should increase the singlet/triplet splitting in one valley and decrease it in the other, which should then lead to a broadening of the peak. Also, depending on the sign of the B-field and the chosen valley, forming trions in one valley should become unfavourable compared to the other (see Fig. 8.6), leading to a asymmetric line shape. The fact that we see none of those effects when applying external magnetic fields points strongly towards the assumption, that the LEEX peak is not a scattering event between different trion states.

In the following section, we will investigate the dependency of the LEEX peak on the twist angle of the heterostructure. In contrast to the magnetic field, it will show that the LEEX peak is strongly influenced by this property. This further supports the point of view, that the trion fine structure does not play a part in the scattering process of this peak, since an interpretation in terms of trion states would be a pure intralayer effect.

9.7. Twist angle dependence

So far, we did not take into account the possibility, that the LEEX excitation is in fact an interlayer effect that arises due to the $MoSe_2$-WSe_2 heterostructure, and is therefore not caused by the $MoSe_2$ layer alone. Hence, we will compare different twist angles between the $MoSe_2$ and WSe_2 layers in this section. At first, misaligned heterostructures that form a Moiré lattice will be considered. Next, the question whether atomic reconstruction plays a role will be addressed, before finally comparing H- and R-type structures.

9.7.1. Misaligned heterostructures

In Fig. 9.9, the result of an excitation-energy dependent measurement on a Moiré structure (Pi40) with a twist angle of 15° is plotted. This twist angle was characterized by modelling the backfolded acoustic phonon branches (known as Moiré phonons), which was part of the publication [163].

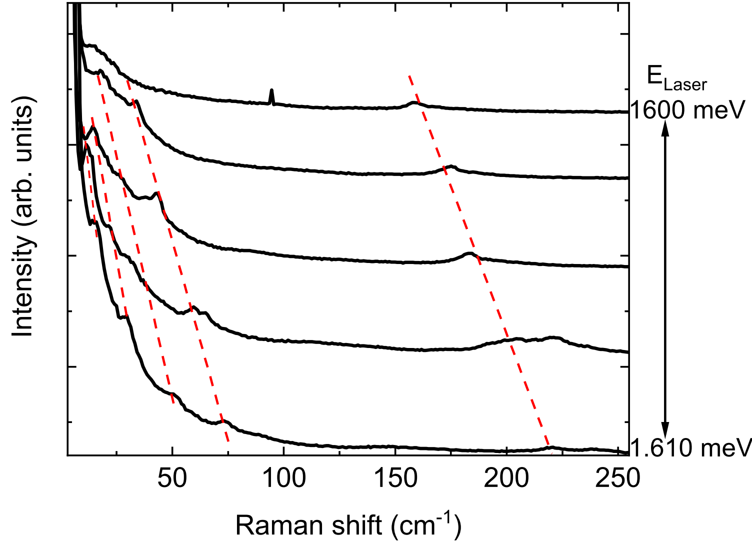

Figure 9.9.: *Excitation-energy dependent series on a heterostructure with a twist angle of $\theta = 15°$. The red dotted lines mark peaks that sit at a constant absolute energy and are thus identified as PL features. The LEEX peak could not be found.*

From the indicated excitation energies at the right side of the plot it follows, that the trion was found at slightly lower energy than for the heterostructures shown so far. This was regularly observed for misaligned structures, the exact reason is however unknown. Nevertheless, hitting the trion resonance again leads to a strong resonance fluorescence towards the laser line. The rest of the spectra for this heterostructure differ strongly from what was measured previously: Here, a number of peaks can be observed (marked by the red dotted lines), that do not show a constant Raman shift with respect to different excitation energies. From that it follows, that these peaks are in fact not Raman peaks, but PL features sitting at a constant absolute energy. This behaviour was found to be typical in this laser energy range for Moiré structures, but was never seen on reconstructed heterostructures. Thus, it seems that these PL features are linked to the Moiré potential in some way. Comparing the energetic distances between these peaks, it indeed seemed to be the case that the spacing correlates inversely with the Moiré period. The LEEX excitation was never found on a Moiré structure, although several different samples were tested. It did not seem as if a worse intralayer PL quenching is responsible for this circumstance. In the following, we will therefore have a closer look on the influence of atomic reconstruction on the appearance of the LEEX peak.

9.7.2. Correlation with atomic reconstruction

To test the influence of atomic reconstruction on the LEEX peak, we will use a sample (HS01) that shows reconstructed areas as well as Moiré areas on the same heterostructure, caused by a stacking angle that is right at the edge of these two regimes. The reconstructed areas are of the H-type, as shown by Nagler et al. using magneto PL experiments [177]. Between these H-type areas, also Moiré areas are found, and their twist angles were characterized by Parzefall et al. according to the spectral position of Moiré phonons [163]. The result of this characterization is shown in Fig. 9.10 (b). Here, golden hexagons indicate areas of the sample, that show the shear mode and are thus recognized as reconstructed. The green circles stand for Moiré areas, giving the exact twist angle at the respective point of the heterostructure.

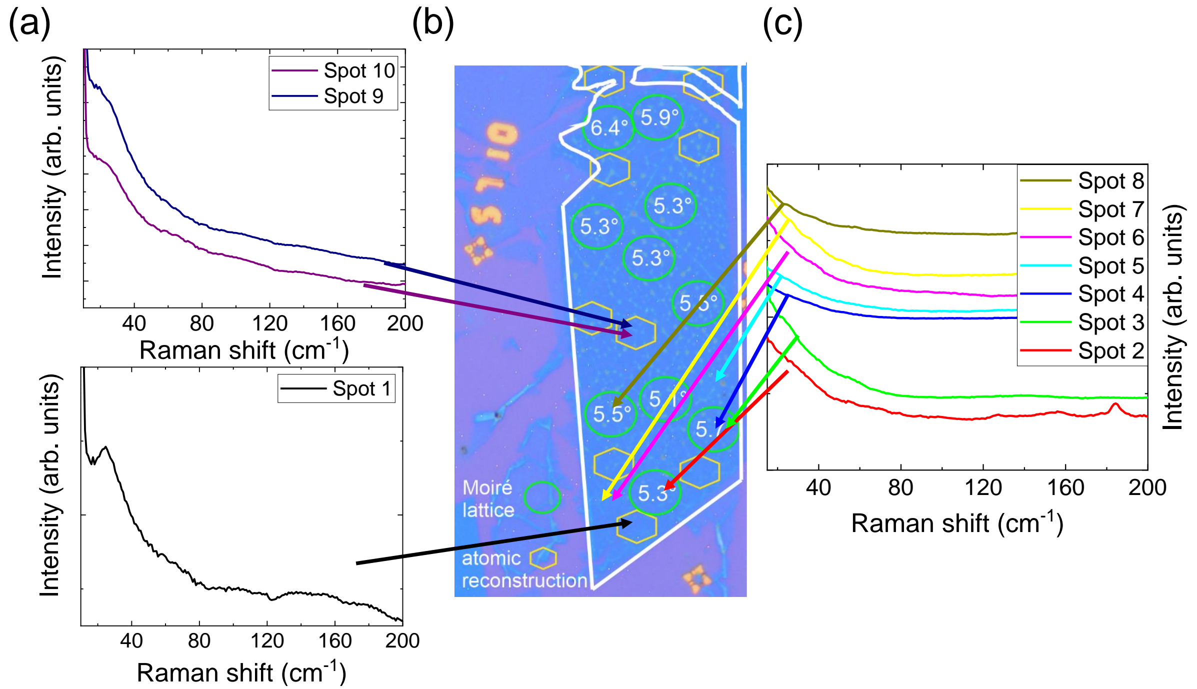

Figure 9.10.: *(b) Microscope picture of the HS01 heterostructure, which has a stacking angle at the edge of the Moiré and reconstruction regimes, and therefore shows both depending on the exact position. Golden hexagons mark areas where atomic reconstruction is present, while green circles indicate Moiré areas and give the stacking angle, measured by Moiré phonons. Picture taken from [163]. (a) Raman spectra in resonance with the $MoSe_2$ trion taken on reconstructed areas of the sample, which are indicated by arrows. (c) Same as (a), but measured on Moiré areas of the sample, again indicated by arrows.*

Left to the picture of the sample in part (a), spectra measured on three different

reconstructed spots are shown, that were all taken at the LEEX resonance energy and the usual power and polarization. The LEEX peak is best observed for spot 1 (lower graph), that was taken at the point of the sample that also shows the highest interlayer exciton PL intensity, and therefore the best intralayer PL quenching. The spots 9 and 10 are on a different reconstructed area, with slightly worse intralayer PL quenching. The LEEX peak is still visible in the the resonance fluorescence towards the laser.

On the right side of the sample picture (c), several measurements taken on Moiré areas are displayed. Also these are taken at the trion resonance energy, which is apparent by the fluorescence towards the laser. However, none of these spectra show the LEEX excitation, even as the quenching of intralayer PL is sufficiently good. Taking this together with the observation that the LEEX peak could not be found on any Moiré lattice with larger twist angle, it has to be concluded that atomic reconstruction is a necessity for appearance of this Peak. Also, it can be concluded at this point, that the LEEX is an interlayer effect, that involves both layers of the heterostructure. The dependence on the twist angle is furthermore similar to that of the layer shear mode at room temperature, which also only appears for reconstructed samples. In addition to that, the shear mode shows a different Raman shift for H- and R-type samples. We will therefore compare the LEEX peak for these two configurations in the following.

9.7.3. H- and R-type comparison

Fig 9.11 (a) compares the LEEX excitation in resonance to the $MoSe_2$ trion in four different samples, two of them H- and two of them R-type. The number of the sample is given in the legend, with the sample MW11 appearing twice, as it has both H- and R-type areas. Dotted lines mark the highest intensity of the LEEX peak for the H- and R-type samples. Unfortunately, as this peak lies in the increasing fluorescence towards the laser, using fit functions does not lead to a more precise assignment of the Raman shift than simply using the point of the highest count rate. Nevertheless, it seems that the LEEX peak shows up at slightly larger Raman shift for H- type structures than for R-type structures, with the difference just below $1\,\mathrm{cm}^{-1}$. The exact same behaviour was found for the shear mode at room temperature [164].

When presenting the excitation-energy dependent Raman spectra in Fig. 9.3 (a), it was stated that also in resonance to the WSe_2 trion a low energy peak appeared, which was located at $13.8\,\mathrm{cm}^{-1}$ on the MW01 sample. This feature had a much lower count rate than the LEEX peak for the $MoSe_2$ resonance, which made it more difficult to investigate it in the same way as done for the LEEX peak. Nevertheless, it was possible

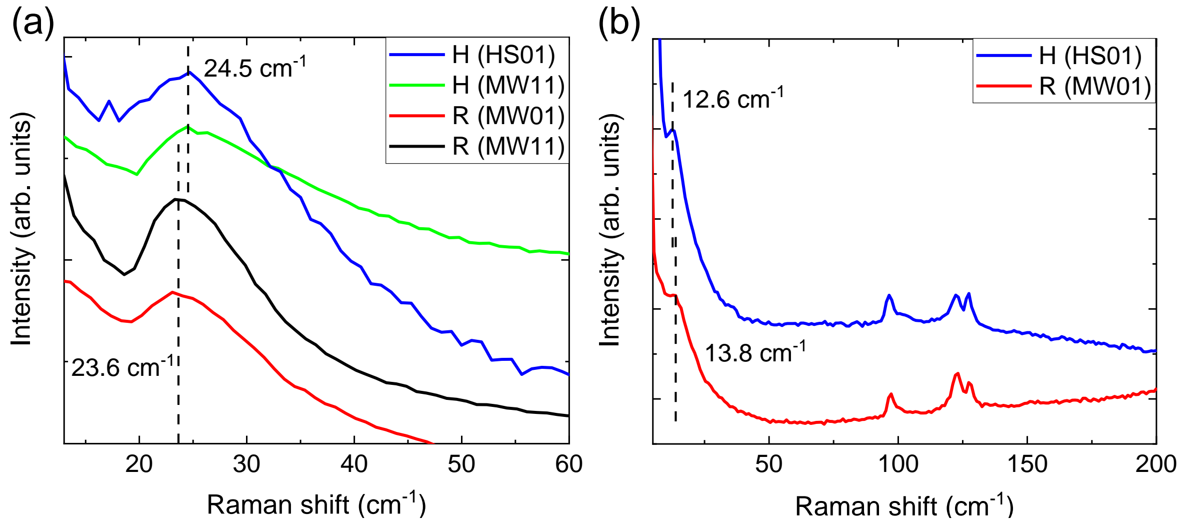

Figure 9.11.: *(a) Comparison of the LEEX peak in resonance to the $MoSe_2$ trion for H- and R-type heterostructures. The peak is found at slightly lower Raman shift for the R-type. (b) Low energy peak found in resonance with the WSe_2 trion for an H- and R-type structure. This peak is found at slightly lower Raman shift for the H-type.*

to find this peak also on the H-type area of the structure HS01. The comparison for H- and R-type structures for the WSe_2 resonant peak is shown in Fig. 9.11 (b). Again, there is a difference just below $1\,\mathrm{cm}^{-1}$ for the two configurations, however with the H-type showing the lower Raman shift for this peak. Unfortunately, we do not have a profound interpretation for this phenomena, which will be evaluated in more detail in the next section.

9.8. Possible interpretations

In this final section of the experimental part, we are going to take closer look on the possible interpretations for the LEEX peak, and discuss which of them are appropriate or not.

It was already argued, that it is very unlikely that the fine structure of the trion itself plays a role in the scattering process. Apart from external magnetic fields showing no visible effect on the LEEX peak, also the strong dependence on the heterostructure twist angle excludes a pure electronic mechanism of trion states. As such a process should be confined to the $MoSe_2$ layer, we would not expect it to vanish for Moiré structures, as long as the intralayer PL quenching is still good enough in order to observe peaks in the

fluorescence. We will therefore not consider this interpretation any further.

Excluding trion states itself from the interpretation, a phonon related process must be responsible for the LEEX peak. Low-energy phonon peaks are often caused by difference processes, where one phonon is created and one annihilated. These processes are however usually not observed at low temperatures, as the phonon that is annihilated has to be present in the material before the scattering. This was observed for the $MoSe_2$ $E^1_{2g}(M) - LA(M)$ peak, that vanishes completely from the spectrum for $T = 4\,\mathrm{K}$. The complete opposite temperature dependency of the LEEX peak therefore excludes difference processes as an interpretation.

We do not believe either, that a defect activated acoustic phonon scattering is responsible for the effect. First of all, phonon peaks that are most probably defect induced were found in WSe_2 at $97\,\mathrm{cm}^{-1}$ and $122\,\mathrm{cm}^{-1}$. These two peaks were previously assigned to difference processes, but survived in the spectrum for nominally $4\,\mathrm{K}$ temperature. Even though the actual sample temperature might have been slightly higher, the absence of the $MoSe_2$ difference peaks in the same measurements shows that the interpretation as difference peaks is not adequate for these WSe_2 peaks. Since those peaks are found in the spectrum for every temperature in contrast to the LEEX peak, defect activated scattering does not seem to be appropriate as an interpretation either. Moreover, a defect activated peak in the $MoSe_2$ layer should not depend on the twist angle of the heterostructure as the LEEX peak does.

In the low-energy region of the Raman spectrum, the only first order Raman modes for a layer number of two, are the layer shear and breathing modes. Both of them can be excluded for interpretation due to the scattering energy of the LEEX and its temperature dependency: For non-resonant excitation, we measured the shear mode in H-type structures at $18\,\mathrm{cm}^{-1}$ for room temperature and at $18.75\,\mathrm{cm}^{-1}$ for $T = 4\,\mathrm{K}$. The Raman shift of the LEEX for H-type structures of $24.6\,\mathrm{cm}^{-1}$ at $T = 4\,\mathrm{K}$ does therefore not fit to this phonon mode. In addition to that, the shear mode is observed for both co and crossed linear polarizations, while the LEEX peak is suppressed in the cross polarized case. Even though the polarization selection rule of the LEEX peak fits to the breathing mode, the breathing mode can also be excluded due to the scattering energy and temperature behaviour. Just as for the shear mode, the breathing mode in heterostructures is located between the bilayer breathing mode position for homobilayers of the constituent materials [165]. For $MoSe_2$ homobilayers, the breathing mode is found at at $\approx 34\,\mathrm{cm}^{-1}$ [150, 156], and for WSe_2 bilayers at $\approx 29\,\mathrm{cm}^{-1}$ [155, 156]. From that it follows, that the breathing mode should be located at $\approx 31.5\,\mathrm{cm}^{-1}$ for $MoSe_2$-WSe_2

heterostructures at room temperature. The position of the LEEX peak lies below that for $T = 4\,\mathrm{K}$, and shifts to even lower energy for increasing temperature. The breathing mode can therefore be excluded as an possible interpretation.

Although considering first order Raman peaks, neither the shear or breathing mode can explain the LEEX peak, the scattering process we observed clearly seems to be an interlayer effect, that involves both of the layers in the heterostructure. The dependency on the twist angle thereby strongly resembles that of the shear mode: The LEEX peak is only observed for reconstructed heterostructures and absent on Moiré lattices, and it shows a slightly higher Raman shift for H-type than for R-type structures, that is consistently observed for different samples. This similar behaviour for different twist angles implies, that while the LEEX peak is not the shear mode itself, it maybe a process related to the shear mode. For example, a shear mode shifted in energy due to interaction with the electronic system, which would be mediated by the formation of the negatively charged trion in $MoSe_2$. Considering this possibility, it is very interesting that also in resonance to the WSe_2 trion (which we expect to be positively charged), a low-energy Raman peak showed up in the spectrum, which was located at $13.8\,\mathrm{cm}^{-1}$ for R-type structures. Strikingly, when expecting the shear mode itself at $18.75\,\mathrm{cm}^{-1}$ for $T = 4\,\mathrm{K}$, this peak is redshifted in relation to the shear mode by the almost exact same value, as the LEEX peak in resonance to $MoSe_2$ is blueshifted in relation to the shear mode; namely by close to $5\,\mathrm{cm}^{-1}$. It therefore could be the case, that by interaction with the electronic system, the shear mode energy is influenced, and two shear mode branches open up for interaction with positive or negative trions. Unfortunately, to this stage, we do not know whether this is actually the case, or if the appearance of the peak in resonance to the WSe_2 trion is just a coincidence. Nevertheless, we think that at least the LEEX peak resonant to the $MoSe_2$ trion, is the product of the electronic system interacting with the shear mode.

For the possibility of an electronic interaction with the shear mode to be plausible, the peak position of the LEEX should depend on the charge-carrier density in the sample. In Fig. 9.6 (a) the response of the LEEX peak to different excitation powers was shown; with the result that its peak position does not change. Also the fact that this peak showed very consistent Raman shifts on different samples supports the observation that no power dependency is observed, since it is not very probable that for every sample the same charge-carrier density was reached. However, it is not clear to us at the moment, whether the charge-carrier density actually has no effect on the LEEX peak, or if we always measured in a kind of saturation regime. Because on the other hand, the impact

of the number of trions formed in the material has a strong effect on the LEEX peak, as demonstrated by temperature-dependent measurements. Here, we observed the peak shifting to lower Raman shifts by about $2 - 3\,\mathrm{cm}^{-1}$ in the range between $T = 30\,\mathrm{K}$ to $T = 110\,\mathrm{K}$. Although phonons are known to shift to lower energies for increasing temperature, this is an unusually strong shift in this rather small temperature window (for typical shifts see again Fig. 9.1). Also, the shift of the LEEX peak is not yet present at $T = 30\,\mathrm{K}$ where the trion PL is still as pronounced as for $T = 4\,\mathrm{K}$; it rather seems to set in at temperatures, where the trion PL looses intensity drastically compared to the neutral exciton, meaning that trions become unstable [129]. It therefore looks as if the energy of the LEEX moves towards that of the unperturbed shear mode, when the formation of trions becomes unfavourable for higher temperatures.

10. Conclusion and outlook on part three

The purpose of this project was to perform resonant Raman experiments on TMDCs, with the goal of discovering new phenomena that are not present in the non-resonant case. It was decided to excite $MoSe_2$ using a Ti:Sapphire laser, making use of the good compatibility of the band gap energy with the tuning range of this laser. All measurements were conducted at $T = 4\,\mathrm{K}$, in order to resolve resonances with all excitonic complexes present in the material. Thus, the first data presented were characterization measurements for non-resonant excitation, to clarify how the spectral position of the A_{1g}-mode changes between room temperature and $T = 4\,\mathrm{K}$. The low-temperature values were then used to obtain correct Raman shifts for the spectra recorded with resonant excitation. This was necessary, since the laser is asymmetrically broadened by resonance fluorescence, and can not be shifted to $0\,\mathrm{cm}^{-1}$ any more. Also the low-temperature position of the interlayer shear mode of an H-type $MoSe_2$-WSe_2 heterostructure was measured for non-resonant excitation.

Another problem that occurs for resonant excitation and had to be solved, was the strong PL of $MoSe_2$ monolayers, that over shines Raman lines due to its much higher intensity. The solution presented was the usage of a $MoSe_2$-WSe_2 heterostructure, where the intralayer PL of the layers is strongly quenched as a consequence of the type II band alignment. It was further shown, that the quenching strength correlates inversely with the intensity of the interlayer exciton. Therefore, we are able to find a good spot on the sample by maximizing the interlayer PL.

After discussing these general issues, a low-temperature and excitation-energy dependent measurement of an R-type $MoSe_2$-WSe_2 heterostructure was presented. The laser energy was varied in small steps between the WSe_2 and $MoSe_2$ trions. In addition to Raman peaks already known from the literature, a low-energy excitation (LEEX) was found at about $23.5\,\mathrm{cm}^{-1}$. By analysing the resonance fluorescence of the laser and comparing it to the LEEX intensity with respect to laser excitation, it was shown that this

peak is resonantly enhanced with the $MoSe_2$ trion. Furthermore, a very weak peak could be identified at about $13.8\,cm^{-1}$ in resonance with the WSe_2 trion. As it was much easier to measure, the LEEX peak for the $MoSe_2$ trion was used for further investigations.

In the next step, the effects of different sample temperatures on the LEEX peak were examined. To do this, several laser-energy dependent series were measured for different temperatures, and the LEEX resonance curves extracted. It was shown, that the laser energy giving the LEEX maximum intensity redshifts with increasing temperature, as does the trion PL itself. Also, the intensity of the LEEX is decreased strongly for temperatures, were the trion PL is known to vanish from the PL spectrum. This intensity decrease was accompanied by a strong redshift of the spectral peak position of about $2\,cm^{-1}$, already between $T = 30\,K$ and $T = 110\,K$. To conclude the investigation of the basic properties for the new Raman peak, the laser power and polarization were varied. With the respect to the excitation power, there seemed to be no measurable effect, such as a changing Raman shift or line shape. In case of polarization, it was shown that the LEEX peak is only strongly observed for co-polarized linear polarization. This configuration was hence used for all measurements presented.

Since the LEEX peak only occurs in resonance with the $MoSe_2$ trion, the possibility of a purely electronic scattering mechanism that involves a fine structure of the trion was discussed in the following. Using singlet and triplet states of the trion, a possible mechanism was proposed that interprets the LEEX peak as the energetic difference between these two trion states. However, since the peak does not change when external magnetic fields perpendicular to the sample are applied, it was concluded that this interpretation is not appropriate.

Instead, a strong dependency of the LEEX peak on the twist angle of the heterostructure was found. First of all, an exemplary measurement on a Moiré structure was discussed. Here, the LEEX peak was not detectable, but instead a series of PL features that could be linked to the Moiré potential. Since the LEEX peak could not be found on any Moiré structure, it was further tested whether atomic reconstruction is necessary for its appearance. This was done using a sample that has both reconstructed and Moiré areas, as the twist angle is right at the edge of the two regimes. Indeed, the LEEX peak could be measured on the reconstructed parts only. Finally, it was tested if the LEEX Raman shift shows a similar difference for R and H-type structures as the interlayer shear mode does for non-resonant excitation at room temperature. It was verified, that also the LEEX peak appears at slightly higher energies for H-type structures compared to R-type structures. For the weak Raman peak in resonance to the WSe_2 trion, the

opposite behaviour was observed.

After all measurable properties of the LEEX peak were introduced, possible interpretations were discussed in the last section. An electronic scattering mechanism involving trion states was already excluded, which was further supported by the strong dependence of the peak on the twist angle. Difference processes of phonons could be excluded due to the temperature dependence, and defect activated acoustic phonons seemed unlikely for similar reasons. Therefore, the possibility of observing a first order low-energy Raman mode, namely the layer shear or breathing mode, was discussed. The breathing mode could be ruled out, as the peak position of the LEEX together with its temperature-dependent shift, did not fit to this phonon mode. The shear mode also does not fit to the measured Raman shift of the LEEX peak. However, many of the other properties of the shear mode are also found for the LEEX; it also occurs only for reconstructed structures and appears at higher Raman shifts for H-type than for R-type samples. This implies, that LEEX peak is an interaction of the shear mode with the electronic system, that is only present in resonance with the $MoSe_2$ trion. Such an interaction mechanism would then also have to explain, why the LEEX is only observed for co-polarization, whereas the shear mode is found for both co- and cross-polarization. It was noted, that the peak in resonance to the WSe_2 trion appears just at the other side of the unperturbed shear mode energy; it is however not clear at the moment, if this is just a coincidence or not.

A few days before handing in this dissertation a new possibility to interpret the LEEX peak came up, that is not yet fully developed at the moment and therefore only given here as an outlook on the topic. This new interpretation is based on a Fano resonance, which is a resonant enhancement of phonons with a continuum of electronic states [186]. Such a resonance can alter the peak position and also the line shape of a phonon peak, depending on parameters like the coupling strength and the charge-carrier density in the sample [187]. So far, the LEEX peak resembled strongly a Fano line shape when subtracting the background resonance fluorescence. However, the peak position was shifted to far away from that of the unperturbed shear mode, in order to be interpreted based on a Fano interaction of this mode with the electronic system. We very recently realized, that the spectral LEEX position is in fact lower by about $2\,\mathrm{cm}^{-1}$ than in the interpretation shown before, which makes a Fano effect possible again.

It turned out that the Raman shifts given before were not correct, by measuring the temperature-dependent position of the A_{1g}-mode in the resonant case. Therefore, the laser was tuned into resonance with the $MoSe_2$ trion at low temperatures, and the Rayleigh scattered light of the substrate (that does not show a resonance fluorescence)

monitored. This elastically scattered light was shifted to exactly $0\,\mathrm{cm}^{-1}$ in the spectrometer output, before starting the measurement. We usually do not do this procedure in any measurement, since it is very time consuming. We then took a measurement of the A_{1g}-mode and the LEEX peak for H- and R-type structures. Next, the sample was heated up to room temperature, but all settings of laser and spectrometer kept as for the low-temperature measurement. That way, we do not excite resonantly any more, as the electronic band gap is redshifted compared to $T = 4\,\mathrm{K}$. But the Raman shift of the room temperature A_{1g}-mode can now directly be compared to that of low temperatures, as laser and spectrometer were not changed. The result was, that the A_{1g}-mode barely changes its position between non-resonant room temperature measurements and resonant excitation to the $MoSe_2$ trion at low temperatures. Or, in other words, it is redshifted by about $2\,\mathrm{cm}^{-1}$ for resonant excitation to the trion, compared to a non-resonant measurement at $T = 4\,\mathrm{K}$. As we adjusted our spectra to the non-resonant position of the A_{1g}-mode, this means that the Raman shift of the LEEX peak was consequently about $2\,\mathrm{cm}^{-1}$ to high in our interpretation.

As a result, it seems as if the shear mode is blueshifted according to a Fano resonance, whereas the A_{1g}-mode is redshifted by the same effect. The simulation of the two peaks by Fano lines is however not finished by the time this thesis is written. Also, the exact mechanism of how the Fano resonance is induced is still speculation; due to the trion resonance, it seems as though electron oscillations in the conduction band are caused by the biding and unbinding of the additional electron forming the trion. These oscillations would then have to interact with the shear and A_{1g}-mode. The peak in resonance to the WSe_2 trion on the other hand, could not be explained by this interpretation, and its appearance would be seen as a pure coincidence.

Bibliography

[1]C. Raman and K. Krishnan, “A new type of secondary radiation”, Nature **121**, 501–502 (1928).

[2]C. Raman, “A change of wave-length in light scattering”, Nature **121**, 619–619 (1928).

[3]R. Loudon, “The raman effect in crystals”, Advances in Physics **13**, 423–482 (1964).

[4]C. Schüller, *Inelastic light scattering of semiconductor nanostructures: fundamentals and recent advances*, Vol. 219 (Springer Science & Business Media, 2006).

[5]M. Hirmer, D. Schuh, W. Wegscheider, T. Korn, R. Winkler, and C. Schueller, “Fingerprints of the anisotropic spin-split hole dispersion in resonant inelastic light scattering in two-dimensional hole systems”, Physical Review Letters **107**, 216805 (2011).

[6]C. Schoenhuber, M. Walser, G. Salis, C. Reichl, W. Wegscheider, T. Korn, and C. Schueller, “Inelastic light-scattering from spin-density excitations in the regime of the persistent spin helix in a GaAs-AlGaAs quantum well”, Physical Review B **89**, 085406 (2014).

[7]S. Gelfert, C. Frankerl, C. Reichl, D. Schuh, G. Salis, W. Wegscheider, D. Bougeard, T. Korn, and C. Schüller, “Inelastic light scattering by intrasubband spin-density excitations in GaAs-AlGaAs quantum wells with balanced bychkov-rashba and dresselhaus spin-orbit interaction: quantitative determination of the spin-orbit field”, Physical Review B **101**, 035427 (2020).

[8]S. Furthmeier, F. Dirnberger, J. Hubmann, B. Bauer, T. Korn, C. Schüller, J. Zweck, E. Reiger, and D. Bougeard, “Long exciton lifetimes in stacking-fault-free wurtzite GaAs nanowires”, Applied Physics Letters **105**, 222109 (2014).

[9]F. Dirnberger, M. Kammermeier, J. König, M. Forsch, P. Faria Junior, T. Campos, J. Fabian, J. Schliemann, C. Schüller, T. Korn, P. Wenk, and D. Bougeard, “Ultralong spin lifetimes in one-dimensional semiconductor nanowires”, Applied Physics Letters **114**, 202101 (2019).

[10]K. Novoselov, A. Geim, S. Morozov, D. Jiang, Y. Zhang, S. Dubonos, I. Grigorieva, and A. Firsov, “Electric field effect in atomically thin carbon films”, science **306**, 666–669 (2004).

[11]K. Novoselov, D. Jiang, F. Schedin, T. Booth, V. Khotkevich, S. Morozov, and A. Geim, “Two-dimensional atomic crystals”, Proceedings of the National Academy of Sciences of the United States of America **102**, 10451–10453 (2005).

[12]K. Mak, C. Lee, J. Hone, J. Shan, and T. Heinz, “Atomically thin MoS_2: a new direct-gap semiconductor”, Physical Review Letters **105**, 136805 (2010).

[13]A. Splendiani, L. Sun, Y. Zhang, T. Li, J. Kim, C. Chim, G. Galli, and F. Wang, “Emerging photoluminescence in monolayer MoS_2”, Nano letters **10**, 1271–1275 (2010).

[14]A. Arora, K. Nogajewski, M. Molas, M. Koperski, and M. Potemski, “Exciton band structure in layered $MoSe_2$: from a monolayer to the bulk limit”, Nanoscale **7**, 20769–20775 (2015).

[15]Y. Peter and M. Cardona, *Fundamentals of semiconductors: physics and materials properties* (Springer Science & Business Media, 2010).

[16]I. Pelant and J. Valenta, *Luminescence spectroscopy of semiconductors* (Oxford university press, 2012).

[17]A. Chernikov, T. Berkelbach, H. Hill, A. Rigosi, Y. Li, O. Aslan, D. Reichman, M. Hybertsen, and T. Heinz, “Exciton binding energy and nonhydrogenic rydberg series in monolayer WS_2”, Physical review letters **113**, 076802 (2014).

[18]M. Fox, *Optische eigenschaften von festkörpern* (Oldenbourg Verlag, 2012).

[19]A. Govorov, “Resonant light scattering induced by coulomb interaction in semiconductor microstructures”, Journal of Physics: Condensed Matter **9**, 4681 (1997).

[20]G. Danan, A. Pinczuk, J. Valladares, L. Pfeiffer, K. West, and C. Tu, “Coupling of excitons with free electrons in light scattering from GaAs quantum wells”, Physical Review B **39**, 5512 (1989).

[21]A. Cantarero, C. Trallero-Giner, and M. Cardona, “Excitons in one-phonon resonant raman scattering: deformation-potential interaction”, Physical Review B **39**, 8388 (1989).

[22]C. Trallero-Giner, A. Cantarero, and M. Cardona, “One-phonon resonant raman scattering: fröhlich exciton-phonon interaction”, Physical Review B **40**, 4030 (1989).

[23]R. Trommer and M. Cardona, "Resonant raman scattering in GaAs", Physical Review B **17**, 1865 (1978).

[24]K. Dick, P. Caroff, J. Bolinsson, M. Messing, J. Johansson, K. Deppert, L. Wallenberg, and L. Samuelson, "Control of iii–v nanowire crystal structure by growth parameter tuning", Semiconductor Science and Technology **25**, 024009 (2010).

[25]S. Meier, P. F. Junior, F. Haas, E. Heller, F. Dirnberger, V. Zeller, T. Korn, J. Fabian, D. Bougeard, and C. Schüller, "Intersubband excitations in ultrathin core-shell nanowires in the one-dimensional quantum limit probed by resonant inelastic light scattering", Phys. Rev. B **104**, 235307 (2021).

[26]R. Wagner and W. Ellis, "Vapor-liquid-solid mechanism of single crystal growth", Applied physics letters **4**, 89–90 (1964).

[27]F. Dirnberger, "New directions for semiconductor nanowires: demonstrating robust spins and long-lived excitons", Dissertation (2016).

[28]V. Dubrovskii, G. Cirlin, I. Soshnikov, A. Tonkikh, N. Sibirev, Y. Samsonenko, and V. Ustinov, "Diffusion-induced growth of GaAs nanowhiskers during molecular beam epitaxy: theory and experiment", Physical review B **71**, 205325 (2005).

[29]O. Demichel, M. Heiss, J. Bleuse, H. Mariette, and A. Fontcuberta i Morral, "Impact of surfaces on the optical properties of GaAs nanowires", Applied Physics Letters **97**, 201907 (2010).

[30]F. Dirnberger, D. Abujetas, J. König, M. Forsch, T. Koller, I. Gronwald, C. Lange, R. Huber, C. Schüller, T. Korn, J. Sanchez-Gil, and D. Bougeard, "Tuning spontaneous emission through waveguide cavity effects in semiconductor nanowires", Nano letters **19**, 7287–7292 (2019).

[31]S. Hunklinger, *Festkörperphysik* (Oldenbourg Verlag, 2009).

[32]A. De and C. Pryor, "Predicted band structures of iii-v semiconductors in the wurtzite phase", Physical Review B **81**, 155210 (2010).

[33]M. McMahon and R. Nelmes, "Observation of a wurtzite form of gallium arsenide", Physical review letters **95**, 215505 (2005).

[34]C. Yeh, Z. Lu, S. Froyen, and A. Zunger, "Zinc-blende–wurtzite polytypism in semiconductors", Physical Review B **46**, 10086 (1992).

[35]R. Leitsmann and F. Bechstedt, "Surface influence on stability and structure of hexagon-shaped iii-v semiconductor nanorods", Journal of Applied Physics **102**, 063528 (2007).

[36]T. Akiyama, K. Sano, K. Nakamura, and T. Ito, "An empirical potential approach to wurtzite–zinc-blende polytypism in group iii–v semiconductor nanowires", Japanese journal of applied physics **45**, L275 (2006).

[37]F. Glas, J. Harmand, and G. Patriarche, "Why does wurtzite form in nanowires of iii-v zinc blende semiconductors?", Physical review letters **99**, 146101 (2007).

[38]D. Jacobsson, F. Panciera, J. Tersoff, M. Reuter, S. Lehmann, S. Hofmann, K. Dick, and F. Ross, "Interface dynamics and crystal phase switching in GaAs nanowires", Nature **531**, 317–322 (2016).

[39]G. Zhang, K. Tateno, H. Sanada, T. Tawara, H. Gotoh, and H. Nakano, "Synthesis of GaAs nanowires with very small diameters and their optical properties with the radial quantum-confinement effect", Applied Physics Letters **95**, 123104 (2009).

[40]M. Koguchi, H. Kakibayashi, M. Yazawa, K. Hiruma, and T. Katsuyama, "Crystal structure change of GaAs and InAs whiskers from zinc-blende to wurtzite type", Japanese journal of applied physics **31**, 2061 (1992).

[41]I. Zardo, S. Conesa-Boj, F. Peiro, J. Morante, J. Arbiol, E. Uccelli, G. Abstreiter, and A. F. i Morral, "Raman spectroscopy of wurtzite and zinc-blende GaAs nanowires: polarization dependence, selection rules, and strain effects", Physical review B **80**, 245324 (2009).

[42]M. De Luca and I. Zardo, *Semiconductor nanowires: raman spectroscopy studies* (In-Tech, 2017).

[43]S. Crankshaw, L. Chuang, M. Moewe, and C. Chang-Hasnain, "Polarized zone-center phonon modes of wurtzite GaAs", Physical Review B **81**, 233303 (2010).

[44]N. Vainorius, S. Lehmann, K. Dick, and M. Pistol, "Non-resonant raman scattering of wurtzite GaAs and InP nanowires", Optics express **28**, 11016–11022 (2020).

[45]P. Kusch, S. Breuer, M. Ramsteiner, L. Geelhaar, H. Riechert, and S. Reich, "Band gap of wurtzite GaAs: a resonant raman study", Physical Review B **86**, 075317 (2012).

[46]B. Ketterer, M. Heiss, E. Uccelli, J. Arbiol, and A. Fontcuberta i Morral, "Untangling the electronic band structure of wurtzite GaAs nanowires by resonant raman spectroscopy", ACS nano **5**, 7585–7592 (2011).

[47]B. Ketterer, M. Heiss, M. Livrozet, A. Rudolph, E. Reiger, and A. F. i Morral, "Determination of the band gap and the split-off band in wurtzite GaAs using raman and photoluminescence excitation spectroscopy", Physical Review B **83**, 125307 (2011).

[48]W. Peng, F. Jabeen, B. Jusserand, J. Harmand, and M. Bernard, "Conduction band structure in wurtzite GaAs nanowires: a resonant raman scattering study", Applied Physics Letters **100**, 073102 (2012).

[49]M. Murayama and T. Nakayama, "Chemical trend of band offsets at wurtzite/zinc-blende heterocrystalline semiconductor interfaces", Physical Review B **49**, 4710 (1994).

[50]T. Cheiwchanchamnangij and W. Lambrecht, "Band structure parameters of wurtzite and zinc-blende GaAs under strain in the gw approximation", Physical Review B **84**, 035203 (2011).

[51]L. Ahtapodov, J. Todorovic, P. Olk, T. Mjåland, P. Slåttnes, D. Dheeraj, A. van Helvoort, B. Fimland, and H. Weman, "A story told by a single nanowire: optical properties of wurtzite GaAs", Nano letters **12**, 6090–6095 (2012).

[52]G. Signorello, E. Lörtscher, P. Khomyakov, S. Karg, D. Dheeraj, B. Gotsmann, H. Weman, and H. Riel, "Inducing a direct-to-pseudodirect bandgap transition in wurtzite GaAs nanowires with uniaxial stress", Nature communications **5**, 3655 (2014).

[53]M. De Luca, S. Rubini, M. Felici, A. Meaney, P. Christianen, F. Martelli, and A. Polimeni, "Addressing the fundamental electronic properties of wurtzite GaAs nanowires by high-field magneto-photoluminescence spectroscopy", Nano letters **17**, 6540–6547 (2017).

[54]J. Birman, "Some selection rules for band-band transitions in wurtzite structure", Physical Review **114**, 1490 (1959).

[55]P. Tronc, Y. Kitaev, G. Wang, M. Limonov, A. Panfilov, and G. Neu, "Optical selection rules for hexagonal GaN", physica status solidi (b) **216**, 599–603 (1999).

[56]M. De Luca, G. Lavenuta, A. Polimeni, S. Rubini, V. Grillo, F. Mura, A. Miriametro, M. Capizzi, and F. Martelli, "Excitonic recombination and absorption in In x Ga 1-x As/GaAs heterostructure nanowires", Physical Review B **87**, 235304 (2013).

[57]N. Vainorius, S. Lehmann, A. Gustafsson, L. Samuelson, K. A. Dick, and M. Pistol, "Wurtzite GaAs quantum wires: one-dimensional subband formation", Nano letters **16**, 2774–2780 (2016).

[58]S. Furthmeier, F. Dirnberger, M. Gmitra, A. Bayer, M. Forsch, J. Hubmann, C. Schüller, E. Reiger, J. Fabian, T. Korn, and D. Bougeard, “Enhanced spin–orbit coupling in core/shell nanowires”, Nature communications **7**, 12413 (2016).

[59]R. Robinett, “Quantum mechanics of the two-dimensional circular billiard plus baffle system and half-integral angular momentum”, European journal of physics **24**, 231 (2003).

[60]J. H. Davies, *The physics of low-dimensional semiconductors: an introduction* (Cambridge university press, 1997).

[61]B. Loitsch, D. Rudolph, S. Morkötter, M. Döblinger, G. Grimaldi, L. Hanschke, S. Matich, E. Parzinger, U. Wurstbauer, G. Abstreiter, J. Finley, and G. Koblmüller, “Tunable quantum confinement in ultrathin, optically active semiconductor nanowires via reverse-reaction growth”, Advanced Materials **27**, 2195–2202 (2015).

[62]Z. Zanolli, M. Pistol, L. Fröberg, and L. Samuelson, “Quantum-confinement effects in InAs–InP core–shell nanowires”, Journal of physics: Condensed matter **19**, 295219 (2007).

[63]A. Pinczuk, H. Störmer, R. Dingle, J. Worlock, W. Wiegmann, and A. Gossard, “Observation of intersubband excitations in a multilayer two dimensional electron gas”, Solid State Communications **32**, 1001–1003 (1979).

[64]G. Abstreiter and K. Ploog, “Inelastic light scattering from a quasi-two-dimensional electron system in GaAs-Al x Ga 1- x As heterojunctions”, Physical Review Letters **42**, 1308 (1979).

[65]J. Weiner, G. Danan, A. Pinczuk, J. Valladares, L. Pfeiffer, and K. West, “Electron gas in semiconductor multiple quantum wires: spatially indirect optical transitions”, Physical review letters **63**, 1641 (1989).

[66]R. Strenz, U. Bockelmann, F. Hirler, G. Abstreiter, G. Böhm, and G. Weimann, “Single-particle excitations in quasi-zero-and quasi-one-dimensional electron systems”, Physical review letters **73**, 3022 (1994).

[67]A. Pinczuk, S. Schmitt-Rink, G. Danan, J. Valladares, L. Pfeiffer, and K. West, “Large exchange interactions in the electron gas of GaAs quantum wells”, Physical review letters **63**, 1633 (1989).

[68]E. Burstein, A. Pinczuk, and D. Mills, “Inelastic light scattering by charge carrier excitations in two-dimensional plasmas: theoretical considerations”, Surface Science **98**, 451–468 (1980).

[69]C. Schüller, G. Biese, K. Keller, C. Steinebach, D. Heitmann, P. Grambow, and K. Eberl, "Single-particle excitations and many-particle interactions in quantum wires and dots", Physical Review B **54**, R17304 (1996).

[70]T. Egeler, G. Abstreiter, G. Weimann, T. Demel, D. Heitmann, P. Grambow, and W. Schlapp, "Anisotropic plasmon dispersion in a lateral quantum-wire superlattice", Physical review letters **65**, 1804 (1990).

[71]G. Biese, C. Schüller, K. Keller, C. Steinebach, D. Heitmann, P. Grambow, and K. Eberl, "Coupling of lateral and vertical electron motion in GaAs-Al x Ga 1- x As quantum wires and dots", Physical Review B **53**, 9565 (1996).

[72]A. Goni, A. Pinczuk, J. Weiner, J. Calleja, B. Dennis, L. Pfeiffer, and K. West, "One-dimensional plasmon dispersion and dispersionless intersubband excitations in GaAs quantum wires", Physical review letters **67**, 3298 (1991).

[73]A. Schmeller, A. Goni, A. Pinczuk, J. Weiner, J. Calleja, B. Dennis, L. Pfeiffer, and K. West, "Inelastic light scattering by spin-density, charge-density, and single-particle excitations in GaAs quantum wires", Physical Review B **49**, 14778 (1994).

[74]C. Dahl, B. Jusserand, and B. Etienne, "Selection rules in raman scattering by plasmons in quantum wires", Physical Review B **51**, 17211 (1995).

[75]E. Ulrichs, G. Biese, C. Steinebach, C. Schüller, D. Heitmann, and K. Eberl, "One-dimensional plasmons in magnetic fields", Physical Review B **56**, R12760 (1997).

[76]F. Perez, S. Zanier, S. Hameau, B. Jusserand, Y. Guldner, A. Cavanna, L. Ferlazzo-Manin, and B. Etienne, "Lateral electron confinement in narrow deep etched wires", Applied physics letters **72**, 1368–1370 (1998).

[77]M. Bootsmann, C. Hu, C. Heyn, D. Heitmann, and C. Schüller, "Acoustic plasmons and indirect intersubband excitations in tunneling-coupled GaAs- Al x Ga 1- x As double quantum wells", Physical Review B **67**, 121309 (2003).

[78]R. Anufriev, N. Chauvin, H. Khmissi, K. Naji, M. Gendry, and C. Bru-Chevallier, "Impact of substrate-induced strain and surface effects on the optical properties of InP nanowires", Applied Physics Letters **101**, 072101 (2012).

[79]J. Yan, Y. Zhang, P. Kim, and A. Pinczuk, "Electric field effect tuning of electron-phonon coupling in graphene", Physical review letters **98**, 166802 (2007).

[80]Y. Hu, S. Chen, X. Cong, S. Sun, J. Wu, D. Zhang, F. Yang, J. Yang, P. Tan, and Y. Li, "Electronic raman scattering in suspended semiconducting carbon nanotube", The Journal of Physical Chemistry Letters **11**, 10497–10503 (2020).

[81]B. Zhang, Z. Nie, B. Wang, D. Wang, J. Tang, X. Wang, J. Zhang, G. Xing, W. Zhang, and Z. Wei, "Ultrafast carrier relaxation dynamics of photoexcited GaAs and GaAs/AlGaAs nanowire array", Physical Chemistry Chemical Physics **22**, 25819–25826 (2020).

[82]S. D. Sarma and D. Wang, "Many-body renormalization of semiconductor quantum wire excitons: absorption, gain, binding, and unbinding", Physical review letters **84**, 2010 (2000).

[83]A. Thilagam, "Effect of geometrical shape in the cross section of quantum wires on exciton binding energy", Journal of applied physics **82**, 5753–5757 (1997).

[84]F. Rossi, G. Goldoni, and E. Molinari, "Shape-independent scaling of excitonic confinement in realistic quantum wires", Physical review letters **78**, 3527 (1997).

[85]T. Someya, H. Akiyama, and H. Sakaki, "Enhanced binding energy of one-dimensional excitons in quantum wires", Physical review letters **76**, 2965 (1996).

[86]R. Rinaldi, R. Cingolani, M. Lepore, M. Ferrara, I. Catalano, F. Rossi, L. Rota, E. Molinari, P. Lugli, U. Marti, F. Morier-Gemoud, P. Ruterana, and F. Reinhart, "Exciton binding energy in GaAs v-shaped quantum wires", Physical review letters **73**, 2899 (1994).

[87]A. Mooradian and G. Wright, "Observation of the interaction of plasmons with longitudinal optical phonons in GaAs", Physical Review Letters **16**, 999 (1966).

[88]A. Goñi, U. Haboeck, C. Thomsen, K. Eberl, F. Reboredo, C. Proetto, and F. Guinea, "Exchange instability of the two-dimensional electron gas in semiconductor quantum wells", Physical Review B **65**, 121313 (2002).

[89]P. Giudici, A. Goñi, C. Thomsen, P. Bolcatto, C. Proetto, and K. Eberl, "Effects of the exchange instability on collective spin and charge excitations of the two-dimensional electron gas", Physical Review B **70**, 235418 (2004).

[90]P. Giudici, A. Goñi, P. Bolcatto, C. Proetto, C. Thomsen, K. Eberl, and M. Hauser, "Evidence of breakdown of the spin symmetry in diluted 2d electron gases", EPL (Europhysics Letters) **77**, 37003 (2007).

[91]R. Bromley, R. Murray, and A. Yoffe, "The band structures of some transition metal dichalcogenides. iii. group via: trigonal prism materials", Journal of Physics C: Solid State Physics **5**, 759 (1972).

[92]L. Mattheiss, "Band structures of transition-metal-dichalcogenide layer compounds", Physical Review B **8**, 3719 (1973).

[93]L. Mattheiss, "Energy bands for 2 h- $NbSe_2$ and 2 h- MoS_2", Physical Review Letters **30**, 784 (1973).

[94]J. Frondel and F. Wickman, "Molybdenite polytypes in theory and occurrence. ii. some naturally-occurring polytypes of molybdenite", The American Mineralogist **55**, 1857 (1970).

[95]R. Dickinson and L. Pauling, "The crystal structure of molybdenite", Journal of the American Chemical Society **45**, 1466–1471 (1923).

[96]P. James and M. Lavik, "The crystal structure of $MoSe_2$", Acta Crystallographica **16**, 1183–1183 (1963).

[97]W. Hicks, "Semiconducting behavior of substituted tungsten diselenide and its analogues", Journal of The Electrochemical Society **111**, 1058 (1964).

[98]R. Coehoorn, C. Haas, J. Dijkstra, C. Flipse, R. De Groot, and A. Wold, "Electronic structure of $MoSe_2$, MoS_2, and WSe_2. i. band-structure calculations and photoelectron spectroscopy", Physical Review B **35**, 6195 (1987).

[99]R. Coehoorn, C. Haas, and R. De Groot, "Electronic structure of $MoSe_2$, MoS_2, and WSe_2. ii. the nature of the optical band gaps", Physical Review B **35**, 6203 (1987).

[100]D. Voß, P. Krüger, A. Mazur, and J. Pollmann, "Atomic and electronic structure of WSe_2 from ab initio theory: bulk crystal and thin film systems", Physical Review B **60**, 14311 (1999).

[101]T. Li and G. Galli, "Electronic properties of MoS_2 nanoparticles", The Journal of Physical Chemistry C **111**, 16192–16196 (2007).

[102]S. Lebegue and O. Eriksson, "Electronic structure of two-dimensional crystals from ab initio theory", Physical Review B **79**, 115409 (2009).

[103]P. Tonndorf, R. Schmidt, P. Böttger, X. Zhang, J. Börner, A. Liebig, M. Albrecht, C. Kloc, O. Gordan, D. Zahn, S. de Vasconcellos, and R. Bratschitsch, "Photoluminescence emission and raman response of monolayer MoS_2, $MoSe_2$, and WSe_2", Optics express **21**, 4908–4916 (2013).

[104]S. Tongay, J. Zhou, C. Ataca, K. Lo, T. Matthews, L. Jingbo, J. Grossman, and W. Jungqiao, "Thermally driven crossover from indirect toward direct bandgap in 2d semiconductors: $MoSe_2$ versus MoS_2", Nano letters **12**, 5576–5580 (2012).

[105]W. Zhao, Z. Ghorannevis, L. Chu, M. Toh, C. Kloc, P. Tan, and G. Eda, "Evolution of electronic structure in atomically thin sheets of WS_2 and WSe_2", ACS nano **7**, 791–797 (2013).

[106]A. Kuc, N. Zibouche, and T. Heine, "Influence of quantum confinement on the electronic structure of the transition metal sulfide TS_2", Physical Review B **83**, 245213 (2011).

[107]G. Liu, W. Shan, Y. Yao, W. Yao, and D. Xiao, "Three-band tight-binding model for monolayers of group-vib transition metal dichalcogenides", Physical Review B **88**, 085433 (2013).

[108]Z. Zhu, Y. Cheng, and U. Schwingenschlögl, "Giant spin-orbit-induced spin splitting in two-dimensional transition-metal dichalcogenide semiconductors", Physical Review B **84**, 153402 (2011).

[109]D. Xiao, G. Liu, W. Feng, X. Xu, and W. Yao, "Coupled spin and valley physics in monolayers of MoS_2 and other group-vi dichalcogenides", Physical Review Letters **108**, 196802 (2012).

[110]K. Kosmider, J. Gonzalez, and J. Fernandez-Rossier, "Large spin splitting in the conduction band of transition metal dichalcogenide monolayers", Physical Review B **88**, 245436 (2013).

[111]N. Alidoust, G. Bian, S. Xu, R. Sankar, M. Neupane, C. Liu, I. Belopolski, D. Qu, J. Denlinger, F. Chou, and Z. Hasan, "Observation of monolayer valence band spin-orbit effect and induced quantum well states in MoX_2", Nature communications **5**, 4673 (2014).

[112]T. Cheiwchanchamnangij and W. Lambrecht, "Quasiparticle band structure calculation of monolayer, bilayer, and bulk MoS_2", Physical Review B **85**, 205302 (2012).

[113]A. Kormányos, G. Burkard, M. Gmitra, J. Fabian, V. Zólyomi, N. Drummond, and V. Fal'ko, "K· p theory for two-dimensional transition metal dichalcogenide semiconductors", 2D Materials **2**, 022001 (2015).

[114]Y. Zhang, T. Chang, B. Zhou, Y. Cui, H. Yan, Z. Liu, F. Schmitt, J. Lee, R. Moore, Y. Chen, H. Lin, H. Jeng, S. Mo, Z. Hussain, A. Bansil, and Z. Shen, "Direct observation of the transition from indirect to direct bandgap in atomically thin epitaxial $MoSe_2$", Nature nanotechnology **9**, 111–115 (2014).

[115]H. Zeng, G. Liu, J. Dai, Y. Yan, B. Zhu, R. He, L. Xie, S. Xu, X. Chen, W. Yao, and X. Cui, "Optical signature of symmetry variations and spin-valley coupling in atomically thin tungsten dichalcogenides", Scientific reports **3**, 1608 (2013).

[116]Z. Wang, L. Zhao, K. Mak, and J. Shan, "Probing the spin-polarized electronic band structure in monolayer transition metal dichalcogenides by optical spectroscopy", Nano letters **17**, 740–746 (2017).

[117]G. Wang, C. Robert, M. Glazov, F. Cadiz, E. Courtade, T. Amand, D. Lagarde, T. Taniguchi, K. Watanabe, B. Urbaszek, and X. Marie, "In-plane propagation of light in transition metal dichalcogenide monolayers: optical selection rules", Physical review letters **119**, 047401 (2017).

[118]X. Zhang, T. Cao, Z. Lu, Y. Lin, F. Zhang, Y. Wang, Z. Li, J. Hone, J. Robinson, D. Smirnov, S. Louie, and T. Heinz, "Magnetic brightening and control of dark excitons in monolayer WSe_2", Nature nanotechnology **12**, 883–888 (2017).

[119]M. Molas, C. Faugeras, A. Slobodeniuk, K. Nogajewski, M. Bartos, D. Basko, and M. Potemski, "Brightening of dark excitons in monolayers of semiconducting transition metal dichalcogenides", 2D Materials **4**, 021003 (2017).

[120]T. Cao, G. Wang, W. Han, H. Ye, C. Zhu, J. Shi, Q. Niu, P. Tan, E. Wang, B. Liu, and J. Feng, "Valley-selective circular dichroism of monolayer molybdenum disulphide", Nature communications **3**, 887 (2012).

[121]K. Mak, K. He, J. Shan, and T. Heinz, "Control of valley polarization in monolayer MoS_2 by optical helicity", Nature nanotechnology **7**, 494–498 (2012).

[122]H. Zeng, J. Dai, W. Yao, D. Xiao, and X. Cui, "Valley polarization in MoS_2 monolayers by optical pumping", Nature nanotechnology **7**, 490–493 (2012).

[123]S. Wu, C. Huang, G. Aivazian, J. Ross, D. Cobden, and X. Xu, "Vapor–solid growth of high optical quality MoS_2 monolayers with near-unity valley polarization", ACS nano **7**, 2768–2772 (2013).

[124]G. Sallen, L. Bouet, X. Marie, G. Wang, C. Zhu, W. Han, Y. Lu, P. Tan, T. Amand, B. Liu, and B. Urbaszek, "Robust optical emission polarization in MoS_2 monolayers through selective valley excitation", Physical Review B **86**, 081301 (2012).

[125]M. Baranowski, A. Surrente, D. Maude, M. Ballottin, A. Mitioglu, P. Christianen, Y. Kung, D. Dumcenco, A. Kis, and P. Plochocka, "Dark excitons and the elusive valley polarization in transition metal dichalcogenides", 2D Materials **4**, 025016 (2017).

[126]G. Wang, A. Chernikov, M. Glazov, T. Heinz, X. Marie, T. Amand, and B. Urbaszek, “Colloquium: excitons in atomically thin transition metal dichalcogenides”, Reviews of Modern Physics **90**, 021001 (2018).

[127]G. Plechinger, P. Nagler, A. Arora, A. Granados del Águila, M. Ballottin, T. Frank, P. Steinleitner, M. Gmitra, J. Fabian, P. Christianen, R. Bratschitsch, C. Schüller, and T. Korn, “Excitonic valley effects in monolayer WS_2 under high magnetic fields”, Nano letters **16**, 7899–7904 (2016).

[128]A. Stier, N. Wilson, G. Clark, X. Xu, and S. Crooker, “Probing the influence of dielectric environment on excitons in monolayer WSe_2: insight from high magnetic fields”, Nano letters **16**, 7054–7060 (2016).

[129]J. Ross, S. Wu, H. Yu, N. Ghimire, A. Jones, G. Aivazian, J. Yan, D. Mandrus, D. Xiao, W. Yao, and X. Xu, “Electrical control of neutral and charged excitons in a monolayer semiconductor”, Nature Communications **4**, 1474 (2013).

[130]Z. Li, T. Wang, Z. Lu, C. Jin, Y. Chen, Y. Meng, Z. Lian, T. Taniguchi, K. Watanabe, S. Zhang, D. Smirnov, and S. Shi, “Revealing the biexciton and trion-exciton complexes in bn encapsulated WSe_2”, Nature communications **9**, 3719 (2018).

[131]M. Barbone, A. Montblanch, D. Kara, C. Palacios-Berraquero, A. Cadore, D. De Fazio, B. Pingault, E. Mostaani, H. Li, B. Chen, K. Watanabe, T. Taniguchi, S. Tongay, G. Wang, A. Ferrari, and M. Atatüre, “Charge-tuneable biexciton complexes in monolayer WSe_2”, Nature communications **9**, 3721 (2018).

[132]Z. Ye, L. Waldecker, E. Ma, D. Rhodes, A. Antony, B. Kim, X. Zhang, M. Deng, Y. Jiang, Z. Lu, D. Smirnov, K. Watanabe, T. Taniguchi, J. Hone, and T. Heinz, “Efficient generation of neutral and charged biexcitons in encapsulated WSe_2 monolayers”, Nature communications **9**, 3718 (2018).

[133]H. Yu, G. Liu, P. Gong, X. Xu, and W. Yao, “Dirac cones and dirac saddle points of bright excitons in monolayer transition metal dichalcogenides”, Nature communications **5**, 3876 (2014).

[134]G. Plechinger, P. Nagler, A. Arora, R. Schmidt, A. Chernikov, A. G. Del Águila, P. Christianen, R. Bratschitsch, C. Schüller, and T. Korn, “Trion fine structure and coupled spin–valley dynamics in monolayer tungsten disulfide”, Nature communications **7**, 12715 (2016).

[135]A. Jones, H. Yu, N. Ghimire, S. Wu, G. Aivazian, J. Ross, B. Zhao, J. Yan, D. Mandrus, D. Xiao, W. Yao, and X. Xu, "Optical generation of excitonic valley coherence in monolayer WSe_2", Nature nanotechnology **8**, 634–638 (2013).

[136]G. Wang, L. Bouet, D. Lagarde, M. Vidal, A. Balocchi, T. Amand, X. Marie, and B. Urbaszek, "Valley dynamics probed through charged and neutral exciton emission in monolayer WSe_2", Physical Review B **90**, 075413 (2014).

[137]G. Aivazian, Z. Gong, A. Jones, R. Chu, J. Yan, D. Mandrus, C. Zhang, D. Cobden, W. Yao, and X. Xu, "Magnetic control of valley pseudospin in monolayer WSe_2", Nature Physics **11**, 148 (2015).

[138]T. Deilmann, P. Krüger, and M. Rohlfing, "Ab initio studies of exciton g factors: monolayer transition metal dichalcogenides in magnetic fields", Physical review letters **124**, 226402 (2020).

[139]J. Förste, N. Tepliakov, S. Kruchinin, J. Lindlau, V. Funk, M. Förg, K. Watanabe, T. Taniguchi, A. Baimuratov, and A. Högele, "Exciton g-factors in monolayer and bilayer WSe_2 from experiment and theory", Nature Communications **11**, 4539 (2020).

[140]T. Woźniak, P. F. Junior, G. Seifert, A. Chaves, and J. Kunstmann, "Exciton g factors of van der waals heterostructures from first-principles calculations", Physical Review B **101**, 235408 (2020).

[141]F. Xuan and S. Quek, "Valley zeeman effect and landau levels in two-dimensional transition metal dichalcogenides", Physical Review Research **2**, 033256 (2020).

[142]D. MacNeill, C. Heikes, K. Mak, Z. Anderson, A. Kormányos, V. Zólyomi, J. Park, and D. Ralph, "Breaking of valley degeneracy by magnetic field in monolayer $MoSe_2$", Physical review letters **114**, 037401 (2015).

[143]J. Verble and T. Wieting, "Lattice mode degeneracy in MoS_2 and other layer compounds", Physical review letters **25**, 362 (1970).

[144]H. Terrones, E. Del Corro, S. Feng, J. Poumirol, D. Rhodes, D. Smirnov, N. Pradhan, Z. Lin, M. Nguyen, A. Elias, T. Mallouk, L. Balicas, M. Pimenta, and M. Terrones, "New first order raman-active modes in few layered transition metal dichalcogenides", Scientific reports **4**, 4215 (2014).

[145]K. Kim, J. Lee, D. Nam, and H. Cheong, "Davydov splitting and excitonic resonance effects in raman spectra of few-layer $MoSe_2$.", ACS nano **10**, 8113 (2016).

[146] S. Horzum, H. Sahin, S. Cahangirov, P. Cudazzo, A. Rubio, T. Serin, and F. Peeters, "Phonon softening and direct to indirect band gap crossover in strained single-layer $MoSe_2$", Physical Review B **87**, 125415 (2013).

[147] C. Lee, H. Yan, L. Brus, T. Heinz, J. Hone, and S. Ryu, "Anomalous lattice vibrations of single-and few-layer MoS_2", ACS nano **4**, 2695–2700 (2010).

[148] C. Ataca, M. Topsakal, E. Akturk, and S. Ciraci, "A comparative study of lattice dynamics of three-and two-dimensional MoS_2", The Journal of Physical Chemistry C **115**, 16354–16361 (2011).

[149] A. Molina-Sanchez and L. Wirtz, "Phonons in single-layer and few-layer MoS_2 and WS_2", Physical Review B **84**, 155413 (2011).

[150] P. Soubelet, A. Bruchhausen, A. Fainstein, K. Nogajewski, and C. Faugeras, "Resonance effects in the raman scattering of monolayer and few-layer $MoSe_2$", Physical Review B **93**, 155407 (2016).

[151] G. Frey, R. Tenne, M. Matthews, M. Dresselhaus, and G. Dresselhaus, "Raman and resonance raman investigation of MoS_2 nanoparticles", Physical Review B **60**, 2883 (1999).

[152] B. Carvalho, L. Malard, J. Alves, C. Fantini, and M. Pimenta, "Symmetry-dependent exciton-phonon coupling in 2d and bulk MoS_2 observed by resonance raman scattering", Physical review letters **114**, 136403 (2015).

[153] G. Plechinger, S. Heydrich, J. Eroms, D. Weiss, C. Schüller, and T. Korn, "Raman spectroscopy of the interlayer shear mode in few-layer mos 2 flakes", Applied Physics Letters **101**, 101906 (2012).

[154] H. Zeng, B. Zhu, K. Liu, J. Fan, X. Cui, and Q. Zhang, "Low-frequency raman modes and electronic excitations in atomically thin MoS_2 films", Physical Review B **86**, 241301 (2012).

[155] Y. Zhao, X. Luo, H. Li, J. Zhang, P. Araujo, C. Gan, J. Wu, H. Zhang, S. Quek, M. Dresselhaus, and Q. Xiong, "Interlayer breathing and shear modes in few-trilayer MoS_2 and WSe_2", Nano letters **13**, 1007–1015 (2013).

[156] S. Chen, C. Zheng, M. Fuhrer, and J. Yan, "Helicity-resolved raman scattering of MoS_2, $MoSe_2$, WS_2, and WSe_2 atomic layers", Nano letters **15**, 2526–2532 (2015).

[157] S. Huang, X. Ling, L. Liang, J. Kong, H. Terrones, V. Meunier, and M. Dresselhaus, "Probing the interlayer coupling of twisted bilayer MoS_2 using photoluminescence spectroscopy", Nano letters **14**, 5500–5508 (2014).

[158] R. Bistritzer and A. MacDonald, “Moiré bands in twisted double-layer graphene”, Proceedings of the National Academy of Sciences **108**, 12233–12237 (2011).

[159] A. Van Der Zande, J. Kunstmann, A. Chernikov, D. Chenet, Y. You, X. Zhang, P. Huang, T. Berkelbach, L. Wang, F. Zhang, M. Hybertsen, D. Muller, D. Reichman, T. Heinz, and J. Hone, “Tailoring the electronic structure in bilayer molybdenum disulfide via interlayer twist”, Nano letters **14**, 3869–3875 (2014).

[160] H. Kumar, D. Er, L. Dong, J. Li, and V. Shenoy, “Elastic deformations in 2d van der waals heterostructures and their impact on optoelectronic properties: predictions from a multiscale computational approach”, Scientific reports **5**, 10872 (2015).

[161] A. Weston, Y. Zou, V. Enaldiev, A. Summerfield, N. Clark, V. Zólyomi, A. Graham, C. Yelgel, S. Magorrian, M. Zhou, J. Zultak, D. Hopkinson, A. Barinov, T. Bointon, A. Kretinin, N. Wilson, P. Beton, V. Falko, S. Haigh, and R. Gorbachev, “Atomic reconstruction in twisted bilayers of transition metal dichalcogenides”, Nature Nanotechnology **15**, 592–597 (2020).

[162] M. Rosenberger, H. Chuang, M. Phillips, V. Oleshko, K. McCreary, S. Sivaram, C. Hellberg, and B. Jonker, “Twist angle-dependent atomic reconstruction and moiré patterns in transition metal dichalcogenide heterostructures”, ACS nano **14**, 4550–4558 (2020).

[163] P. Parzefall, J. Holler, M. Scheuck, A. Beer, K. Lin, B. Peng, B. Monserrat, P. Nagler, M. Kempf, T. Korn, and C. Schüller, “Moiré phonons in twisted $MoSe_2$–WSe_2 heterobilayers and their correlation with interlayer excitons”, 2D Materials **8**, 035030 (2021).

[164] J. Holler, S. Meier, M. Kempf, P. Nagler, K. Watanabe, T. Taniguchi, T. Korn, and C. Schüller, “Low-frequency raman scattering in WSe_2- $MoSe_2$ heterobilayers: evidence for atomic reconstruction”, Applied Physics Letters **117**, 013104 (2020).

[165] C. Lui, Z. Ye, C. Ji, K. Chiu, C. Chou, T. Andersen, C. Means-Shively, H. Anderson, J. Wu, T. Kidd, Y. Lee, and R. He, “Observation of interlayer phonon modes in van der waals heterostructures”, Physical Review B **91**, 165403 (2015).

[166] A. Puretzky, L. Liang, X. Li, K. Xiao, K. Wang, M. Mahjouri-Samani, L. Basile, J. Idrobo, B. Sumpter, V. Meunier, and D. Geohegan, “Low-frequency raman fingerprints of two-dimensional metal dichalcogenide layer stacking configurations”, ACS nano **9**, 6333–6342 (2015).

[167]A. Puretzky, L. Liang, X. Li, K. Xiao, B. Sumpter, V. Meunier, and D. Geohegan, "Twisted $MoSe_2$ bilayers with variable local stacking and interlayer coupling revealed by low-frequency raman spectroscopy", ACS nano **10**, 2736–2744 (2016).

[168]S. Huang, L. Liang, X. Ling, A. Puretzky, D. Geohegan, B. Sumpter, J. Kong, V. Meunier, and M. Dresselhaus, "Low-frequency interlayer raman modes to probe interface of twisted bilayer MoS_2", Nano letters **16**, 1435–1444 (2016).

[169]J. Zhang, J. Wang, P. Chen, Y. Sun, S. Wu, Z. Jia, X. Lu, H. Yu, W. Chen, J. Zhu, G. Xie, R. Yang, D. Shi, X. Xu, J. Xiang, K. Liu, and G. Zhang, "Observation of strong interlayer coupling in MoS_2/WS_2 heterostructures", Advanced Materials **28**, 1950–1956 (2016).

[170]P. Nayak, Y. Horbatenko, S. Ahn, G. Kim, J. Lee, K. Ma, A. Jang, H. Lim, D. Kim, S. Ryu, H. Cheong, N. Park, and H. Shin, "Probing evolution of twist-angle-dependent interlayer excitons in $MoSe_2/WSe_2$ van der waals heterostructures", ACS nano **11**, 4041–4050 (2017).

[171]M. Lin, Q. Tan, J. Wu, X. Chen, J. Wang, Y. Pan, X. Zhang, X. Cong, J. Zhang, W. Ji, P. Hu, K. Liu, and P. Tan, "Moiré phonons in twisted bilayer MoS_2", Acs Nano **12**, 8770–8780 (2018).

[172]H. Fang, C. Battaglia, C. Carraro, S. Nemsak, B. Ozdol, J. Kang, H. Bechtel, S. Desai, F. Kronast, A. Unal, C. Conti G. Conlon, G. Palsson, M. Martin, A. Minor, C. Fadley, E. Yablonovitch, R. Maboudian, and A. Javey, "Strong interlayer coupling in van der waals heterostructures built from single-layer chalcogenides", Proceedings of the National Academy of Sciences **111**, 6198–6202 (2014).

[173]P. Rivera, J. Schaibley, A. Jones, J. Ross, S. Wu, G. Aivazian, P. Klement, K. Seyler, G. Clark, N. Ghimire, J. Yan, D. Mandrus, W. Yao, and X. Xu, "Observation of long-lived interlayer excitons in monolayer $MoSe_2$–WSe_2 heterostructures", Nature communications **6**, 6242 (2015).

[174]J. Kang, S. Tongay, J. Zhou, J. Li, and J. Wu, "Band offsets and heterostructures of two-dimensional semiconductors", Applied Physics Letters **102**, 012111 (2013).

[175]Y. Liang, S. Huang, R. Soklaski, and L. Yang, "Quasiparticle band-edge energy and band offsets of monolayer of molybdenum and tungsten chalcogenides", Applied physics letters **103**, 042106 (2013).

[176]K. Seyler, P. Rivera, H. Yu, N. Wilson, E. Ray, D. Mandrus, J. Yan, W. Yao, and X. Xu, "Signatures of moiré-trapped valley excitons in $MoSe_2/WSe_2$ heterobilayers", Nature **567**, 66–70 (2019).

[177]P. Nagler, M. Ballottin, A. Mitioglu, F. Mooshammer, N. Paradiso, C. Strunk, R. Huber, A. Chernikov, P. Christianen, C. Schüller, and T. Korn, "Giant magnetic splitting inducing near-unity valley polarization in van der waals heterostructures", Nature communications **8**, 1551 (2017).

[178]J. Holler, M. Selig, M. Kempf, J. Zipfel, P. Nagler, M. Katzer, F. Katsch, M. Ballottin, A. Mitioglu, A. Chernikov, P. Christianen, C. Schüller, A. Knorr, and T. Korn, "Interlayer exciton valley polarization dynamics in large magnetic fields", Physical Review B **105**, 085303 (2022).

[179]A. Castellanos-Gomez, M. Buscema, R. Molenaar, V. Singh, L. Janssen, H. van der Zant, and G. Steele, "Deterministic transfer of two-dimensional materials by all-dry viscoelastic stamping", 2D Materials **1**, 011002 (2014).

[180]D. Late, S. Shirodkar, U. Waghmare, V. Dravid, and C. Rao, "Thermal expansion, anharmonicity and temperature-dependent raman spectra of single-and few-layer $MoSe_2$ and WSe_2", ChemPhysChem **15**, 1592–1598 (2014).

[181]D. Nam, J. Lee, and H. Cheong, "Excitation energy dependent raman spectrum of $MoSe_2$", Scientific reports **5**, 17113 (2015).

[182]X. Zhang, X. Qiao, W. Shi, J. Wu, D. Jiang, and P. Tan, "Phonon and raman scattering of two-dimensional transition metal dichalcogenides from monolayer, multilayer to bulk material", Chemical Society Reviews **44**, 2757–2785 (2015).

[183]R. Tempelaar and T. Berkelbach, "Many-body simulation of two-dimensional electronic spectroscopy of excitons and trions in monolayer transition metal dichalcogenides", Nature communications **10**, 3419 (2019).

[184]K. Hao, J. Specht, P. Nagler, L. Xu, K. Tran, A. Singh, C. Dass, C. Schüller, T. Korn, M. Richter, A. Knorr, X. Li, and G. Moody, "Neutral and charged inter-valley biexcitons in monolayer $MoSe_2$", Nature communications **8**, 15552 (2017).

[185]J. Klein, M. Florian, A. Hötger, A. Steinhoff, A. Delhomme, T. Taniguchi, K. Watanabe, F. Jahnke, A. Holleitner, M. Potemski, C. Faugeras, A. Stier, and J. Finley, "Trions in MoS_2 are quantum superpositions of intra-and intervalley spin states", Physical Review B **105**, L041302 (2022).

[186]U. Fano, “Effects of configuration interaction on intensities and phase shifts”, Physical Review **124**, 1866 (1961).

[187]F. Cerdeira, T. Fjeldly, and M. Cardona, “Effect of free carriers on zone-center vibrational modes in heavily doped p-type Si. ii. optical modes”, Physical Review B **8**, 4734 (1973).

Acknowledgements

In the end, I would like to thank all the people without whom this thesis would not have been possible. In particular I would like to name:

- Prof. Dr. Christian Schüller, for giving me the opportunity to do my thesis in his group. His very helpful and kind attitude has always led to great discussions about my projects and new ideas for the experimental path.
- Prof. Dr. Tobias Korn, who taught me most of my practical knowledge in the laboratory during my masters thesis, and was still involved in this work by providing great new ideas for my TMDC project.
- Prof. Dr. Dominique Bougeard, Dr. Florian Dirnberger and Viola Zeller for providing the high quality nanowire samples, that made my Raman measurements on the intersubband excitations possible.
- Dr. Paulo de Faria Junior for his theoretical support on the nanowire topic, and his very quick response to all of our ideas concerning new calculations.
- Sebastian Krug, with whom I spent countless hours on planning and rebuilding the magnet cryostat setup, and Dr. Sebastian Bange, who has always helped to solve our problems that occurred during this process.
- Dr. Philipp Nagler, Dr. Johannes Holler, Dr. Sven Gelfert, Philipp Parzefall and Michael Kempf, for their great help and support with my experiments, either by sharing their TMDC samples, or by helping me out with measurements in other laboratories.
- my former master students Ferdinand Haas and Matthias Dietl, who were involved in many of the experiments presented in this thesis.
- Christof Ermer, for solving all software related issues and Eva Weiss, for taking care of the administering part.

- Every other member of the working group, for the pleasant and joyful atmosphere.
- my family, who always supported my goals, no matter in which direction they were going.